Numerical Modeling of Permafrost in Heterogeneous Media

by

Erfan Abedian Amiri

A thesis
presented to the University of Waterloo
in fulfillment of the
thesis requirement for the degree of
Doctor of Philosophy
in
Civil Engineering

Waterloo, Ontario, Canada, 2020

Examining Committee Membership

The following served on the Examining Committee for this thesis. The decision of the Examining Committee is by majority vote.

External Examiner: Robert A. Schincariol
Professor
Department of Earth Sciences and
Department of Civil and Environmental Engineering
Western University

Supervisor: James R. Craig
Associate Professor
Department of Civil and Environmental Engineering
University of Waterloo

Internal Members: David L. Rudolph
Professor
Department of Earth and Environmental Sciences and
Department of Civil and Environmental Engineering
University of Waterloo

Robert Gracie
Associate Professor
Department of Civil and Environmental Engineering
University of Waterloo

Internal-External Member: William L. Quinton
Professor
Department of Geography and Environmental Studies
Wilfrid Laurier University and
Department of Earth and Environmental Sciences
University of Waterloo

I hereby declare that I am the sole author of this thesis. This is a true copy of the thesis, including any required final revisions, as accepted by my examiners.

I understand that my thesis may be made electronically available to the public.

Abstract

Interest in numerical modeling of permafrost has increased over the past decade due to accelerating rates of permafrost thaw. Discontinuous permafrost regions are particularly susceptible to climate change since small increases in mean annual temperature may lead to significant permafrost thaw, landscape change, changes in hydrologic connectivity, and greenhouse gas (GHG) emissions. The influence of local heterogeneities on the short- and long-term evolution of permafrost bodies is poorly understood. In order to numerically simulate the freeze-thaw processes in heterogenous media, a robust numerical model is desirable to overcome potential instabilities induced by heterogeneity in soil thermal properties. Here, such a model is developed, supplemented by a careful evaluation of the impact of heterogeneity upon the soil freezing curve, and applied to investigate the influence of local heterogeneity upon discontinuous permafrost evolution.

Numerical models of permafrost evolution in porous media typically rely upon a smooth continuous relation between pore ice saturation and sub-freezing temperature, rather than the abrupt phase change that occurs in pure media. Soil scientists have known for decades that this function, known as the soil freezing curve (SFC), is related to the soil water characteristic curve (SWCC) for unfrozen soils due to the analogous capillary and sorptive effects experienced during both soil freezing and drying. Herein we demonstrate that other factors beyond the SFC-SWCC relationship can influence the potential range over which pore water phase change occurs. In particular, we provide a theoretical extension for the functional form of the SFC based upon the presence of spatial heterogeneity in both soil thermal conductivity and the freezing point depression of water. We infer the functional form of the SFC from many abrupt-interface 1-D numerical simulations of heterogeneous systems with prescribed statistical distributions of water and soil properties. The proposed SFC paradigm extension has the appealing features that it (1) is determinable from measurable soil and water properties, (2) collapses into an abrupt phase transition for homogeneous media, (3) describes a wide range of heterogeneity within a single functional expression, and (4) replicates the observed hysteretic behavior of freeze-thaw cycles in soils.

SFCs are used in all the permafrost models that use a continuum phase-change criterion. Here, an efficient enthalpy-based continuum numerical approach is introduced for solving heat transfer problems with non-isothermal phase change. In order to simulate permafrost over time spans of several years, a robust and efficient model is required. In the present setting, the heat transfer problem is converted to a minimization problem, in which we minimize a potential function that characterizes the governing heat transfer

PDE within a time discrete framework. The use of the trust region minimization algorithm proves desirable due to the highly nonlinear energy functional which also involves non-convex terms induced by phase change. Results obtained show satisfactory agreement with existing analytical solutions. Moreover, the grid and timestep convergence studies conducted to examine the dependence of the solution on mesh and timestep sizes indicate robust convergence rates. This is the first application of trust region energy minimization algorithm in permafrost simulation.

The two-dimensional enthalpy-based numerical model with continuum phase-change is applied to study the effect of heterogeneity in the soil freezing point on conduction-driven talik formation. This model is rigorously verified against Lunardini's solution (Lunardini, 1981), which is an analytical solution of the Stefan Problem with a non-isothermal phase-change criterion. Stochastic realizations of spatially correlated distributed soil thermal parameter fields are generated using the geostatistical software library (GSLIB) for a variety of correlation lengths and variances in material properties. These are used as input to the 2-D permafrost model under fully saturated conditions. The simulation results indicate that local heterogeneities have conditional effects on the formation of unfrozen zones and, eventually, taliks. This influence is exacerbated under the presence of advective heat transfer, where small perturbations to the liquid water saturation can lead to preferential flow conduits. This work is extended by conducting sensitivity analysis to study the relative dependence of talik formation on different sources of heterogeneity (e.g. soil density and boundary conditions).

Acknowledgements

Firstly, I would like to express my gratitude and appreciation to my advisor, Dr. James R. Craig. Without his constant support and trust, this research would not have been possible. Words cannot describe the friendly and healthy environment he created in our research group that led to a desirable balance between my PhD and personal life. I have been extremely lucky to work with Dr. Craig and everyone in our research group throughout my PhD (Dr. Bryan Tolson, Dr. Juliane Mai, Robert Chlumsky, Élise Devoie, Konhee Lee, Sarah Grass, Mark Ranjram, Mahkameh Taheri, Shaghayegh Akbarpour Safsari, Leland Scantlebury, Genevieve Brown, Dr. Hongli Liu, Hongren Shen, and Ming Han).

Moreover, I would like to thank my dearest friend Dr. Mohammadreza Hirmand for his collaborative support through several conversations. I would also like to acknowledge the contribution and helpful field-related advice of Élise Devoie, which led me to conduct more realistic and practical simulations.

Many thanks to the wonderful friends that made this journey memorable, especially Roya Cody, who is one my first school friends who became family. I would like to express my deepest gratitude to Dr. Atena Pirayehgar, who is also my family and a great support during the toughest moments.

Also, I would like to thank my family, especially my beloved brother Ali, for their support and encouragement throughout my entire education.

Finally, a special thank you to my loving wife Parnia for her continued support, love, and patience. She has always had faith in me and what I do and is a great part of all I have achieved in my life.

To my lovely wife
Parnia

Table of Contents

List of Figures

List of Tables

Abbreviations

ET evapotranspiration 77

FEM finite element method 18

FTC freeze/thaw cycle 2, 8, 16, 18

GHG greenhouse gas iv, viii, 2, 8, 74

GLS Galerkin least squares 4

GSLIB geostatistical software library v, xiii, 25, 27, 76, 84, 110, 140

LAI leaf area index 77

MAE mean absolute error 82

NWT Northwest Territories 74, 75, 81, 112

PCHIP piecewise cubic Hermite interpolating polynomial 82

REV representative elementary volume 18, 110

SCRS Scotty Creek Research Station 73–76, 78, 81, 88, 100, 108, 110

SE standard error 82

SFC soil freezing curve iv, ix, xiii, xiv, 5, 29–31, 33, 34, 39–48, 110

SVAT soil-vegatation-atmosphere 77

SWCC soil water characteristic curve iv, 30, 31, 47, 48, 110

XFEM extended finite element method 4, 5, 17, 29, 33, 36, 37, 39, 110

Chapter 1

Introduction

1.1 Introduction

Regions exposed to subzero temperatures are highly influenced by seasonal freeze/thaw cycles (FTCs), and nearly a quarter of the exposed land on Earth is underlain by permafrost. The term 'permafrost' refers to soil or rock that remains below zero for at least two full years and is usually covered by a layer of soil. This mantling layer is called the soil active layer and is regularly exposed to freezing and thawing conditions on an annual basis (Quinton and Baltzer, 2013). The bottom elevation of permafrost is controlled by the geothermal gradient, average annual surface temperature, and advective heat transfer beneath permafrost body; and the surface elevation (referred to as the permafrost table) is limited by energy fluxes at the ground surface. The permafrost thickness is defined by the elevation difference between the permafrost table and base. A soil profile in permafrost regions is schematically shown as in Figure 1.1. Talik in general means unfrozen ground, but in permafrost terminology, it refers to a zone in permafrost environment that remains unfrozen. The hydrology and carbon balance of cold regions is strongly influenced by the presence of permafrost in the subsurface. Since the biological processes in these regions are highly sensitive to changes occurring in the permafrost FTCs (Belshe et al., 2012), any change in soil FTCs will disturb the carbon balance of the permafrost region. The drastic impacts of rapid climate change on the permafrost zones are becoming evident, as observed in an increase in carbon release rates, emergence of thermokarst lakes (Bouchard et al., 2017), changes in the discharge of Arctic rivers, and disappearance and shrinkage of Arctic lakes (White et al., 2007). Soil FTCs have a very important role in many processes and strongly influence the geo-mechanical, hydro-mechanical, and thermal properties of soil (Qi et al., 2006; Tang and Yan, 2014; Jamshidi et al., 2015); soil stability (Oztas and Fayetorbay, 2003; Kemper and Rosenau, 1986); greenhouse gas (GHG) emission (Kurganova et al., 2007); hydrology (Wang et al., 2009); and biological activity (Larsen et al., 2002; Teepe et al., 2001). The implications of these changes are still being investigated. In particular, the effect of local and mesoscale heterogeneity on permafrost thaw is poorly understood. It has been observed that the degradation of the permafrost table in the Arctic and sub-Arctic regions occurs variably in space. However, a gap exists in the literature on the impacts of heterogeneity on the long-term and short-term evolution of permafrost bodies (Ippisch, 2001). This local heterogeneity in soil properties or surface energetics may be a major driver of talik formation, a phenomenon that can impact landscape evolution, hydrologic connectivity, and GHG emission. Permafrost models which specially address the presence of spatial heterogeneity in soil and water properties may help to better understand these

impacts.

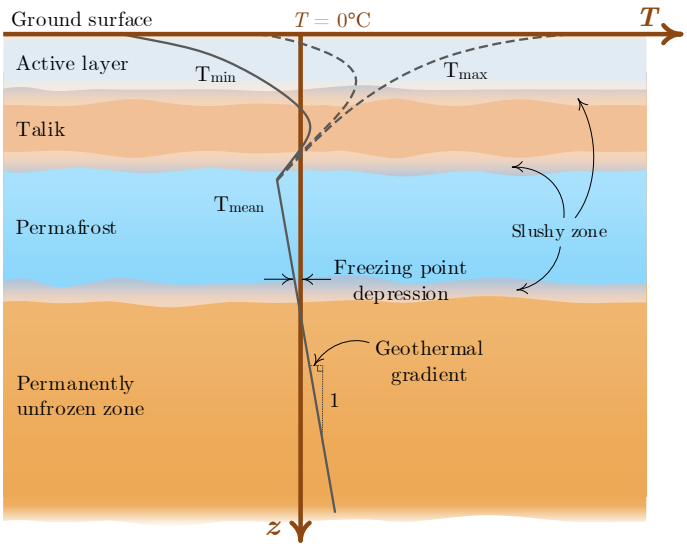

Figure 1.1 A schematic overview of soil profile in permafrost zones

1.2 Motivation and objectives

A proper representation of freeze/thaw processes in hydrological models is important for understanding the factors controlling permafrost thaw and predicting the impacts of climate change. Several numerical models have been developed for simulating soil-water-ice systems using different criteria for phase change phenomena (i.e. isothermal and non-isothermal) with different levels of complexity for various purposes (Chessa et al., 2002; Comini et al., 1974; Grenier et al., 2018; Painter et al., 2016). In this research, a stable and convergent model which can study the impact of soil-water-ice system heterogeneity on the short- and long-term evolution of permafrost bodies, formation of taliks, and lateral thaw of permafrost was developed. Moreover, the effect of lateral (perpendicular to the vertical cross-section) flow on talik formations has been investigated, which, to the best of the author's knowledge, has not been studied to this date. The previously developed models are mostly one-dimensional and often suffer from stability issues, which significantly constrain grid and timestep sizes; thus, here, an efficient, stable, and demonstrably convergent 2-D model capable of handling heterogeneity is developed to study and test

the effect of different sources of heterogeneity in soil-water-ice systems. In such statistical study, compared to a field scale simulation, the computational cost of the simulation sets are high due to the high volume of required stochastic realizations. This computational cost and run time of each simulation was the main limiting factor for not extending the model to three dimensions.

The overarching goal of this research is to study the effect of heterogeneity on the thermal behavior of soil-water-ice systems. In particular, we attempt to better understand (1) the influence of heterogeneity on upscaled soil freezing curves, (2) the impact of heterogeneity on talik formations and evolution, and (3) the relative importance of different types of heterogeneity on landscape permafrost evolution. To reach this goal, an enhanced numerically stable model is first developed and applied. This model is specifically designed to be applicable to heterogeneous media, where soil thermal and hydraulic properties (heat capacity, thermal conductivity, freezing point, and hydraulic conductivity) may be spatially variable. Two methods where deemed to be suitable options: the extended finite element method (XFEM), which explicitly models the frozen/unfrozen interface, and continuum enthalpy approach, which solves the energy balance in terms of enthalpy rather than temperature, and treats the freezing front as a continuum between frozen and unfrozen. Challenges associated with the XFEM include the stability of the method in heterogeneous media and the generation of complex interface geometries in 2-D problems. The stability issue can be tackled by implementing and testing stabilization methods, e.g. the Galerkin least squares (GLS) method, and complex interfaces can be handled, in part, by simplifying assumptions. The main issue with the models which treat phase change using a sharp interface criteria is that the criteria does not comply with the physics of phase change in soil, in which phase change generally occurs over a narrow range of temperatures. The enthalpy method requires a realistic freezing function; thus, a theoretical criterion has been developed for justifying the freezing temperature range of soils. After verifying the models' results against the existing analytical solutions for a simple case (i.e. the Stefan problem), the model is applied to a number of different field-scale problems. The developed tools and analysis of the simulation results are used to study the effect of heterogeneity on permafrost thaw.

This thesis has the following objectives:

1. Develop and evaluate a heterogeneity-informed theoretical criterion for determining the soil freezing function temperature range to be used in the continuum approach;

2. Develop and test a stable and robust 2-D freeze/thaw model, which supports arbitrary

heterogeneity, using the saturated continuum approach; and

3. Deploy the developed model to study the effect of heterogeneity on permafrost thaw. In particular, the following hypotheses are tested using the developed model:

   (a) Local scale soil heterogeneity may be an important driver of talik formation and evolution, and

   (b) The spatial distribution and correlation scale of soil and radiation heterogeneity has a non-negligible influence upon the evolution of discontinuous permafrost.

1.3 Thesis structure and statement of contribution

The work done for this doctoral research is structured in the following 5 chapters:

Chapter 2 summarizes a background of permafrost and its physics, a review on existing permafrost models, and permafrost model.

Chapter 3 consists of a paper published in *Advances in Water Resources* (2018) 111:319-328. The paper was co-authored by myself and my supervisor, Dr. James R. Craig, and Dr. Barret L. Kurylyk, Assistant Professor in the Department of Civil and Resource Engineering and Centre for Water Resources Studies at Dalhouse University. This paper presents a theoretical extension for the form of soil freezing curve (SFC) based on local spatial heterogeneity in soil. In this paper, I developed a 1-D XFEM formulation for simulating nonlinear heat transfer with phase change in soil. I implemented the model in a code written in Matlab for simulating different realizations of a heterogeneous soil column. I also prepared the manuscript. Dr. Craig provided the key idea of investigating the effect of local heterogeneity in soil on the shape of SFC. Moreover, he provided guidance through supervising the mathematical formulations and editing the manuscript. Dr. Kurylyk provided collaborative suggestions and guidance through editing the manuscript.

Chapter 4 includes a paper published in *Computational Geosciences* (2019). The paper is co-authored by myself, my supervisor, Dr. James R. Craig, and Dr. M. Reza Hirmand, post-doctoral fellow in the Department of Mechanical and Mechatronics Engineering at the University of Waterloo. In this paper, a robust, stable, and convergent trust region algorithm is presented for simulating nonlinear heat transfer with phase change using an enthalpy formulation. I implemented the developed algorithm in a computer program written in C++, designed and ran the test-case simulations, and wrote the manuscript. Dr.

Craig provided supervision through the development of the mathematical formulations and editing the manuscript. Dr. Hirmand provided collaborative support through suggesting the implementation of a trust region scheme, developing the algorithm, and editing the manuscript.

In Chapter 5, the effect of soil and surface heterogeneity on permafrost thaw is studied. A sensitivity analysis is performed using Sobol' sensitivity analysis scheme to identify the soil parameters that permafrost thaw is the most sensitive to. Finally, the effect of an adjacent hydrologic feature such as a channel fen on the lateral and vertical permafrost thaw is investigated.

Chapter 6 summarizes the conclusions of the research conducted in this dissertation.

Chapter 2

Background and literature review

2.1 Effect of permafrost thaw

As mentioned in Section 1.1, permafrost thaw has a very important role in many processes and strongly influences the geo-mechanical, hydro-mechanical, and thermal properties of soil.

2.1.1 Greenhouse gas (GHG) emission

The Earth's climate is determined by the amount of solar energy gained by its atmosphere. GHGs play a critical role in making the Earth habitable. GHGs enable the atmosphere to absorb reflected radiant heat and keep the Earth warm, which supports life. This effect is called the GHG effect. One of the most important causes of climate change is an increase in GHG release. This global warming has a significant impact on the changes in soils freeze/thaw cycles (FTCs) and permafrost thaw, but is also a byproduct of thaw due to carbon release. Due to decomposition of plants and microbial activity during the past thousands years, a significant amount of nitrogen and carbon has been trapped within and beneath the permafrost (Teepe et al., 2001; Zimov and Schuur, 2006). Carbon dioxide (CO_2) and nitrous oxide (N_2O) are two of the most important GHGs, and the emission of CO_2 and N_2O is increasing dramatically due to permafrost thaw. The subsequent gas release due to permafrost thaw, therefore, accelerates the climate change in a positive feedback loop.

2.1.2 Soil physical properties

It has been observed that presence or absence of ice changes the bulk physical properties of soils. Frozen soils are extremely stable, strong, and impervious (frozen saturated soil), and therefore, freezing soil is used as a technique to temporarily stabilize the soil in projects such as the construction of retaining walls, tunnels, and foundations. However, regular soil FTCs can cause significant changes in the soil's hyro- thermo- mechanical properties. As a case in point, Jamshidi et al. (2015) reported that soils' exposure to FTCs leads to a significant increase in its hydraulic permeability via cracking and pore separation. The degree of the increase in soil hydraulic conductivity depends on the characteristics of scenario of the FTC of the soil, i.e., the temperature range and number of FTCs. However, in some specific cases, FTC can lead to slight decrease in soil hydraulic conductivity (Hayashi et al., 2003). Conversely, the soil hydraulic conductivity in frozen saturated soils is near zero.

Eventually, as the ice lenses existing within the pores melt (due to thaw), the hydraulic conductivity of the soil increases significantly.

2.1.3 Hydrology

Freeze/thaw cycles influence the hydrogeological and hydrological processes controlled by the permafrost presence, specifically the annual evolution of the active layer. Permafrost thaw increases the total depth of active layer and talik, which leads to higher hydraulic conductivity and infiltrability of the soil. This happens because after thawing, the ice-lenses, which block the water path, do not exist in the pores (Walvoord and Kurylyk, 2016).

When the average temperature of a permafrost region raises, local taliks can form. In some cases, the talik connects the active layer to a permanently unfrozen zone at depth. Consequently, water may flow into the unfrozen soil through the taliks. These vertically forming taliks that connect the active layer and sub-permafrost region are known as open taliks. Heat advection through the open taliks accelerates the permafrost thaw rate. Consequently, new open taliks form, which facilitate ground/surface water exchange (Walvoord and Kurylyk, 2016). They can also open up larger connections between surface water features (Connon et al., 2014). Rowland et al. (2011) studied how advective heat transfer affects talik formation, which mostly happens beneath lakes and ponds. They indicated that sub-permafrost groundwater flow increases the localized degradation of permafrost. This may lead to shrinkage of lakes or bogs resting above the permafrost. As may be inferred from Figure 2.1, unfrozen holes in the permafrost layer can provide conduits for groundwater flow. In permafrost regions, groundwater flows in three different zones: (1) the active layer, (2) the year-round unfrozen zones within the permafrost (taliks), and (3) the permanently unfrozen zone beneath the permafrost. The flows within these zones are known as supra-permafrost groundwater, in-permafrost groundwater, and sub-permafrost groundwater, respectively (Kurylyk et al., 2014).

The active layer plays the most important role in the runoff process regardless of the variation of seasonal flood runoff levels (Hayashi et al., 2003). Wang et al. (2009) reported that in their case study (Qinghai-Tibet plateau) the direct runoff ratio has minimal influence and the precipitation has little effect on the total annual river runoff. Rather, the effect of the temperature of active layer is dominant. Walvoord et al. (2012) recognized that the understanding of talik formation and its morphology is important because the

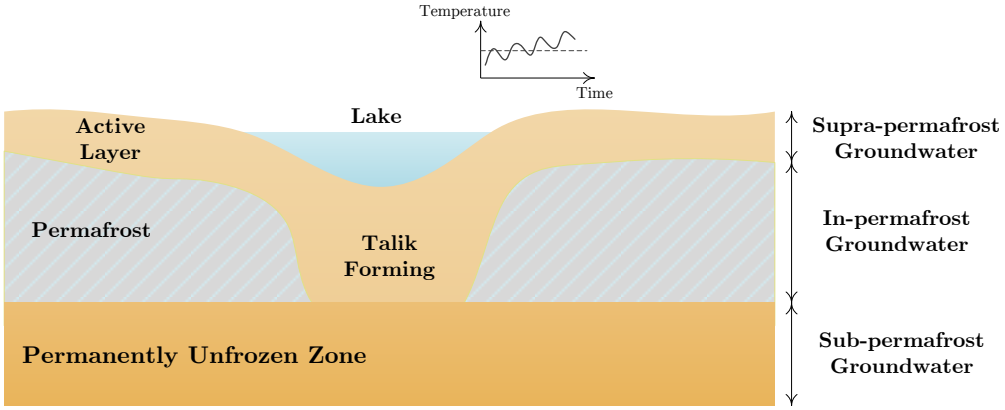

Figure 2.1 Talik forming in permafrost

groundwater recharge and discharge mostly occurs through open taliks. Here, we recognize that the formation of taliks may be, in part, influenced by local heterogeneity in soil characteristics and energy budget.

2.2 Physics of permafrost

Permafrost evolution is controlled by (1) the availability and movement of water in the pore-space of soil and (2) the transfer of energy between the soil matrix, ice, water, and, (most notably) in phase change. In heat transfer problems, it is essential to distinguish between three different types of heat transfer: conduction, convection, and radiation. Heat transfer via conduction takes place from a higher temperature zone to a lower one by kinetic motion or impact of molecules. This mechanism is the dominant mode of heat transfer in solids. Convection is a type of heat transfer that is caused by the relative motion of fluid with respect to the solid surface. In this type of heat transfer, fluid flow is coupled with the heat transfer because the velocity of the fluid comes to action. If the motion is caused by the buoyancy effects, which results from density difference of fluids with different temperatures, the heat transfer is called natural convection. However, if the motion of the fluid is externally induced, the heat transfer is called forced convection or advection in the case of transport of energy due to pressure gradient induced groundwater flow. Thermal radiation is a type of heat transfer which occurs via electromagnetic waves emitted from material's body due to its internal energy variation (Miller, 2012).

The freezing and thawing of porous media experiencing sub-zero temperature has an

indirect influence on the conductive heat transfer because the thermal properties of frozen soil (e.g. thermal conductivity and bulk heat capacity) are different from that of thawed soil. Ice formation also affects advective heat transfer because ice lenses can block the pores, and, consequently, the hydraulic conductivity of the soil decreases. In addition, note that water can migrate towards freezing front (freezing reduces pore pressure by inducing a pressure gradient). Since advective heat transfer depends on the groundwater flow velocity, this type of heat transfer is often restricted due to ice formation.

2.2.1 Governing equations

The governing equations of heat and mass transfer in permafrost systems are the equations of continuity (mass balance) and energy conservation. Here, the flow is considered incompressible and non-viscous, and the following equations are based on the same assumption.

Conservation of mass: The mass balance principal or the continuity equation states: in a fixed volume, the rate of change of mass with respect to time is equal to the net rate of flow through the boundaries (Reddy and Gartling, 2010). The continuity equation for flows in porous media is represented by the Richards' equation, which can be defined as

$$\frac{\partial \vartheta}{\partial t} = -\nabla \cdot \mathbf{j}, \tag{2.1}$$

$$\mathbf{j} = -\lambda \nabla \Phi, \tag{2.2}$$

$$\Phi = p + z, \tag{2.3}$$

in which ϑ $[-]$ is the volumetric water content, $\mathbf{j}$ $[\mathrm{L}^1\mathrm{T}^{-1}]$ is the water flux (discharge per unit area), λ $[\mathrm{L}^1\mathrm{T}^{-1}]$ is the isotropic hydraulic conductivity, Φ $[\mathrm{L}^1]$ is the hydraulic head, p $[\mathrm{L}^1]$ is the pressure head, and z $[\mathrm{L}^1]$ is the elevation. It is assumed that flow is driven by potential gradient using Buckingham-Darcy law (Equation 2.2). For saturated systems with phase change, Equation 2.1 can be simplified to:

$$\frac{\partial \vartheta}{\partial \Phi} \frac{\partial \Phi}{\partial t} = \nabla \cdot (\lambda \nabla \Phi)\,. \tag{2.4}$$

Conservation of energy: The first law of thermodynamics states that the time rate of change of a system's total energy is equal to the sum of the net rate of work done by the forces and the net heat transfer to the system. This law can be expressed in a conservation

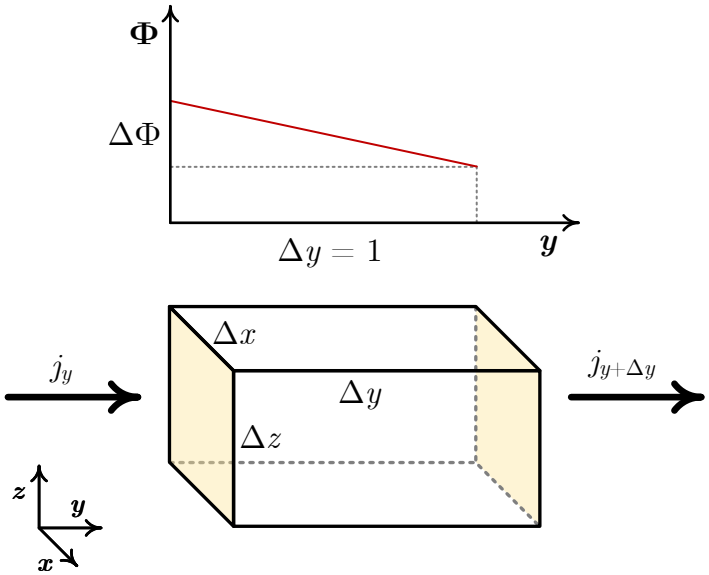

Figure 2.2 Lateral (y-direction) flow description

form for porous media as follows:

$$\frac{\partial}{\partial t}\left(\overline{\rho c}T\right) + \nabla\cdot\left(\rho_{\mathrm{w}} c_{\mathrm{w}} \mathbf{v} T\right) = -\nabla\cdot\mathbf{q} + \mathrm{h_b}, \tag{2.5}$$

$$\mathbf{q} = -\overline{K}\nabla T, \tag{2.6}$$

where $\mathbf{q}$ $[\mathrm{M^1T^{-1}\Theta^{-3}}]$ is the heat flux vector, $\mathbf{v}$ $\left[\mathrm{LT^{-1}}\right]$ is the velocity vector, and $\mathrm{h_b}$ $[\mathrm{M^1L^{-1}T^{-3}}]$ is an internal heat source (e.g. latent heat from phase change and lateral advective heat transfer due to in-to page water flow); ρ_{w} $[\mathrm{ML^{-3}}]$ and c_{w} $[\mathrm{L^2T^{-2}\Theta^{-1}}]$ are the density and specific heat capacity of water; whereas, $\overline{\rho c}$ $[\mathrm{M^1L^2T^{-2}\Theta^{-1}}]$ and $\overline{K}$ $[\mathrm{M^1L^1T^{-3}\Theta^{-1}}]$ are the effective bulk heat capacity and isotropic thermal conductivity of the soil-water-ice media, respectively. In this research, conductive heat transfer assumed to be the only source of heat transfer in xz-plane and advective heat transfer in y direction (into plane). Consequently, the equation of energy conservation would be sufficient to simulate the freeze/thaw of soil. The energy conservation law for such system is expressed as

$$\frac{\partial}{\partial t}\left(\overline{\rho c}T\right) = \frac{\partial}{\partial x}\left(\overline{K}\frac{\partial T}{\partial x}\right) + \frac{\partial}{\partial z}\left(\overline{K}\frac{\partial T}{\partial z}\right) - \frac{\partial}{\partial y}\left(\rho_{\mathrm{w}} c_{\mathrm{w}} j_y T\right), \tag{2.7}$$

$$j_y = -\lambda\frac{\partial \Phi}{\partial y}, \tag{2.8}$$

where j_y [$\mathrm{L^1T^{-1}}$] is the into-plane water flux, and $\partial\Phi/\partial y$ denotes the slope of ground in y direction. Assuming a unit length in y direction, Equation 2.7 can be simplified to:

$$\frac{\partial}{\partial t}\left(\overline{\rho c}T\right) = \frac{\partial}{\partial x}\left(\overline{K}\frac{\partial T}{\partial x}\right) + \frac{\partial}{\partial z}\left(\overline{K}\frac{\partial T}{\partial z}\right) + \rho_{\mathrm{w}} c_{\mathrm{w}} \lambda \alpha_y \Delta T, \tag{2.9}$$

where α_y is the slope in y direction, and ΔT [Θ] is the temperature difference between the ambient soil and flowing water.

The general boundary and initial conditions of this problem are

$$T = \tilde{T}\left(\mathbf{x}, t\right) \qquad \text{on } \Gamma_{\mathrm{D}}, \tag{2.10}$$

$$-\overline{K}\nabla T \cdot \mathbf{n} = \tilde{\mathbf{q}}\left(\mathbf{x}, t\right) \qquad \text{on } \Gamma_{\mathrm{N}}, \tag{2.11}$$

$$T = T_0\left(\mathbf{x}, 0\right) \qquad \text{over } \Omega, \text{ at } t = 0, \tag{2.12}$$

where $\tilde{T}\left(\mathbf{x}, t\right)$ and $\tilde{\mathbf{q}}\left(\mathbf{x}, t\right)$ are, the temperature and heat flux over the Dirichlet (Γ_{D}) and Neumann (Γ_{N}) boundaries, respectively, and $\mathbf{n}$ is the vector normal to the Neumann boundary.

Soil-water-ice system apparent properties

As soil is a composite material, the thermal properties of soil are defined in terms of the properties of its constituents. The properties used in the previous equations are defined as follows:

Saturated isotropic hydraulic conductivity $\boldsymbol{\lambda}$: The hydraulic conductivity of porous media indicates the ability of the porous media to transport water, and its dimension is $\mathrm{L^1T^{-1}}$. Soil hydraulic conductivity is often expressed as a tensor since hydraulic conductivity of porous media can differ in difference directions due to the anisotropy of the media. Here, it is assumed that soil is isotropic.

Isotropic thermal conductivity $\boldsymbol{K}$: This property indicates the ability of a material to conduct heat, and its dimension is $\mathrm{M^1L^1T^{-3}\Theta^{-1}}$. The average isotropic thermal conductivity of the soil-water-ice system can be calculated based on three volumetric averaging

methods: arithmetic, harmonic, and geometric methods, which are calculated as follows:

$$\overline{K}_{\mathrm{a}} = n(S_{\mathrm{w}}K_{\mathrm{w}} + S_{\mathrm{i}}K_{\mathrm{i}}) + (1-n)K_{\mathrm{s}}, \tag{2.13}$$

$$\frac{1}{\overline{K}_{\mathrm{h}}} = \frac{1}{nS_{\mathrm{w}}K_{\mathrm{w}}} + \frac{1}{nS_{\mathrm{i}}K_{\mathrm{i}}} + \frac{1}{(1-n)K_{\mathrm{s}}}, \tag{2.14}$$

$$\overline{K}_{\mathrm{g}} = {K_{\mathrm{w}}}^{S_{\mathrm{w}}n}{K_{\mathrm{i}}}^{S_{\mathrm{i}}n}K_{\mathrm{s}}^{(1-n)}, \tag{2.15}$$

where, n, S, ρ, c, and k are the porosity, saturation, density, bulk heat capacity, and thermal conductivity, respectively. The 'w', 'i', and 's' subscripts denote the parameters of water, ice, and soil phases. In Equation 2.13 the assumption is that the soil components are parallel thermal resistors, which leads to a linear relation between the thermal conductivities of the soil components. If the medium is considered as thermal resistors in series, the representative thermal conductivity can be calculated by Equation 2.14, which defines a volumetric harmonic relation between the soil constituents. For the case that multi-dimensional heat transfer occurs, the orientation of the soil constituents cannot be conceptualized either in parallel or in series; thus, geometric averaging is preferable and can be calculated by Equation 2.15 (Walvoord and Kurylyk, 2016). Clauser and Huenges (1999) also suggested that geometric mean is more appropriate than the arithmetic mean for soil thermal conductivity. Similar to soil hydraulic conductivity, thermal conductivity is often expressed as a tensor; however, due to isotropic assumption, soil thermal conductivity is represented as a scalar.

Specific heat capacity c: Specific heat capacity is an intrinsic property of a substance that measures the amount of energy needed to raise the temperature a unit mass of that substance by one Kelvin without phase change. The dimension of the specific heat capacity is $\mathrm{M^1L^2T^{-2}\Theta^{-1}}$. Since the effective bulk heat capacity of soil ($\overline{\rho c}$) is independent of the orientation of the soil components, volumetric arithmetic averaging can typically be used in calculating the representative bulk heat capacity, which is expressed as below:

$$\overline{\rho c}_{\mathrm{a}} = n(S_{\mathrm{w}}\rho_{\mathrm{w}}c_{\mathrm{w}} + S_{\mathrm{i}}\rho_{\mathrm{i}}c_{\mathrm{i}}) + (1-n)\rho_{\mathrm{s}}c_{\mathrm{s}}. \tag{2.16}$$

Latent heat L_{f}: The latent heat of fusion is the amount of energy required for occurrence of phase change in a unit mass of a substance without any change in temperature. The dimension of this property is $\mathrm{M^1L^2T^{-2}}$.

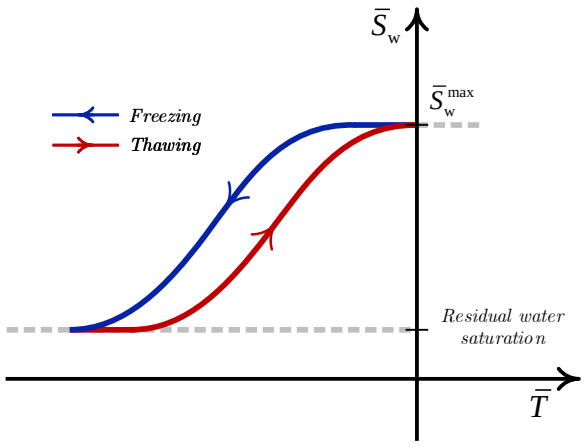

Figure 2.3 Hysteretic freezing function expressed in terms of water saturation (S_w) and soil temperature (T)

The soil freezing curve: The term 'phase' is typically used to determine a region in space throughout which the physical properties are uniform (Tester and Modell, 1997). Regarding this definition, the different states of a material (i.e. gas, liquid, and solid) are considered as different phases of it. Permafrost systems can consist of four different components: soil, liquid water, ice, and gas. This composition makes the soil freezing characteristics complicated. The complexity stems from the dependency of soil properties and water freezing temperature on factors such as air pressure and water content. To determine the soil freezing characteristics in the lab, it is essential to measure the unfrozen water potential (i.e. water pressure) and mass fraction simultaneously (Spaans and Baker, 1996). During soil freezing process, water and ice coexist at the temperatures below the soil's freezing point, and the characteristics of this coexistence is strongly influenced by temperature. As soil temperature decreases during freezing, the water pressure becomes more negative, which leads to a drop in the soil's water content. Water pressure (Ψ_w) and ice pressure (Ψ_i) at the freezing front can be related to the following differential equation, which is called the Clapeyron equation (Spaans and Baker, 1996). A detailed derivation of the generalized Clapeyron equation is demonstrated by Kay and Groenevelt (1974); Groenevelt and Kay (1974).

$$\frac{1}{\rho_w} dp_w - \frac{1}{\rho_i} dp_i = \frac{L_f}{T} dT, \tag{2.17}$$

in which p is the pressure, ρ is the density, and T is the temperature at the freezing front in Kelvin (K). This equation is an approximation that may be only valid for pure water at the freezing front when the temperature is close to the water's freezing point. Ice potential p_{i} is often considered negligible, and most of the existing models do not account for it. In the general case of frozen soil, this assumption may not be justified. The water pressure assuming a negligible ice pressure can be directly calculated as follows:

$$p_{\mathrm{w}} = \rho_{\mathrm{w}} L_{\mathrm{f}} \ln \frac{T}{T_{\mathrm{m}}}, \tag{2.18}$$

where T_{m} is the pure water melting point in Kelvin (273.15 K at atmospheric pressure).

Koopmans and Miller (1966) noted that soil freeze/thaw is a hysteretic process. In a hysteretic freeze/thaw process, thawing and freezing do not occur via the same path (Figure 2.3), which means that for the same temperature, we may expect different freezing curves under freezing and thawing conditions. Flerchinger et al. (2006) demonstrated a similarity between the soil freeze/thaw and drying/wetting processes. The same hysteretic behavior is observed in the soil drying and wetting processes for pressure-water saturation relation (Spaans and Baker, 1996). Smerdon and Mendoza (2010) studied the hysteretic behaviour of riparian peatlands in the Western Boreal Forest of Canada and reported that the hysteretic behaviour occurs potentially due to heterogeneity in porosity of the soil and different thermal properties of frozen and thawed soil. They also demonstrated through sensitivity analyses that assuming a freezing range between -0.25 to $-2\,^{\circ}\mathrm{C}$ leads to more accurate simulation results. Rubio et al. (2011) conducted a study in a laboratory scale investigating the hysteretic characteristics of the thermal properties of a silt loam soil, and noted important controlling factors on the hysteretic behaviour such as the level of saturation and the shape of the layer of water surrounding soil particles.

2.3 Modeling permafrost

To understand and predict the impact of FTCs in porous media, it is common to deploy numerical models. Existing models of solidification/liquefaction, freeze/thaw, or general phase change incorporate methods that tend to fall into two main categories: front tracking and continuum methods. The front tracking approach is a classic free boundary problem based on solving the governing equations for temperature in the frozen vs. unfrozen regions of the domain and tracking the location of the sharp interface in each timestep, typically

by applying the Stefan condition at the interface. The Stefan condition, which arises from an energy balance at the interface at the interface, defines the local velocity of the interface based on the heat flux jump at the sides of it. The sharp interface causes a discontinuity in the derivatives of the temperature field, which can be addressed using various techniques, such as extended finite element method (XFEM) (Chessa et al., 2002; Salvatori and Tosi, 2009), adaptive mesh methods (Khoei, 2005), or the phase-field method, in which the interface is not sharp but tracked explicitly (Wheeler et al., 1992). Because this method predicts the location of the interface precisely, it is popular in solidification problems, in which the exact location of the interface between the solid and liquid phases is important. The issue with this method is that it may be impossible to track multiple sharp interfaces of complex shapes in 2-D and 3-D problems; alternately, there may not be any sharp interfaces. This is generally the case for freeze/thaw of soil, in which the phase change is a non-isothermal process due to, in part, local variability in the matric potential of frozen soil. The non-isothermal freezing leads to the presence of a slushy zone consisting of frozen and unfrozen water. The spatial variability in water pressure, water quality, and soil properties have influence on the characteristics of the slushy zone. To simulate the slushy zone evolution, a continuum approach is typically implemented. In this approach, a single governing equation is solved for heat transfer with two phases, and the transition between the fully frozen and fully thawed is zones is represented by a temperature-ice saturation relation called the freezing function. Either temperature or enthalpy may be used as the state variable. Here, the Stefan condition is implicitly satisfied at the interface, and the sharp interface, a singularity in the sharp interface numerical solution, is smoothed out and needs no special accommodation. This continuum approach is the one most commonly employed in practical models of freeze/thaw in porous media (e.g., Voller et al., 1987; Swaminathan and Voller, 1992; Alexiades and Solomon, 1993; Nedjar, 2002), in part because it is the most numerically stable. A drawback of this approach is that the temperature range used in the soil freezing function lacks a rigorous and reasonable justification at the common scales of application, particularly when sub-grid scale heterogeneity is present. In most of the literature, a continuous function is used, often with the slushy zone present over a 1 to 4°C temperature range (e.g., McKenzie et al., 2007). It is suggested here that a useful physically-based rationale for defining the characteristics of the slushy zone may be found by invoking the presence of soil-water-ice system heterogeneities. The aqueous heterogeneity (i.e. spatial variation in the freezing point temperature) is related to solute concentration and water matric potential (Flerchinger et al., 2006; Bao et al., 2016), and the soil heterogeneity is ascribed to natural spatial variation in thermal diffusivity below

the scale of the representative elementary volume (REV).

Permafrost or phase change models are introduced and developed for different dimensions with levels of complexities. The classic two-phase solidification-liquefaction problem (or in general a moving-boundary problem) is called the Stefan Problem, for which an analytical solution exists. The Stefan Problem was first introduced by Josef Stefan (a Slovenian physicist), whose research interest was the polar ice cap melt. The history and review of the Stefan Problem is covered by Hill (1987). Evans (1951) presented the existence of a solution for the Stefan Problem, and Douglas (1956) showed the uniqueness of the solution. An analytical solution for this problem (the Neumann solution) is presented in explicit closed-form equations, which can be found in the studies done by Solomon (1966); Rathjen and Jiji (1971) and Crank (1999*a*). Although an analytical solution exists for variations of the Stefan Problem, the solutions are restricted to very simple configurations. The problems for which the analytical solutions are presented are either one-dimensional (Hill, 1987; Alexiades and Solomon, 1993) or two-dimensional with symmetric geometry and boundary conditions, e.g., a two-dimensional corner freezing problem presented by Rathjen and Jiji (1971). The simplicity associated with the problems with analytical solutions obliges us to use numerical treatments for all other complicated problems. These solutions, however, are useful for benchmarking (Kurylyk and Watanabe, 2013). Many numerical models were presented to simulate the soil freezing and thawing processes and combine the soil freeze/thaw with the flow models of porewater.

An early permafrost model presented was presented by Hwang et al. (1971) to study the interaction of structural foundations and permafrost. The two-dimensional model implements the finite element method (FEM) and considers latent heat as a heat source varying in space and time. The formulation was verified by checking results with the Neumann solution (Solomon, 1966). In addition, the versatility of the approach was demonstrated by illustrating the capability of the method to predict results for nontrivial problems of practical significance.

Since then, multiple researchers have developed one-dimensional permafrost models, often coupled to soil-vegetation atmosphere transfer (SVAT) models for simulation of climate and weather. Flerchinger (2000) introduced the simultaneous heat and water (SHAW) model, which is a representative of many 1-D vertical models in the literature. The model, which was originally developed by Flerchinger and Saxton (1989) to model soil FTCs, simulates water, heat, and solute transfer in a one-dimensional soil profile. As it is shown in Figure 2.4, the model one-dimensional configuration is represented by vegetation canopy,

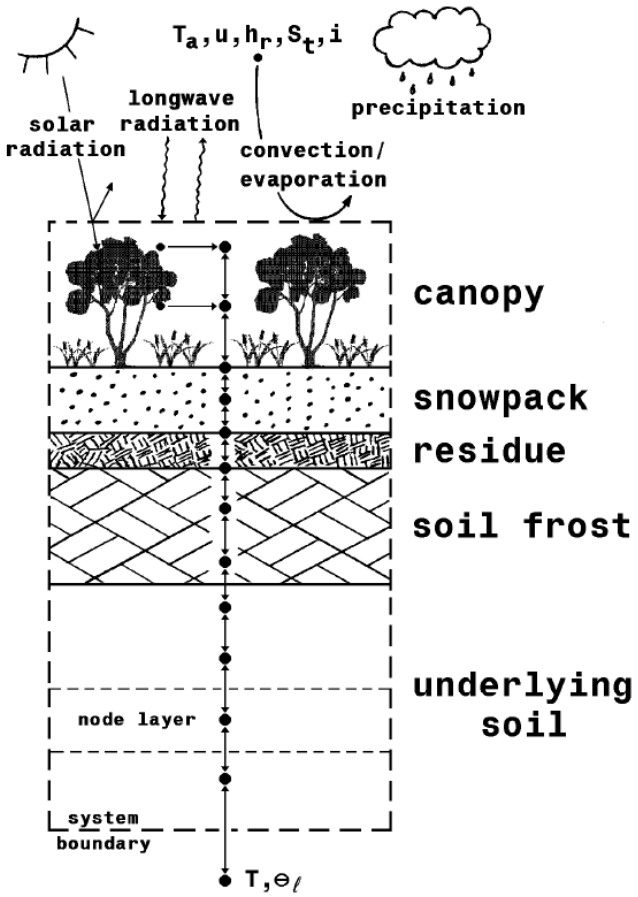

Figure 2.4 The physical system description in SHAW model (Flerchinger, 2000)

snow cover, residue, and a certain depth of soil. A layered system is considered from plant canopy to the specified soil depth, and each node layer is represented by a node. The upper boundary is subjected to a daily or hourly air temperature, wind speed, precipitation, and solar radiation. The input energy from the upper boundary and the soil conditions in the lower boundary determine the heat and water fluxes into the system. The balance equations at each node are solved in an implicit finite difference scheme. After solving the equations at each timestep, the energy, moisture and solute fluxes are interpolated between the nodes.

Although SHAW and similar 1D models are capable of modeling freeze/thaw in soil, they are not be entirely adequate for modeling of permafrost in some systems because of its one-dimensional nature. For instance, they cannot handle the local influence of lateral heterogeneity or collective melt. Similar one-dimensional models include the models introduced by Jansson and Karlberg (2004) (COUP) , Zhang et al. (2003) (NEST), Hansson

et al. (2004), and White and Oostrom (2006) (STOMP) suffer from the same issue. Other models have extended the same model configuration to simulate carbon and nitrogen cycles in soil (Jansson and Karlberg, 2004) or subsurface transport (White and Oostrom, 2006).

Hansson et al. (2004) introduced a numerically stable mass and energy transport model to deal with the phase change in soil. This one-dimensional model is developed based on HYDRUS-1D model (Šimunek et al., 1998). In the model, a modified Richards' equation is used to describe the variably saturated water flow. Due to the variability of the parameters used in this model in space and time, the equations (Richards' and heat transfer) are highly nonlinear. An implicit finite difference scheme was used for solving the modified Richard's equation and discretization of the heat transfer equation in time domain. FEM was used for the discretization of the heat transfer equation in space domain. The model was verified by a laboratory freezing experiment and applied to a Swedish road to perform a long-term analysis. As Ippisch (2001) reported, the vapor transport coupling has minor impacts on the results.

Several researchers developed 2- and 3-D models for a realistic representation of permafrost. Ippisch (2001) developed a 2- and 3-D numerical solver for heat, water, and gas transport (a three-phase model), considering soil freeze/thaw. The model has been applied to soils at laboratory to plot scale. A finite volume and finite difference scheme is used in discretization of space and time domains, respectively. The results of this model has been compared with a real permafrost site data and showed satisfying agreement. The simulation results were sensitive to a slight change in water transport parameters. However, the model was used to demonstrate that vapor transport (gas phase) is typically unimportant. Moreover, considering solute transport was shown to have almost no effect on the simulation results. There was an considerable deviation between calculated temperatures and field data, which was attributed to the heterogeneity of the soil profile or, in general, heterogeneities of the parameters used in calculations. This study suggests that consideration of the heterogeneity is important.

In order to simulate effect of climate and environmental changes or constructed facilities (e.g., foundation of structures, pipelines), Krane (2007) introduced TEMP/W model, which is a two-dimensional simulator based on FEM. This model is basically an add-on for GEO-SLOPE model, which is a geotechnical modeling environment.

FEFLOW with piFreeze (DHI-WAYS, 2016) module and HydroGeoSphere (Schilling et al., 2019) are two of the powerful 3-D models that can model simulate soil freeze/thaw process coupled with unsaturated fluid flow. Langford et al. (2019) used FEFLOW with

piFreeze plug-in for their field-scale simulations, and deployed a spin-up initial condition implementation for a more accurate validation with field data. Schilling et al. (2019) efficiently integrated HydroGeoSphere with winter hydrolocial processes in a physically-based manner for a catchment-scale problem.

Finally, the SUTRA-ICE model was introduced by McKenzie et al. (2007). This model is a modification to the SUTRA model, which is a computer program that simulates fluid transport in a saturated or unsaturated subsurface environment (first released by Voss, 1984). SUTRA-ICE can effectively simulate the phase change of porewater to ice occurring over a rage of temperatures. McKenzie et al. (2007); Rühaak et al. (2015); **?** studied the effect of soil freeze on the thermal profile of peat bogs using SUTRA-ICE.

In this research, first, a computer program is developed in C++ for modeling permafrost in heterogeneous media. An important step towards a powerful and robust numerical model is convergence study, which lacks in most of the reviewed models. The convergency of this model is examined via spatial and temporal convergence studies to ensure that acceptable convergence rates are obtained. The details of the development, derivations of the equations, spatial and temporal convergence analyses, and verification against the analytical solution are elaborated on in Chapter 4. This model is also successfully validated against field data (Section 5.3).

2.4 Soil heterogeneity

Heterogeneity in the field of hydrology has always been of importance (Wood et al., 1988; Leblanc et al., 1991; Entekhabi and Eagleson, 1989), and several studies have been conducted to investigate the effect of soil heterogeneity and spatial variability on surface and subsurface flows (Russo and Bresler, 1981; Mallants et al., 1996; Rehfeldt et al., 1992; Mohanty et al., 1991; Woodbury and Sudicky, 1991). Permafrost projections are estimated by numerical simulations. These estimations are dependent upon the representation of the soil-water-ice system (Harp et al., 2016). The soil-water-ice system is often considered homogeneous (Vogel et al., 2019; Lamontagne-Hallé et al., 2018; Langford et al., 2019) or layered (Signorelli et al., 2007), which is a reduced form of characterizing a 2- or 3-D heterogeneous system for the sake of simplicity. However, due to unpredictable physical processes, soils or rock masses in an aquifer or reservoir become heterogeneous; thus, spatial variability is induced to their properties (i.e. physical, mechanical, hydraulic, and thermal) (Bundschuh, 2010). Modelers can either use averaged or representative properties or

explicitly simulate heterogeneity of soil. The traditional way of simulating soil systems in permafrost models is to use homogeneous properties. Bundschuh (2010) reviewed different methods of averaging heterogeneous geological properties. Considering soil as a homogeneous composite material has been justified by testing the thermal behavior of a block of soil as a thermal resistor and showing that the block can be represented by equivalent homogeneous thermal properties (i.e. thermal conductivity and heat capacity).

Atchley et al. (2015) developed a data-informed 1-D model to calibrate their model parameters in an iterative manner using homogeneous parameters as a start point. They illustrated that the data-informed adjustments creates an improved and robust system response. Harp et al. (2016) extended the work done by Atchley et al. (2015) studied the effect of soil property uncertainty on the projections of permafrost thaw. They showed that soil property uncertainty has significant effects on the projections of annual permafrost depth and active layer thickness, minor effects on the Stefan number estimations, and minimal effects on the soil moisture predictions. Schneider et al. (2012) investigated the effect of surface and subsurface heterogeneity on the observed temperatures at an alpine permafrost site. Based on their 8-year temperature observation, assuming a relatively equal angle, exposure, and micro-climate for all sites, the responses of the thermal regimes were different, and a non-uniform temperature data was recorded.

Permafrost systems are highly heterogeneous, yet the implications of heterogeneity are still unclear and understudied. Particularly, there has been little work done regarding the effect of heterogeneity on permafrost thaw patterns and talik formations (Atchley et al., 2015; Adams and Gelhar, 1992; Shen et al., 1995; Harp et al., 2016; Signorelli et al., 2007; Rehfeldt et al., 1992; Ippisch, 2001).

2.4.1 Geostatistical representation of heterogeneity

Geostatistics is defined as "the study of phenomena that fluctuate in space" (Olea, 1991). The Geostatistical tools help interpret and model spatial variability by characterizing the uncertainty around some unknown using a probability distribution (Deutsch and Journel, 1997). In Geostatistics, a property field (e.g. thermal conductivity) can be characterized as a spatially correlated random field. The most common description of such field is a semivariogram, $\gamma(\mathbf{h})$, which is half of a function (variogram) that describes the spatial variability, interdependence, and the fluctuation scale of a random function, $Z(\mathbf{x})$, representing the variance of the property as a function of distance between any two points in

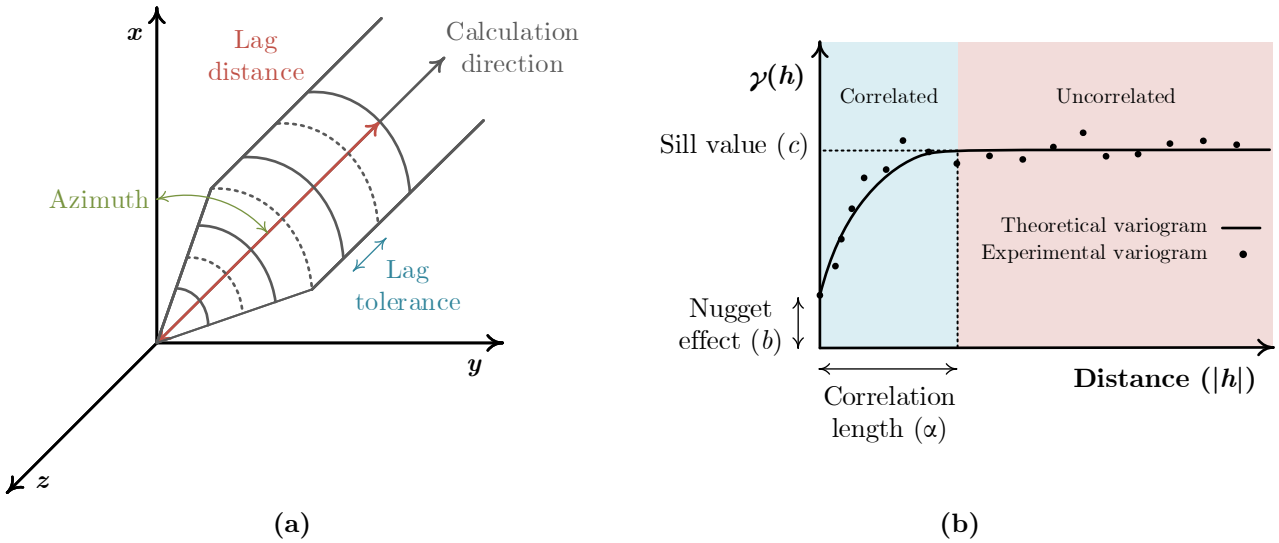

Figure 2.5 Geostatistics definitions: (a) Lag setting in variogram calculation (b) Variogram schematic: Sill value is the maximum variance, where the variogram reaches plateau, and nugget effect (b) denotes the variability in small scales

the field (study area, Ω). A variogram may be estimated from an existing field, $Z(\mathbf{x})$, as:

$$\gamma(\mathbf{h}) = \frac{1}{2N} \sum_{i=1}^{N} [Z(\mathbf{x}_i) - Z(\mathbf{x}_i + \mathbf{h})]^2, \tag{2.19}$$

in which N is the number of lag points and $\mathbf{h}$ (the lag vector) is a vector denoting the distance from the point at which spatial variability is being calculated and is specified by a direction and a tolerance value (Figure 2.5a). Lag tolerance defines the minimum distance of the data point pairs that are included in the variogram calculation. The length of $\mathbf{h}$ must be greater or equal to the shortest distance between any pairs.

To generate spatial fields with different spatial correlation, theoretical variograms can be defined in various forms depending upon the nature of the variability of the random property of the study field. The three most common used variograms, the spherical, expo-

nential, and Gaussian variograms, are respectively expressed as

$$\gamma(\mathbf{h}) = \begin{cases} b + c\left(\frac{3\mathbf{h}}{\alpha} - \frac{1}{2}\left(\frac{\mathbf{h}}{\alpha}\right)^3\right) & \text{if } |\mathbf{h}| < \alpha \\ c & \text{if } |\mathbf{h}| > \alpha \end{cases}, \tag{2.20}$$

$$\gamma(\mathbf{h}) = b + c\left[1 - \exp\left(\frac{-\mathbf{h}}{\alpha}\right)\right], \tag{2.21}$$

$$\gamma(\mathbf{h}) = b + c\left[1 - \exp\left(-\left(\frac{\mathbf{h}}{\alpha}\right)^2\right)\right], \tag{2.22}$$

where b is the nugget effect, a is the correlation length, and c is the sill value (the maximum variance, where the variogram reaches plateau). Sill value is equal to the variance of entire field without acknowledging spatial structure.

As illustrated in Figure 2.5a, direction is one the characteristics of a variogram; thus, to specify a 3-D spatial variability, three variograms for the three orthogonal directions may be defined; directional anisotropy can be induced by considering a different correlation length for different directions (Simms, 2012).

To study the effect of heterogeneity on permafrost, the characterization of the heterogeneous medium must first be specified. Here, we assume different forms of heterogeneity in soil: porosity, density, thermal conductivity, and hydraulic conductivity. To generate a consistent heterogeneous soil realization, the correlations between soil properties must be respected, i.e. we could not have high porosity soil with low hydraulic conductivity. This is possible by relying upon pedotransfer functions, which are empirical functions linking soil properties to some basic shared characteristics, such as bulk density. Here, the following two functions are used to express thermal conductivity, $K\left[\mathrm{W.m.^{-1}K^{-1}}\right]$, (Lawrence et al., 2018) and hydraulic conductivity, $\lambda\left[\mathrm{m.s^{-1}}\right]$, (Liu and Lennartz, 2018) of peat soil in terms of the bulk density of soil, $\rho_\mathrm{s}\left[\mathrm{kg.m^{-3}}\right]$:

$$K = \frac{0.135\rho_\mathrm{s} + 64.7}{2700 - 0.947\rho_\mathrm{s}}, \tag{2.23}$$

$$\log_{10}(\lambda) = 3.491 - 15.802\rho_\mathrm{s} + 19.552\rho_\mathrm{s}^2. \tag{2.24}$$

Thus, we can generate ρ_s field and calculate resultant λ and K fields.

Quantifying the effect of heterogeneity in heterogeneous soil-water-ice systems is challenging because there is little work done characterizing the uncertainties in the spatial

Table 2.1 Geostatistical model parameters

Property	Value
Variogram type	Exponential
Sill value	0.2
Nugget	0.0
Vertical correlation length	2.0 m
Horizontal correlation length	12.0 m

properties of peat, i.e. the sill value (c) or correlation length (a) of the experimental variogram. Mallants et al. (1996) studied the effect of heterogeneity on unsaturated soil hydraulic properties in a layered soil system for three different depths (0.1 m, 0.5 m, and 0.9 m), and found out that correlation length of cross-correlated lags calculated by a spherical theoretical model was very close to that of direct semivariograms. In the past, the permafrost modeling was done using completely homogeneous properties (McKenzie et al., 2007; Bao et al., 2016; Wu and Zhang, 2010). In this research, geostatistical software library (GSLIB) (Deutsch and Journel, 1997) is deployed for generating an unconditional spatially correlated realization of soil in a 2-D domain. GSLIB is an open source computer program written in FORTRAN. One can use this program to quantify spatial variability of existing fields using Geostatistics or generate random fields with specified Geostatistical properties. The lack of spatial information describing peat thermal properties has led the author to assume reasonable values based on related studies.

A key assumption here is that of similar spatial variability structure and scale for thermal and hydraulic properties. Usowicz et al. (1996) showed that soil water content and bulk density have the most influence on the spatial variability of thermal properties of agricultural soil. Since fully saturated soil is assumed throughout the thesis, the empirical functions from Lawrence et al. (2018) and Liu and Lennartz (2018) are chosen that express thermal and hydraulic conductivity based on bulk density (Equations 2.23 and 2.24). In the present work, similar to research by Simms et al. (2014) about the effect of soil heterogeneity on horizontal ground loop heat exchangers, the horizontal correlation length was selected to be 12 m and an aspect ration of 6 was selected for the horizontal vs. vertical anisotropy (Usowicz et al., 1996). The nugget effect for this research is assumed to be 0 because the properties are upscaled to the 2-D elemental scale of the finite element mesh for the sake of numerical stability; thus, spatial variability for small scales is not likely to be influential. A range of 10 to 760 kg.m^{-3} (Liu and Lennartz, 2018) is assumed for the variability of

peat bulk density based on the meta study conducted by Liu and Lennartz (2018) on the gradient of bulk density of various types peat soil. An exponential function (Equation 2.21) is assumed for the theoretical variogram. Summary of the geostatistical model parameters and values are listed in Table 2.1.

2.4.2 Heterogeneous soil realization using GSLIB

As mentioned in Section 2.4.1, a sequential Gaussian realization is generated (Figure 2.6a) to simulate an unconditional and spatially correlated field, and the semivariograms of the generated field (experimental semivariograms) are compared to the theoretical semivariograms. The parameters in Table 2.1 are used in the sequential Gaussian simulations. To evaluate how well the simulated realization performs vs. the theoretical variogram of the same field, the experimental variogram of the simulated field is plotted against the theoretical one. As is evident in Figure 2.6b, the semivariogram calculated for the simulated field generally matches the theoretical semivariogram generated based on the same geostatistical parameters.

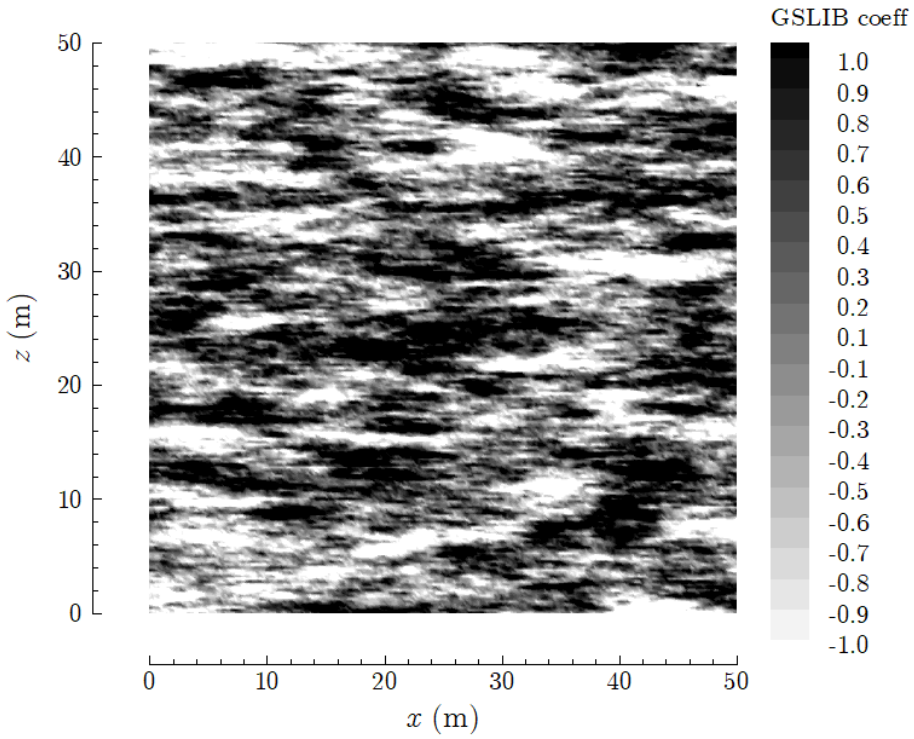

(a)

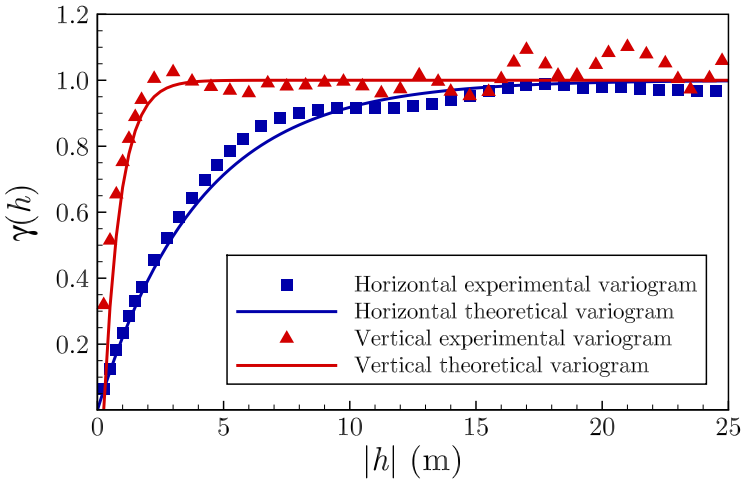

(b)

Figure 2.6 GSLIB simulation: (a) a realization generated by a sequential Gaussian simulation using GSLIB (b) experimental variogram vs. theoretical variogram

Chapter 3

A theoretical extension of the soil freezing curve paradigm

Statement of contribution

The following chapter is written based on the following article:

Amiri, E. A., Craig, J. R., and Kurylyk, B. L. (2018). A theoretical extension of the soil freezing curve paradigm. *Advances in Water Resources*, 111(November 2017), 319–328.

The paper was co-authored by myself and my supervisor, Dr. James R. Craig, and Dr. Barret L. Kurylyk, Assistant Professor in the Department of Civil and Resource Engineering and Centre for Water Resources Studies at Dalhouse University. This paper presents a theoretical extension for the form of soil freezing curve (SFC) based on local spatial heterogeneity in soil. In this paper, I developed the 1-D extended finite element method (XFEM) formulation for simulating nonlinear heat transfer with phase-change in soil. I implemented the model in a code written in Matlab for simulating different realizations of a heterogeneous soil column. I also prepared the manuscript. Dr. Craig provided the key idea of investigating the effect of local heterogeneity in soil on the shape of SFC. Moreover, he provided guidance through supervising the mathematical formulations and editing the manuscript. Dr. Kurylyk provided collaborative suggestions and guidance through editing the manuscript.

3.1 Introduction

Ground ice influences the mechanical, hydraulic, and thermal properties of soil (Qi et al., 2006; Tang and Yan, 2014; Jamshidi et al., 2015), and thus permafrost thaw can cause soil instability (Oztas and Fayetorbay, 2003; Kemper and Rosenau, 1986) and hydrologic and hydrogeologic changes (Wang et al., 2009). Thawing permafrost also acts as a positive climate change feedback by releasing sequestered carbon into the atmosphere (Kurganova et al., 2007). Consequently, quantifying the influence of recent and future global warming on permafrost thaw is an important research topic for climate scientists, hydrologists, and geotechnical engineers (Walvoord and Kurylyk, 2016; Schuur et al., 2015; Hinzman et al., 2005).

Numerical models are often employed to calculate rates of permafrost thaw because analytical solutions to heat transfer problems involving phase change are limited by their simplifying assumptions (Kurylyk et al., 2014). In numerical models, the front tracking approach (Skrzypczak et al., 2012) precisely predicts the location of the phase change interface, and thus it is popular in solidification problems, in which the exact location of the interface between the solid and liquid phase is important. The issue with this method is that it may be impossible to track multiple sharp interfaces of complex shape; alternately, in most porous media, the phase change interface is not sharp. The latter is generally the case for soil freezing and thawing, because pore water phase change is a non-isothermal process due to capillary and sorptive forces, variable solute concentrations, and soil heterogeneities (Painter et al., 2016). Thus, the freeze-thaw interface in soil exists as a partially frozen 'slushy zone'. In this case, a continuum enthalpy approach is typically implemented to represent the phase change interface (Dall'Amico et al., 2011) in which the transition between the fully frozen and fully thawed zones is simulated by considering a temperature-ice saturation (or alternatively a temperature-liquid water saturation) relation called the SFC (Koopmans and Miller, 1966). Here, the Stefan condition, which states that the discontinuity in heat flux at the interface is equivalent to the rate of latent heat released or absorbed (Lunardini, 1981), is implicitly satisfied. Also, the sharp interface, which is a source of singularity in the numerical solution, is smoothed out and does not require any special accommodation. This continuum approach is the one most commonly employed in numerical models of freeze-thaw in porous media (e.g., Voller et al., 1987; Swaminathan and Voller, 1992; Alexiades and Solomon, 1993; Nedjar, 2002), in part because it is the most numerically stable.

SFCs are either derived theoretically based on the analogy between soil water charac-

teristic curves (SWCCs) and SFCs (Koopmans and Miller, 1966) or empirically developed from field or laboratory data using a simple mathematical expression such as a power or exponential function (Kurylyk and Watanabe, 2013). The analog between SFCs and SWCCs is predicated on an understanding that pore water is held by capillary and/or sorptive forces during both soil freezing and soil drying, and this tightly held water retards drying or freezing processes. The primary variable in SWCC-derived SFCs is pressure. The Clausius-Clapeyron equation is used to express the equilibrium relationship between the pressure of ice and water and soil temperature. The generalized form of the Clausius-Clapeyron equation in terms of water and ice pressure can be written as (Ma et al., 2015)

$$\frac{1}{\rho_{\mathrm{w}}} dP_{\mathrm{w}} - \frac{1}{\rho_{\mathrm{i}}} dP_{\mathrm{i}} = \frac{L_{\mathrm{f}}}{T} dT \tag{3.1}$$

in which $P\,(\mathrm{N.m^{-2}})$ is pressure, T is the temperature at the freezing front in Kelvin (K), and L_{f} $(\mathrm{J.kg^{-1}})$ is the latent heat of fusion of pure water, $\rho\,(\mathrm{kg.m^{-3}})$ is density, and subscripts w and i denote the water and ice phase respectively. This equation is an approximation that is only valid at the freezing front when the temperature is close to the melting temperature of water. Equation 3.1, which represents an equilibrium relation between pressure and temperature, has several variations in the literature as reviewed by Kurylyk and Watanabe (2013). This equation can be inserted into an existing SWCC to indirectly develop an expression between pressure (or temperature) and the liquid saturation (Hansson et al., 2004). The focus of the present study is independently derived SFCs for which the primary variable is temperature. The main drawback of the independently-derived SFCs is that they lack a rigorous theoretical justification for their range. Parameters for these SFCs can be obtained based on fitting experimental curves, but there is uncertainty if the curves are transferable when pressures, water contents, or other conditions change. Often, a differentiable continuous function is used with the slushy zone ranging from about 1 to 4 °C (e.g., McKenzie et al., 2007).

The purpose of this study is to develop a theoretical understanding of how mechanisms other than sorptive or capillary processes may contribute to the temperature range over which water freezes in soils. In particular, this study examines how spatial variability in the freezing point temperature and the soil properties may widen the SFC interval. The aqueous heterogeneity (i.e., spatial variation in the freezing point temperature) is related to solute concentration and water matric potential (Flerchinger et al., 2006; Bao et al., 2016), and the soil heterogeneity is ascribed to natural spatial variation in thermal conductivity at scales finer than a representative elementary volume (REV).

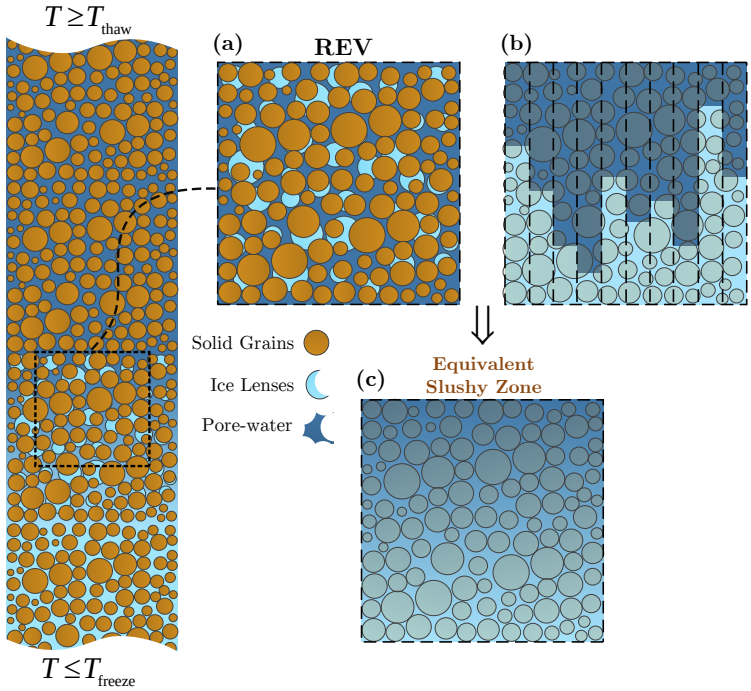

Figure 3.1 Frozen soil slushy zone and equivalent heterogeneous layers: (a) Physical distribution of ice and water in soil matrix, (b) Conceptualization as parallel ice-water transitions, (c) Equivalent slushy zone. T_{thaw} and T_{freeze} are the temperatures at which soil thaws and freezes.

3.2 Slushy zone characterization

The existence of a slushy zone in soil is generally understood to be caused by capillary and sorptive forces, which impede the complete freezing of pore water. This is physically analogous to the suction range over which soil dries (Koopmans and Miller, 1966). While we acknowledge that these processes are very important in creating a temperature range over which soil freezes and thaws, we herein demonstrate that the extent of the slushy zone can also be partly ascribed to variations in both water purity and soil properties, which impact the freezing point of water. It is noteworthy that the observed freezing temperature range is mainly below and slightly above 0 °C, the freezing point for pure water (Williams and Smith, 1989). While this gradual transition from pure ice to liquid water has been observed in the field and laboratory experiments (e.g., Williams, 1964; Koopmans and Miller, 1966; Spaans and Baker, 1996; Quinton et al., 2005; Zhou et al., 2014) and repeatedly used for continuum modeling of freeze-thaw processes in porous media (e.g., Lunardini, 1985; Flerchinger et al., 2006; McKenzie et al., 2007; Bense et al., 2009), few attempts have been made to determine the theoretical factors which determine the extent and shape of the temperature-ice fraction relation beyond the similarities between soil wetting/drying and

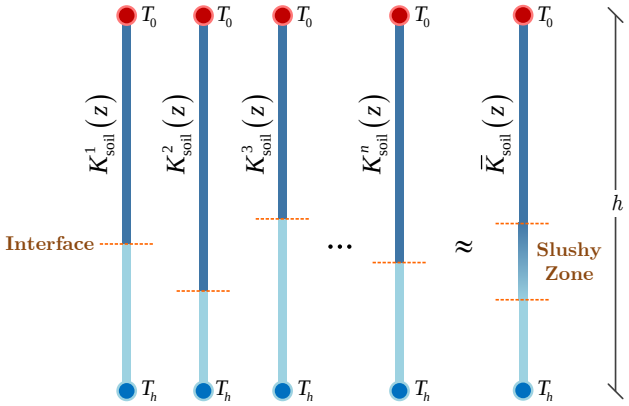

Figure 3.2 Realizations analyzed by the extended finite element model, and the equivalent slushy zone.

soil freezing/thawing processes.

This research presents a novel procedure to investigate the temperature-ice fraction relationship, in which an REV of the slushy zone is considered as an average of several stochastically generated heterogeneous soil columns. Each column may consist of several layers of soil with different properties, which are randomly distributed in space (Figures 3.1 and 3.2). These heterogeneities in the properties of the system can be represented by a distribution (Figure 3.2), and this distribution causes a distribution in the freeze-thaw interface (Figure 3.1b), which can in turn be represented as a gradually transitioning slushy zone (Figure 3.1c). While treated as parallel 1-D systems, the conceptual model could also describe independent intertwining pathways through the porous medium through which freezing or thawing progresses. Each soil-water-ice system might have various degrees of heterogeneity, and the characteristic heterogeneity of the system leads to a different SFC. For instance, chemical heterogeneity of the pore liquid (ionic content) leads to a depression in the soil freezing point; heterogeneity in the physical properties of soil affects both the hydraulic conductivity (important for advective heat transfer) and the average thermal properties. The focus of this research is to assess the effects of heterogeneous thermal properties and liquid characteristics, particularly soil thermal conductivity and freezing point, on SFCs.

The stochastically generated 1-D freeze-thaw progression models are simulated using the XFEM (Khoei, 2015), as described in more detail later. In this approach, the interface is driven by applying the Stefan condition. Each realization generates a different location of the ice/water interface, leading to a spatial distribution of local temperature and ice saturation within the 1-D column, as seen in Figure 3.3. Depending on the soil type,

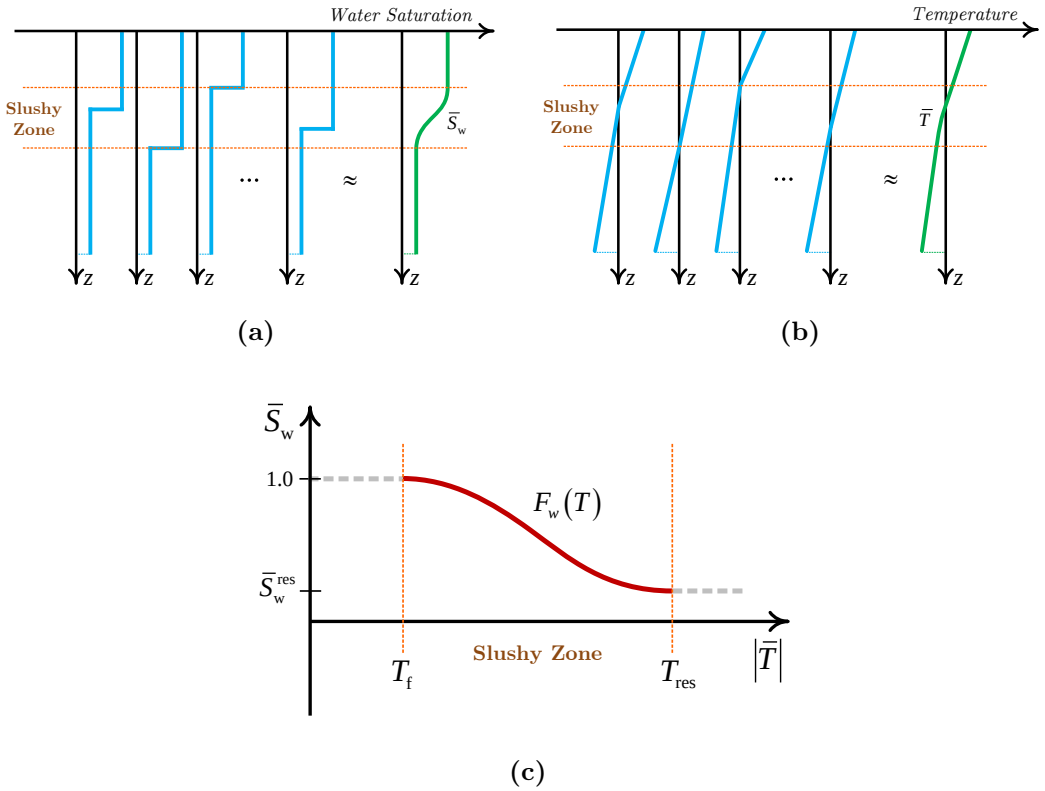

Figure 3.3 SFC as generated from multiple realizations of sharp interface problem: (a) Water saturation profile and mean water saturation profile for multiple realizations, (b) Temperature profile and mean water saturation profile for multiple realization, (c) Resultant SFC.

there may be residual water saturation (S_w^{res}) at temperatures below the freezing point due to water being tightly held (Cannell and Gardner, 1959; Miller, 1990; Spaans and Baker, 1996; Watanabe and Mizoguchi, 2002). The slushy zone in fully saturated soil would consist of two extreme fronts, i.e., the ice front (where the ice saturation, S_i, is equal to $1 - S_w^{res}$, where S_w^{res} is the residual liquid water content) and the liquid water front (where the liquid water saturation, S_w, is equal to 1). These two fronts are separated by the slushy zone. The spatial extent of this transition zone is herein ignored. Rather, the average temperature across all realizations is mapped to the average ice saturation across all realizations, generating a corresponding SFC (Figure 3.3c). Thus a distribution of sharp interfaces is employed to arrive at a slushy zone or distributed SFC. In this study, the soil is fully saturated.

3.2.1 The 1-D model

The equations used in the one dimensional realizations are similar to the governing equations of the classic Stefan Problem, which has been applied both analytically and numerically and appears in several works (Lunardini, 1981; Chessa et al., 2002; Bernauer and Herzog, 2012). Thus, each of the one dimensional realizations is a two-phase Stefan Problem but is further characterized by varying properties along the problem domain, Ω.

Although heat transfer in saturated soil can occur via conduction and advection, in the current model, only heat transfer via conduction is considered. Hence, the energy conservation equation over Ω applies

$$\frac{\partial}{\partial t}\left(\overline{\rho c}T\right) = -\nabla\cdot\mathbf{q} \tag{3.2}$$

$$\mathbf{q} = -\bar{k}\nabla T \tag{3.3}$$

in which $\mathbf{q}$ is the conductive heat flux density vector ($\mathrm{kg.m^{-2}}$) and $\overline{\rho c}$ and $\bar{k}$ are the bulk volumetric heat capacity and bulk isotropic thermal conductivity of the soil-water-ice media, respectively. These are calculated as the volumetrically weighted arithmetic mean of the soil constituent thermal properties:

$$\overline{\rho c} = n(S_{\mathrm{w}}\rho_{\mathrm{w}}c_{\mathrm{w}} + S_{\mathrm{i}}\rho_{\mathrm{i}}c_{\mathrm{i}}) + (1-n)\rho_{\mathrm{s}}c_{\mathrm{s}} \tag{3.4}$$

$$\bar{k} = n(S_{\mathrm{w}}k_{\mathrm{w}} + S_{\mathrm{i}}k_{\mathrm{i}}) + (1-n)k_{\mathrm{s}} \tag{3.5}$$

where, n, S, ρ, c, and k are the porosity, saturation, density, specific heat, and thermal conductivity, respectively. The 'w', 'i', and 's' subscripts denote the parameters of water, ice, and soil particles. The boundary and initial conditions for this problem are

$$T = \tilde{T}\left(z,t\right) \qquad \text{on } \Gamma_{\mathrm{D}} \tag{3.6}$$

$$T\left(z,0\right) = T_{\mathrm{ini}} \tag{3.7}$$

where $\tilde{T}\left(z,t\right)$ is the temperature over the Dirichlet (Γ_{D}) boundaries. In addition, another condition must be satisfied at the interface between fully frozen and fully thawed media,

in which the temperature should be equal to the freezing point of water (T_{f}).

$$T_{\mathrm{int}} = T_{\mathrm{f}} \qquad \text{on } \Gamma_{\mathrm{int}} \tag{3.8}$$

where T_{int}, T_{f}, and Γ_{int} are the interface temperature, soil freezing temperature, and interface boundary, respectively. Equation 3.8 indicates that the temperature field is continuous. However, its gradient is discontinuous due to the latent heat released/absorbed during porewater phase change and the different soil thermal properties below and above the interface caused by the dissimilar thermal properties of pore ice and pore water.

As previously noted, the location of interface is tracked explicitly in this study. Hence, an energy balance equation is required to allocate the interface position and control its rate of migration. This equation is called the Stefan condition, which is applied on Γ_{int}, and stipulates that the conductive heat flow discontinuity across the interface is equal to the released or consumed latent energy with progression of that interface, i.e.,

$$\left(k^{+}\nabla T^{+} - k^{-}\nabla T^{-}\right) = -n\rho_{\mathrm{w}}L_{\mathrm{f}}v \tag{3.9}$$

where ρ_{w} is the water density (kg.m^{-3}), L_{f} is the latent heat of fusion of water (334,000 J.kg^{-1}), v is the speed of the interface progression (m.s^{-1}), and + and - indicate positions immediately below and above the interface. The interface calculations follow the "level set method" presented in Salvatori and Tosi (2009).

XFEM formulation

Due to the continuity of the base (shape) functions used in the classic finite element method (FEM), FEM is incapable of handling discontinuity of any kind within an element. The sharp interface of ice/water in soil imposes weak discontinuity in the temperature field resulting in discontinuity in its gradient field. XFEM is an enhancement to the classic FEM to overcome its inability to capture discontinuities (Khoei, 2015). This is accomplished by adding an enhanced field to the standard interpolation field; this process is called enrichment. According to the nature of the Stefan Problem, the enriched field should be continuous over Ω. However, the gradient of this field needs to be discontinuous. The XFEM approximation of the temperature field can be written as

$$T\left(z,\,t\right) = \sum_{I\in\mathcal{N}} N^{I}_{\mathrm{std}}\left(z\right)\bar{T}^{I}_{\mathrm{std}}\left(t\right) + \sum_{J\in\mathcal{M}} \underbrace{N^{I}_{\mathrm{enr}}\left(\left|\varphi\left(z\right)\right| - \left|\varphi\left(z^{J}\right)\right|\right)}_{enriched\,shape\,function}\bar{T}^{J}_{\mathrm{enr}}\left(t\right) \tag{3.10}$$

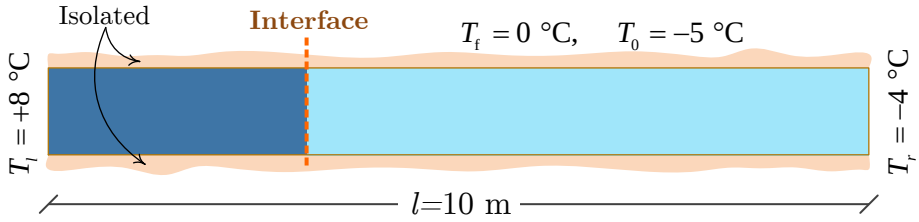

Figure 3.4 Verification problem geometry and boundary conditions

where N denotes the shape functions vector, $\bar{T}$ is the nodal temperature vector, $\mathcal{N}$ and $\mathcal{M}$ are respectively the standard and enrichment sets, the 'std' subscript denotes an association with standard degrees of freedom, 'enr' subscript denotes values associated with the enriched degrees of freedom. The Signed Distance Function (Chessa et al., 2002) is used as the enrichment function, $\varphi(z)$, which exhibits a discontinuity in the temperature gradient field and is expressed as

$$\varphi(z) = |z - \tilde{z}|\text{sign}(z - \tilde{z}) \tag{3.11}$$

in which $\tilde{z}$ is the interface location. The weak form and fully discretized equations are presented in Appendix A.1.1. This solution approach closely follows Merle and Dolbow (2002). The accuracy of the XFEM for a homogeneous case was determined in this study via comparison with results reported by (Merle and Dolbow, 2002) and verified against the exact solution of the classic Stefan Problem (Solomon, 1966).

Verification of XFEM against the exact analytical solution of the Stefan Problem

In this example, a 10m one-dimensional domain under thawing condition is considered. The conditions (boundary and initial) and geometry of the problem are shown in Figure 3.4. The Neumann solution predicts the exact position of the interface and the analytical temperature distribution along the domain as below:

$$X_{\text{interface}}(t) = 2\lambda\sqrt{\alpha_{\text{th}}t} \tag{3.12}$$

$$T_{\text{th}}(x,t) = T_l - (T_l - T_{\text{f}})\frac{\text{erf}\left(\frac{x}{2\sqrt{\alpha_{\text{th}}t}}\right)}{\text{erf}(\lambda)}, \qquad x < x_{\text{interface}} \tag{3.13}$$

$$T_{\text{fr}}(x,t) = T_r + (T_{\text{f}} - T_r)\frac{\text{erf}\left(\frac{x}{2\sqrt{\alpha_{\text{fr}}t}}\right)}{\text{erf}(\lambda\nu)}, \qquad x > x_{\text{interface}} \tag{3.14}$$

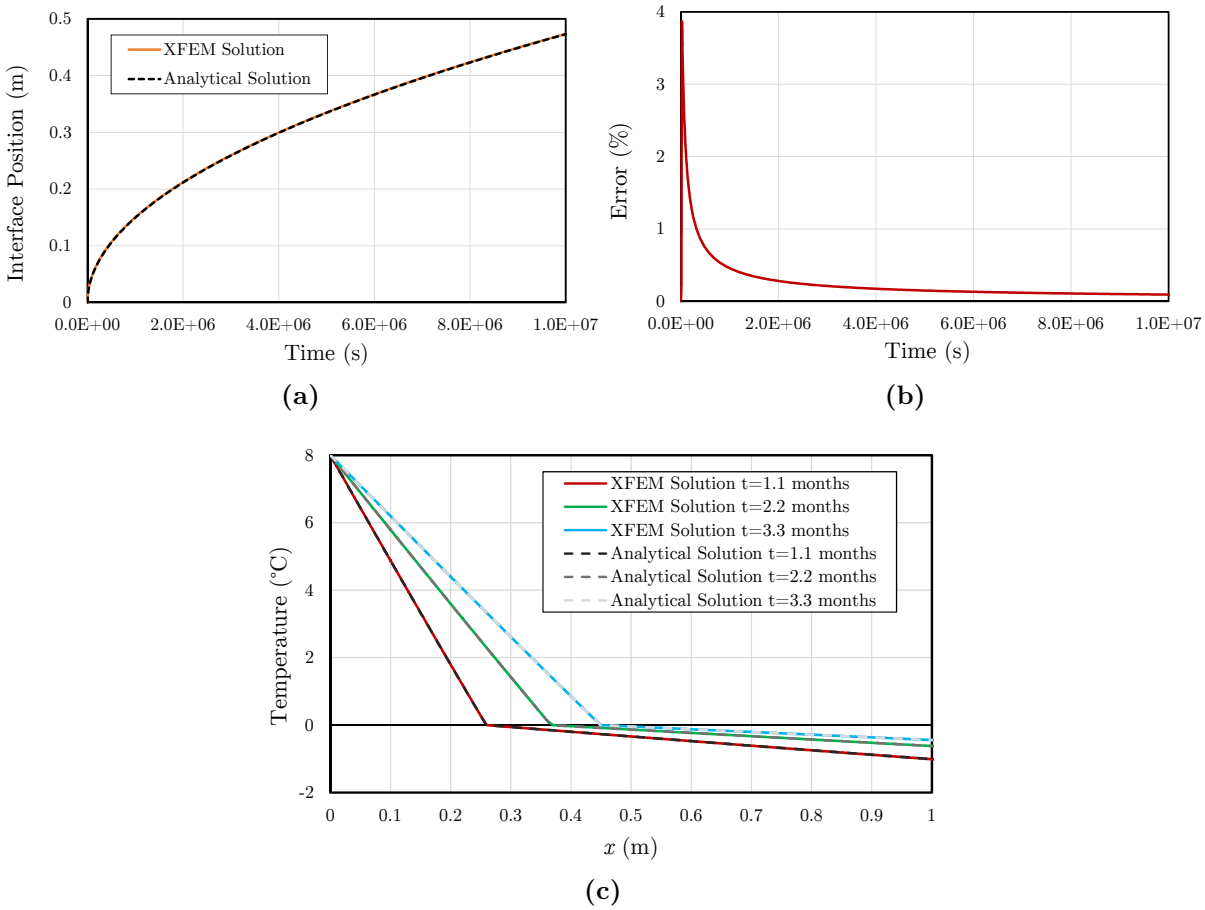

Figure 3.5 Verification problem: (a) Evolution of interface vs. time , (b) Error of interface location estimation, (c) Temperature profile along the domain at different time steps

where $\alpha_{\text{th}} = K_{\text{th}}/(\rho c)_{th}$ is the Stefan number for the fully thawed part, $\alpha_{\text{fr}} = K_{\text{fr}}/(\rho c)_{\text{fr}}$ is the Stefan number for the fully frozen part, and λ is calculated by solving the following nonlinear equation.

$$\lambda\sqrt{\pi} + \frac{c_{\text{fr}}\left(T_{\text{f}} - T_r\right)}{\nu L \exp\left(\lambda^2\nu^2\right)\operatorname{erfc}(\lambda\nu)} + \frac{c_{\text{th}}\left(T_{\text{f}} - T_{\text{l}}\right)}{L\exp\left(\lambda^2\right)\operatorname{erf}(\lambda)} = 0 \tag{3.15}$$

The XFEM solution for the Stefan problem, which is fully described in Appendix A.1, is compared with the exact analytical solution. As is evident in Figure 3.5, the numerical and analytical solutions show a perfect match.

The soil freezing function is here generated via averaging of multiple realizations of one-dimensional freezing front propagation in both homogeneous and heterogenous media. Care was taken to avoid artefacts in the resultant soil freezing function that could be

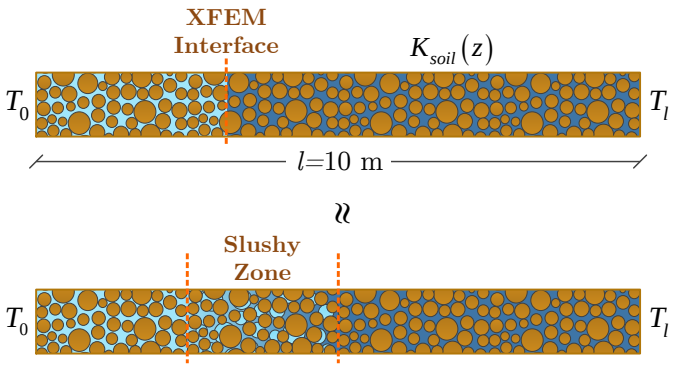

Figure 3.6 Sketch of a heterogeneous soil layer realization thawed at right and frozen on left (T_0 and T_l are the temperatures at the freezing and thawing boundaries, respectively).

caused by boundary condition effects, numerical discretization errors, domain size issues, insufficient number of realizations, i.e., the resultant model cannot be dependent upon the geometric configuration or numerical parameters of the model.

3.2.2 Soil freezing curves

The SFC is herein generated via averaging of the multiple realizations of 1-D freezing front propagation in both homogeneous and heterogeneous media. Care was taken to avoid artifacts in the resultant SFC that could be caused by boundary condition effects, numerical discretization errors, domain size issues, and insufficient number of realizations; i.e., the resultant model cannot be dependent upon the geometric configuration or numerical parameters of the model.

In order to investigate the effects of soil heterogeneity on the SFC, the freezing zone is assumed to consist of several heterogeneous soil columns, and each heterogeneous column is represented by a realization which will be analyzed by the XFEM, Figures 3.1 and 3.2. It is noteworthy that these realizations are assumed to be representatives of realistic soils. After extracting the water saturation and temperature graphs from each realization and averaging them along every fixed z cross section (Figures 3.3a and 3.3b) the SFC can be derived (Figure 3.3c).

Table 3.1 Constant properties used in simulations

Parameters	Values	Parameters	Values
c_{s} $\left[\mathrm{J.kg^{-1}.K^{-1}}\right]$	900	K_{i} $\left[\mathrm{W.m^{-1}.K^{-1}}\right]$	2.14
ρ_{s} $\left[\mathrm{kg.m^{-3}}\right]$	2650	c_{i} $\left[\mathrm{J.kg^{-1}.K^{-1}}\right]$	2108
n (porosity)	0.35	ρ_{i} $\left[\mathrm{kg.m^{-3}}\right]$	920
$S_{\mathrm{w}}^{\mathrm{res}}$	0.12	L_{heat} $\left[\mathrm{J.kg^{-1}}\right]$	334000
K_{w} $\left[\mathrm{W.m^{-1}.K^{-1}}\right]$	0.58	Δt [s]	5×10^{5}
c_{w} $\left[\mathrm{J.kg^{-1}.K^{-1}}\right]$	4187	$n_{\mathrm{realization}}$ [1]	600
ρ_{w} $\left[\mathrm{kg.m^{-3}}\right]$	1000	n_{layer} [2]	300

[1] number of realizations

[2] number or soil layers is each realization

3.3 Numerical simulation and results

In this paper, two forms of heterogeneity are investigated independently: (1) soil thermal conductivity, and (2) soil freezing point depression. First, we examine the impacts of boundary conditions and explore the sensitivity of the SFC to the extrinsic parameters of the soil-water-ice system of interest. We then aggregate and non-dimensionalize model results to infer a general SFC that is a function of the standard deviation of media thermal conductivity only. Lastly, we determine a SFC for the case where the media is homogeneous but the freezing point is treated as a random variable, due to local variability of dissolved solute concentrations.

The domain of interest (Figure 3.6) which is consistent in all the simulations included in this research, is a 10 m 1-D heterogeneous soil column discretized into 300 homogeneous elements. In the case of the soil being physically heterogeneous, the thermal conductivity

Table 3.2 Varying properties used in simulations

Parameters	Boundary Condition Sensitivity Analysis	Thermal Conductivity Heterogeneity		Freezing Point Heterogeneity		Hysteresis Analysis	
		Case 1	Case 2	Case 1	Case 2	Case 1	Case 2
$m_{K_{\mathrm{s}}}$ $\left[\mathrm{W.m^{-1}.K^{-1}}\right]$	2.92	1.32∼4.52	2.92	2.92	2.92	2.92	2.92
$SD_{K_{\mathrm{s}}}$ $\left[\mathrm{W.m^{-1}.K^{-1}}\right]$	0.2	0.2	0.3∼1.7	0	0	0.2	0
$m_{T_{\mathrm{f}}}$ [°C]	−0.25	−0.25	−0.25	−0.42∼0	−0.25	−0.25	−0.25
$SD_{T_{\mathrm{f}}}$ [°C]	0	0	0	0.095	0.035∼0.14	0	0.095

of the elements is log-normally distributed with mean, μ, and standard deviation, σ; these are related to the untransformed mean, m and untransformed variance v, by the following functions

$$\mu = \log\left(\frac{m^2}{\sqrt{v+m^2}}\right) \tag{3.16}$$

$$\sigma = \sqrt{\log\left(\frac{v}{m^2}+1\right)} \tag{3.17}$$

The variability of the soil freezing point is represented using a log-normal distribution. The material properties and statistical parameters used in the simulations are given in Tables 3.1 and 3.2. The soil statistical parameters and thermal properties incorporated in the simulations represent soil with a clay mineral constituent, reported by Williams and Smith (1989) and can also be found in Bonan (2008). A sensitivity analysis was run to choose an appropriate number of realizations such that the minimum difference between the standard deviation of the Gaussion fitting function and the standard deviation of the raw outputted data was achieved.

The representative average model-generated SFCs are here fit with a Gaussian fitting function, which is defined as

$$\bar{S}_{\mathrm{w}}\left(\bar{T}\right) = \left(1 - S_{\mathrm{w}}^{\mathrm{res}}\right) e^{-\left(\frac{\bar{T}-\alpha}{\beta}\right)^2} + S_{\mathrm{w}}^{\mathrm{res}} \tag{3.18}$$

In which $\bar{S}_{\mathrm{w}}$ is the average water saturation, S_{res} is the residual water saturation, $\bar{T}$ is the average temperature, and α and β are the fitting parameters calculated from a least-squares fitting procedure. Note that $\bar{S}_{\mathrm{w}}$ and $\bar{T}$ indicate average or representative S_{w} and T in an REV and therefore translates to S_{w} and T in the conventional SFC ($S_{\mathrm{w}} = F(T)$). This functional form has been used in the past but without justification of the choice for α and β (e.g., McKenzie et al., 2007). Since the Gaussian function is continuous and differentiable, it can be readily implemented in continuum modeling of soil freeze-thaw processes as most model formulations require a continuous and differentiable function for the soil freezing curve (e.g., McKenzie et al., 2007). How such a function can be implemented in conjunction with a sorptive- or capillary-based soil freezing curve is a question that will be investigated in future work.

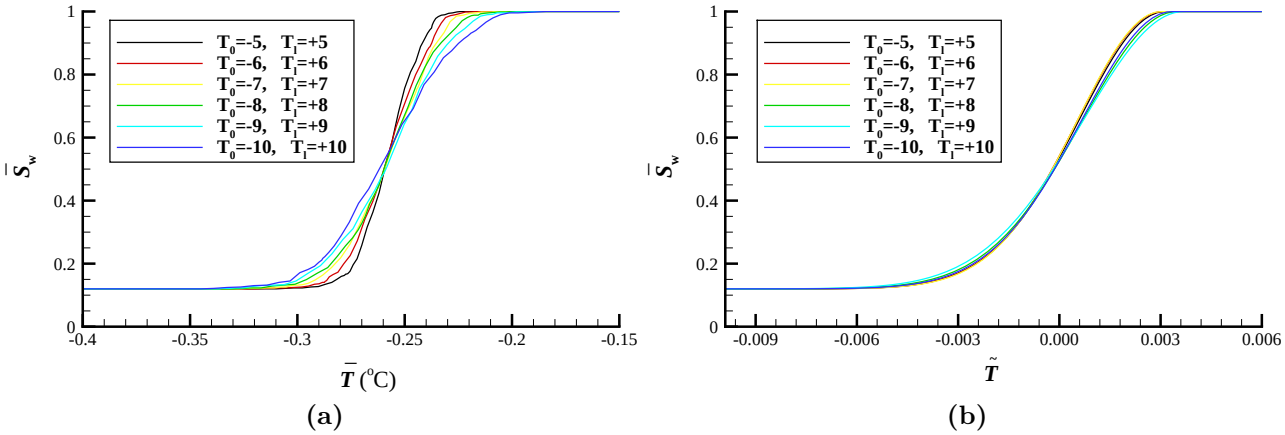

Figure 3.7 Effect of boundary conditions on the SFC considering soil thermal conductivity as the sources of heterogeneity: (a) model-generated SFCs, (b) Normalized Gaussian fitted SFCs. The horizontal axis in (a) represents the average temperature, while the horizontal axis in (b) represents the scaled temperature (see Equation 15).

3.3.1 Sensitivity analysis: effect of boundary conditions on the SFC

A set of sensitivity analyses was carried out to investigate the effect of boundary conditions, geometry, and solution time. The effect of boundary conditions on the SFC is described in this section, with the desirable outcome that the impacts of 1-D model boundary conditions is negligible. In this analysis, twelve cases of Dirichlet boundary conditions are considered. The thermal conductivity and freezing point depression are both considered as sources of heterogeneity. As is evident in Figure 3.7a, the SFC is mildly impacted by boundary conditions. However, by giving careful consideration to the trend followed by each case, it can be interpreted as a sensitivity to the system temperature gradient (temperature difference of the cold and warm boundaries). Hence, the following normalization of the average temperature results in a narrow variation of SFC, (Figure 3.7b).

$$\tilde{T} = \frac{\left(\bar{T} - T_{\mathrm{f}}\right)}{\mathrm{abs}\left(T_0 - T_{\mathrm{ini}}\right)} \tag{3.19}$$

in which $\tilde{T}$ is the scaled temperature , $\bar{T}$ is the average temperature, and T_0 and T_{ini} are the temperatures at the freezing boundary and the initial temperature of the soil domain, respectively.

However, Figure 3.8 clearly illustrates that boundary conditions do not have a significant influence on the SFC if the source of heterogeneity is the soil freezing point depression

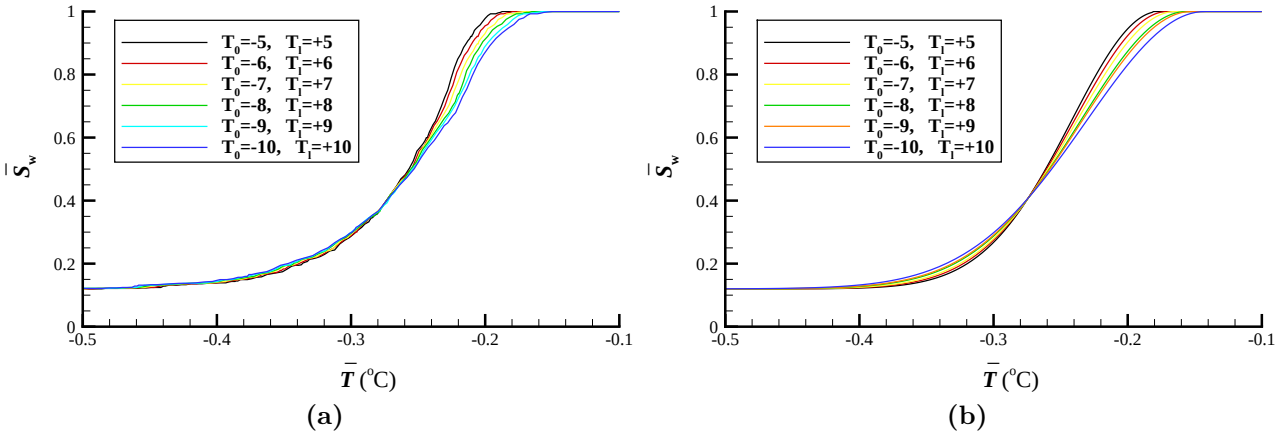

Figure 3.8 Effect of boundary conditions on the SFC considering freezing point as the source of heterogeneity: (a) Model-generated SFCs, (b) Gaussian fitted SFCs

(recall here that the primary concern is describing the temperature range of the slushy transition, not the precise shape of the curve). It is noteworthy that the SFCs are not sensitive to the length of the solution time or medium if the medium is sufficiently large that the problem is effectively semi-infinite.

3.3.2 Heterogeneity of the soil thermal conductivity field

The soil thermal conductivity is considered as the only heterogeneous parameter of the soil thermal properties. Two cases are studied, with each case consisting of twelve sets of realizations (Table 2). In the first case, the thermal conductivity mean is varied between $1.32 \sim 4.52\,\mathrm{W.m^{-1}.K^{-1}}$, and the standard deviation is held constant ($0.2\,\mathrm{W.m^{-1}.K^{-1}}$); however, in the second case, the standard deviation is varied between $0.3 \sim 1.7\,\mathrm{W.m^{-1}.K^{-1}}$, and the thermal conductivity mean is held constant ($2.92\,\mathrm{W.m^{-1}.K^{-1}}$). These values were loosely based on the range of thermal properties depending on the porosity and type of soil grains (e.g., Bonan, 2008). As is evident in Figure 3.9 and Figure 3.10, both the thermal conductivity mean and standard deviation influence the SFC. By scaling the temperature using the following equation,

$$T^* = \left(\bar{T} - T_\mathrm{f}\right) \sqrt{\frac{m_{K_\mathrm{s}}}{SD_{K_\mathrm{s}}}} \tag{3.20}$$

the SFCs collapse into a single characteristic curve. Additionally, Figures 3.9b and 3.10b, which depict the relationship between the normalized temperature and the water saturation, indicate that the SFCs for a realistic range of the statistical parameters of permafrost

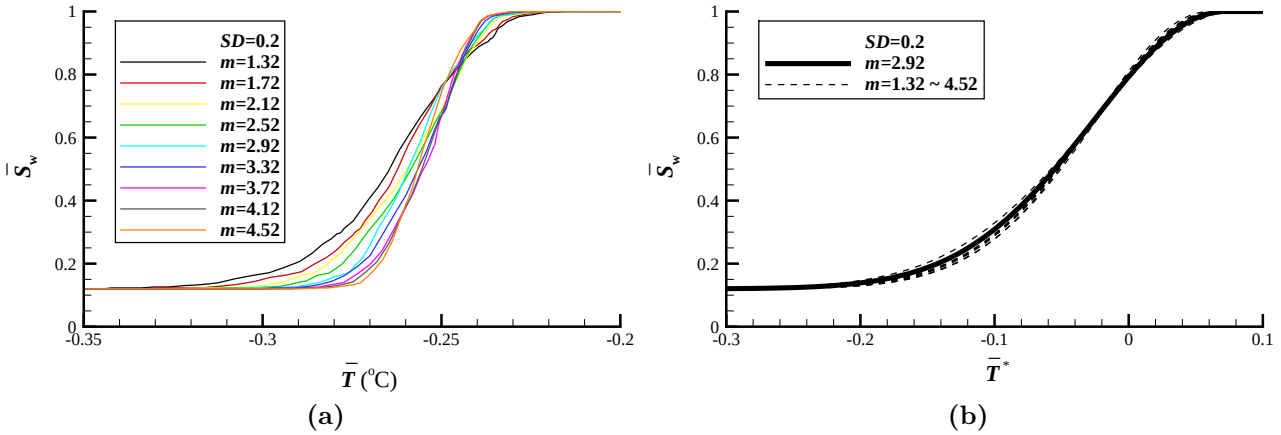

Figure 3.9 Effect of soil thermal conductivity mean on the SFC: (a) SFC, (b) Normalized Gaussian fitted SFCs

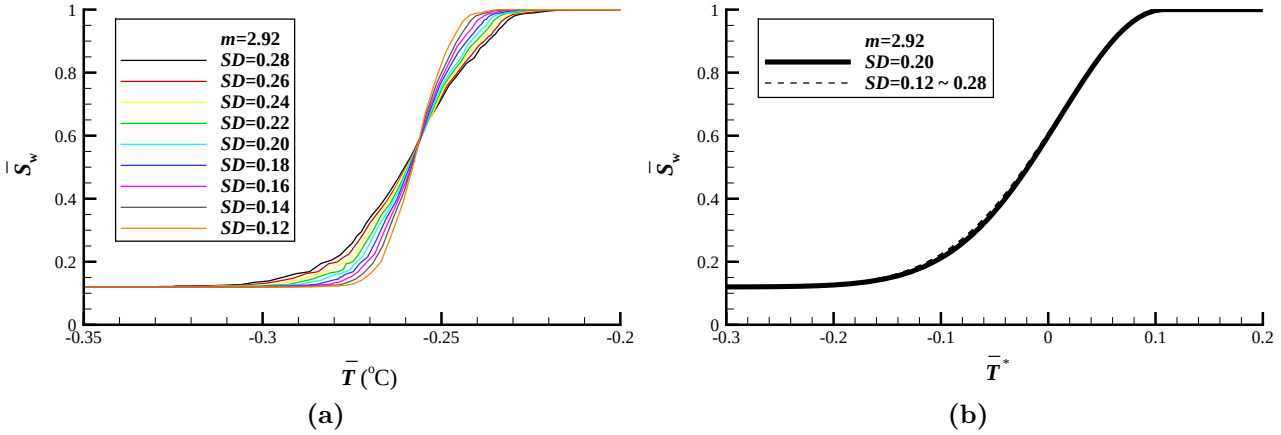

Figure 3.10 Effect of soil thermal conductivity standard deviation on the SFC: (a) model-generated SFCs, (b) Normalized Gaussian fitted SFCs.

thermal conductivity are similar.

3.3.3 Heterogeneity of the soil freezing point depression

Like in the previous section, both the mean and standard deviation of the water freezing point are parameters of interest. In the first case, the water freezing point depression mean is varied between -0.42 to $0\,^{\circ}$C (Banin and Anderson, 1974). and the standard deviation is held constant ($0.095\,^{\circ}$C). In the second case, the standard deviation of the freezing point depression is varied between $0.035 \sim 0.140\,^{\circ}$C and the mean is held constant ($-0.25\,^{\circ}$C). As expected, the freezing point depression heterogeneity plays an important

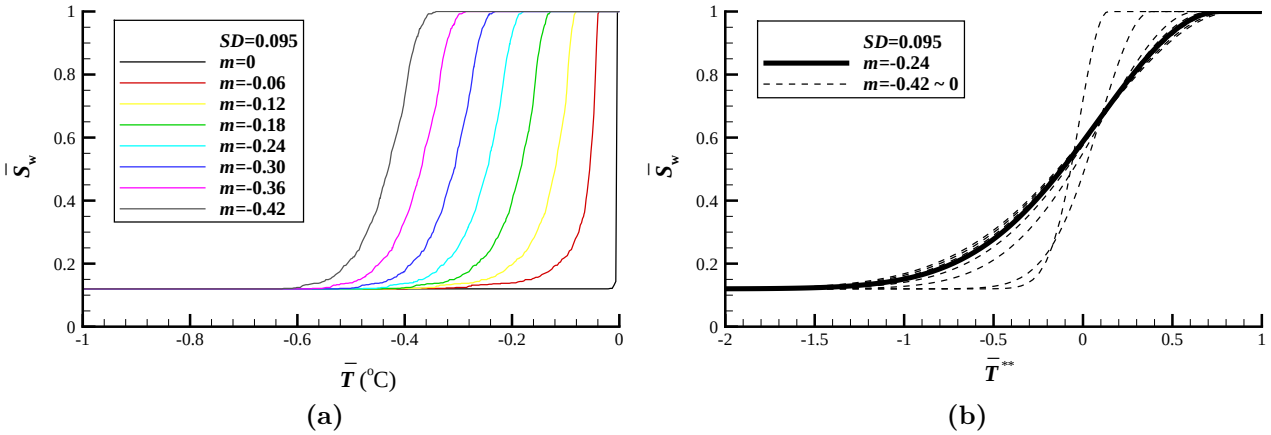

Figure 3.11 Effect of soil freezing point mean on its freezing function: (a) model-generated SFCs, (b) Normalized Gaussian fitted freezing functions.

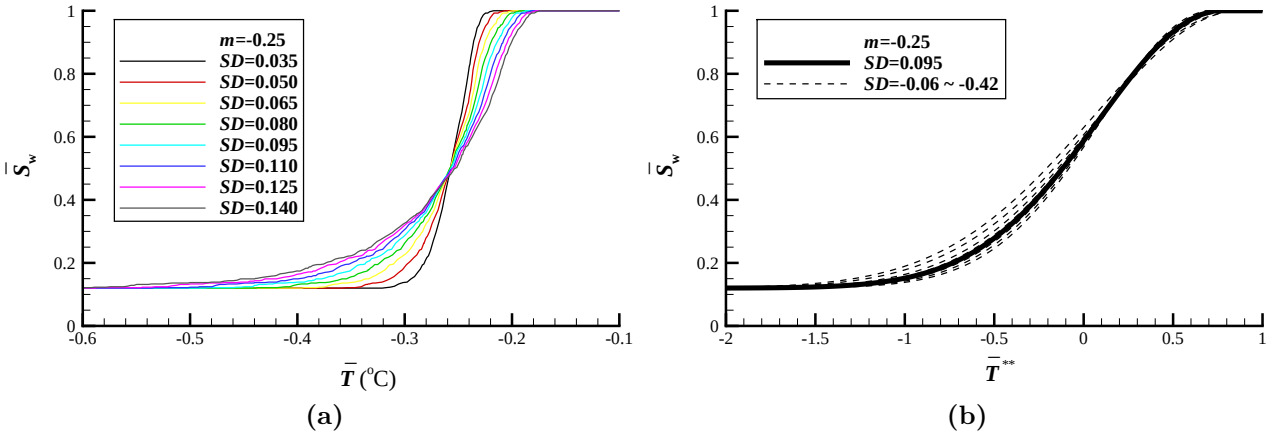

Figure 3.12 Effect of soil freezing point standard deviation on its freezing function: (a) model-generated SFCs, (b) Normalized Gaussian fitted SFCs

role. Figures 3.11b and 3.12b show that by normalizing the temperature, with the following equation,

$$\bar{T}^{**} = \frac{\left(\bar{T} - m_{T_\mathrm{f}}\right)}{SD_{T_\mathrm{f}}} \tag{3.21}$$

the soil freezing curves become identical. However, due to log-normally distributed freezing points of the realizations, there are some artifacts in the extreme case such that the mean is almost zero representing pure water. In this case, the freezing function gets straightened to mimic a sharp interface and cannot be resolved by Equation 3.21, which should only be considered valid for $m_{T_\mathrm{f}} < -0.1\,^{\circ}\mathrm{C}$.

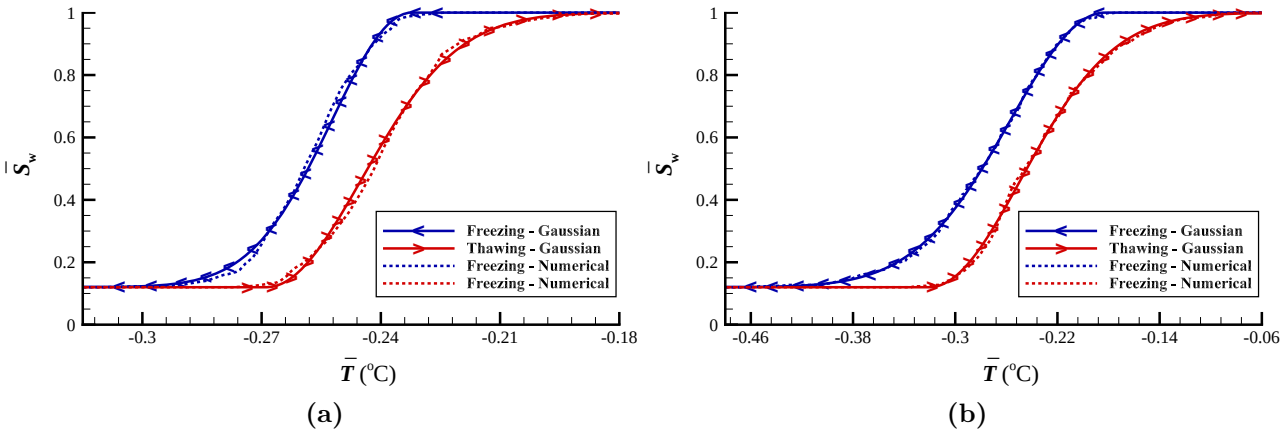

Figure 3.13 SFC hysteresis: (a) Heterogeneous thermal conductivity, (b) Heterogeneous freezing point depression.

3.3.4 Hysteresis in freeze-thaw conditions

After applying the procedure suggested in Section 3.2.2 for deriving the SFC for both freezing and thawing conditions, it was observed that the SFC obeys a hysteresis cycle during freeze-thaw, as is consistent with experimental observations (Koopmans and Miller, 1966). The hysteretic behavior of permafrost has been reported at many sites, including a peat plateau in Scotty Creek, Canada (Quinton and Baltzer, 2013) and in riparian peatlands of the western boreal forest, Canada (Smerdon and Mendoza, 2010). Two sets of realizations were run to capture the hysteretic behavior, and each set represents one condition (freeze or thaw). For the freezing scenario, a 10 m one-dimensional initially unfrozen soil column is considered (initial condition is 5 °C) subjected to a top surface freezing temperature of −5 °C at the freezing boundary. Whereas, for the thawing scenario, the same domain is assumed initially frozen (inital condition is −5 °C) and subjected to a top surface thawing temperature of 5 °C. As Figure 3.13 shows, the suggested process mimics the hysteretic behavior revealed in field data.

3.3.5 Comparison of heterogeneity-based SFCs and existing SFCs

As mentioned in Section 3.1, the existence of a slushy zone in soil is generally understood to be due to sorptive and capillary processes. Here, after testing the hypothesis that suggests another rationale for the existence of a slushy zone, we infer that this temperature range for pore water phase change can be partly ascribed to soil heterogeneities. Comparing the laboratory results reported by Koopmans and Miller (1966) and others reviewed by Kurylyk

and Watanabe (2013) to the results of this study, it is evident that the heterogeneity-induced temperature range for slushy zone, which varies between 0.1 to 0.3 °C, is narrower than those previously reported in lab results (e.g., about 2 °C but dependent on grain size and distribution). Clearly, sorptive and capillary processes appear to account for well over half the overall temperature range. However, the magnitude of heterogeneity effects are not inconsiderable in comparison, and may be particularly important for modeling systems on coarse grids where sub-cell heterogeneity will be present.

3.4 Conclusion

In this study, the effect of local sub-grid/sub-REV heterogeneity of soil thermal conductivity and depression point temperature on the SFC were investigated using a stochastic-conceptual approach. It was found that heterogeneity in soil thermal conductivity and depression point may be used to directly estimate an explicit functional form of the SFC for saturated porous media in the absence of capillary or sorptive forces. The range of temperatures over which the slushy zone was shown to exist in this study is narrower than those reported in laboratory studies or those commonly used in existing field-scale permafrost models for fine-grained soils, even in highly heterogeneous media. These discrepancies arise because capillary and sorptive processes can expand the temperature interval of freezing and thawing. Such processes have been studied for decades (Koopmans and Miller, 1966) and were not the focus of the present study. The temperature range for the slushy zone generated solely via thermal conductivity heterogeneity is only on the order of 0.2 °C for highly heterogeneous media, and the maximum range due solely to heterogeneity in water quality is on the order of 0.3 °C. While these ranges are small, they would be a significant portion of typical SFC ranges, particularly for those observed in coarse grained soils. Further studies will investigate how the SFC range due to heterogeneities as investigated in this study interfaces with the SFC range due to capillary and sorptive forces, but at present the ranges are hypothesized to be summative. This theoretical study suggests that the slushy zone extent can be different than that determined only from the SWCC-SFC relationship, and the results appears to be consistent with experimentally determined SFCs. Additionally, this approach suggests that a knowledge of the temperature gradient and the statistical parameters of soil thermal properties could be applied to obtain an estimate of the shape and extent of the SFC, i.e., parameters of Equation 3.18, can be obtained.

The proposed approach for generating the SFC led to closed-form relationships for the

SFC function that were dependent on the degree of soil and water quality heterogeneity, and collapse into the sharp front condition for pure (i.e. non-porous) media. While not yet extended to unsaturated systems where variability in water pressure will also play a significant role in controlling the SFC, the approach provides a theoretical justification for extending our understanding of both the shape and extent of the SFC in heterogeneous media. The approach has been shown to replicate the observed hysteretic ice saturation-temperature relation under freezing and thawing conditions, and may be used to help justifying the selection of an appropriate SFC function for both column and field-scale numerical studies of ice evolution in porous media. For practical application, we conjecture that the relative influence of the individual terms are likely to be roughly additive, i.e., the range in temperatures over which the freezing curve varies will be the sum of the ranges from heterogeneous media, heterogeneous depression point, and the traditional curve determined by analogy to SWCCs.

As a future extension to this work, different sources of heterogeneity can be applied conjunctively. Moreover, the effect of advective heat transfer in the characteristics of the slushy zone could be studied, as McKenzie et al. (2007) illustrated that advection accelerates soil's freeze-thaw processes. We expect that the inclusion of high rates of advection would likely compress the SFC temperature range due to heterogeneities as conductive processes would become less important. However, we would note that in ice-saturated medium, conduction is normally the dominant process (Williams and Smith, 1989).

Chapter 4

A trust region approach for numerical modeling of non-isothermal phase change

Statement of contribution

The following chapter is written based on the following article:

Amiri, E. A., Craig, J. R., and Hirmand, M. R. (2019). A trust region approach for numerical modeling of non-isothermal phase change. Computational Geosciences.

The paper is co-authored by myself, my supervisor, Dr. James R. Craig, and Dr. M. Reza Hirmand, post-doctoral fellow in the Department of Mechanical and Mechatronics Engineering at the University of Waterloo. I developed and implemented the algorithm in a computer program written in C++; designed and ran the test-case simulations; and wrote the manuscript. Dr. Craig provided supervision through the development of the mathematical formulations and editing the manuscript. Dr. Hirmand provided collaborative support through suggesting the implementation of a trust region scheme, developing the algorithm, and editing the manuscript.

4.1 Introduction

Permafrost underlies more than half of the exposed land in the Northwest territories of Canada and elsewhere in the northern hemisphere (Zhang et al., 1999). During the past decades, permafrost is thawing due to climate change particularly in regions of discontinuous permafrost around 60°N. The freeze/thaw processes in the soil have effects on climate change (Schuur et al., 2008, 2015), hydrology, and geotechnical properties. Thawing permafrost increases the rate of carbon release to the atmosphere due to high organic matter in the thawed soil and release of trapped carbon. In terms of hydrology, changes in soil freeze/thaw processes leads to changes in surface and subsurface water distribution and energy balance (Walvoord and Kurylyk, 2016). Moreover, presence of ice instead of water alters the thermo- hydro- geo-mechanical properties of soil (Chamberlain and Gow, 1979; Qi et al., 2006; Jamshidi et al., 2015). Proper representation of the phase-change process in water-saturated soil models is critical for 1) understanding controls on permafrost thaw and 2) simulating the impacts of climate change; thus, considering the phase-change process in the hydrological models is of importance. While many permafrost models have been developed in the literature (e.g. Hwang et al., 1971; Chamberlain and Gow, 1979), few of them performed convergence studies against grid and timestep sizes to examine robustness of their finite element models. Most implementations found in the literature use a relatively standard implementation of the Galerkin finite element method that is sensitive to the sharpness of the transition range of temperatures over which phase change occurs; with increasing sharpness, these methods can suffer from instability and may require excessively small timesteps. This time sensitivity manifests, in part, as inconsistent numerical convergence.

Permafrost modeling is essence a thermal problem, in which phase-change occurs within a temperature range. The simplest form of a phase change problem is called the Stefan Problem, which is the classic two phase/single media, sharp-interface solidification-liquefaction problem (a moving-boundary problem). The Stefan Problem was first introduced by Josef Stefan (a Slovenian physicist), whose research interest was polar ice cap melt. The history and review of the Stefan Problem is covered by Hill (1987). Evans (1951) presented existence of a solution for the Stefan Problem, and Douglas (1956) proved uniqueness of the solution. An analytical solution to this problem (the Neumann solution) is available in form of an explicit closed-form expression, which can be found in the studies done by Solomon (1966); Rathjen and Jiji (1971) and Crank (1999*b*). In the classic Stefan Problem, phase-change occurs only at the material's freezing point, i.e., sharp transition

from one phase to the other. Soil-water systems, however, undergo phase-change gradually within a finite range of temperature due to local heterogeneity in pore pressure, soil properties, and salinity (Amiri et al., 2018; Kurylyk and Watanabe, 2013). This is often accounted for by introducing a freezing function where liquid water saturation is given as a function of temperature $S_{\mathrm{w}}(T)$ which reverts to the Heaviside function (i.e., binary frozen/unfrozen) in the limit of the classic Stefan Problem. Lunardini (1985) proposed analytical solutions for linear, exponential, and quadratic freezing functions in soils, in which it was assumed that the heat transfer occurs via conduction only. Although analytical solutions exist for variations of the Stefan Problem, the solutions are restricted to very simple configurations. Analytical solutions are only available in 1-D (Hill, 1987; Alexiades and Solomon, 1993) or for 2-D settings with simple geometry and boundary conditions, e.g. the 2-D corner freezing problem presented by Rathjen and Jiji (1971). The simplicity of the problems with analytical solutions obliges us to use numerical treatments in practical applications. These solutions, however, provide benchmarks for the verification of numerical solutions (Kurylyk and Watanabe, 2013).

A variety of numerical schemes have been developed for simulating phase-change in both homogeneous media (e.g. water only) and soil-water systems. Comini et al. (1974) introduced a finite element model for nonlinear conductive heat transfer. In this model, latent heat is not taken into account explicitly. Rather, the effect of latent heat is applied to the bulk heat capacity by correcting and varying it rapidly within the freezing zone leading to a temperature-dependent "effective heat capacity". This has become the standard approach for handling smoothly continuous phase change. Morgan et al. (1978) showed that evaluating the heat capacity directly from the rate of change of enthalpy can lead to better results rather than averaging the heat capacity. The averaging technique is used to avoid missing any peak values of the effective heat capacity, which can lead to inaccuracy. Nedjar (2002) implemented a relaxed linearization procedure that is applicable to both stationary and transient heat transfer with an isothermal phase-change. Many numerical models have been presented to simulate the soil freezing and thawing processes and combine the soil freeze/thaw with the flow models of porewater. These models have been developed for various purposes, with different level of complexity, and using different numerical schemes. Grenier et al. (2018) conducted a thorough intercomparison between the existing permafrost models for 2-D cases, studied the sources of the discrepancies in the models' simulation results, and proposed test cases and guidelines for modelers to test their models. In their test cases, they showed that the existing models are in general agreement, particularly, the group of models that solve same equations and utilize same

characteristic curves. Even though the results are in agreement, there is still a need for alternate approaches that have improved convergence characteristics.

The major difficulty in modeling permafrost is to track the evolution of the freezing zone where the phase-change processes occur within the domain. One possible avenue of development would be to mathematically model the freezing zone as an interface whose evolution in the domain is described by an evolution law separate from the finite element heat transfer equation itself. In such approaches, the freezing zone may be modeled as a sharp interface (discontinuity) as in XFEM (Chessa et al., 2002), Discontinuous Galerkin (Nourgaliev et al., 2016), and mesh adaptive finite element methods (Provatas et al., 1998), or be smeared over a small region through regularization as in phase field formulations (Zheng et al., 2015). In the present work, an energy approach to phase change is proposed in which the freezing zone is tracked automatically as a part of the solution. The method entails minimization of a physically based potential derived from the governing boundary value problem through variational calculus. The method is distinct from usual finite element weak formulations in that the finite element discretization is directly applied to the potential functional, leading to a finite-dimensional minimization problem that must be solved at each timestep, see (Hirmand and Papoulia, 2018) for an application of a similar approach in the context of cohesive fracture. The proposed potential accounts for the latent heat capacity of the soil-water-ice system within the freezing zone by introducing a freezing/thawing function that is a highly non-linear, non-convex function of the unknown variable, i.e. temperature, in freezing temperature ranges (Dall'Amico et al., 2011). This necessitates the use of the trust-region minimization algorithm as the core ingredient of the proposed method. Standard and modified Newton's methods, e.g. Newton Raphson, Picard (Celia et al., 1990), and L-scheme (Pop et al., 2004; List and Radu, 2016), may fail to converge in certain cases when encountering locally non-convex or highly non-linear functions. We will investigate mathematical soundness of the trust region finite element formulation by performing convergence studies with grid size and timestep refinement and comparing this to the standard Galerkin approach. Few studies are available that investigate convergence of non-isothermal (i.e., non-sharp interface) treatment of phase change (Grenier et al., 2018).

Finally, the paper is organized as follows: formulation of the energy approach is presented in Section 4.2 where the governing boundary value problem and the proposed potential function will be presented. Three types of freezing functions (linear, Gaussian, and sinusoidal functions) used in the numerical simulations will also be presented in this section. Section 4.5 presents the trust-region minimization algorithm employed for the

solution of the minimization problem. Numerical simulation results including convergence studies with timestep and mesh refinement and verification with existing simplified solutions are presented in Section 4.6. Finally, Section 4.7 presents concluding remarks and proposes possible future work.

4.2 Formulation of the energy approach

While many phase-change problems are cast in terms of temperature as state variable, here, we use enthalpy, H [E]. Enthalpy is a thermodynamic quantity which represents the total heat energy of a system relative to some arbitrary energy state. In this approach, the phase-interface is calculated as a part of solution; thus, explicit tracking of the interface is not needed. It is historically interesting that the enthalpy approach was not originally introduced for simulating phase change but as an alternative formulation of heat conduction problems with varying thermal conductivity by Eyres et al. (1946).

Consider a domain $\Omega \subset \mathbb{R}^n$, $n \in \{1, 2, 3\}$, of a soil-water-ice system bounded externally by boundary Γ, as shown in Figure 4.1. The boundary Γ consists of disjoint parts Γ_{D} and Γ_{N} on which temperature $\overline{T}$ and heat flux $\overline{\mathbf{q}}$ are prescribed, respectively. It is assumed that the boundaries are mutually exclusive and collectively exhaustive ($\Gamma_{\mathrm{D}} \cap \Gamma_{\mathrm{N}} = \varnothing$ and $\Gamma_{\mathrm{D}} \cup \Gamma_{\mathrm{N}} = \Gamma$). Throughout this paper, we will use subscripts 'w', 'i', and 's' to refer the parameters associated with water, ice, and soil phases, respectively. The boundary value problem governing the conservation of energy in the body can be expressed in terms of enthalpy as (Ayasoufi and Keith, 2004)

$$\begin{aligned} \frac{\partial H(T)}{\partial T}\dot{T} + \nabla\cdot(\mathbf{v}H_{\mathrm{w}}(T)) &= -\nabla\cdot\mathbf{q} + \mathrm{h_b}, \\ \mathbf{q} &= -\overline{K}\nabla T, \\ T &= \overline{T} \qquad \text{on} \quad \Gamma_{\mathrm{D}}, \\ \mathbf{q} &= \overline{\mathbf{q}} \qquad \text{on} \quad \Gamma_{\mathrm{N}}, \end{aligned} \tag{4.1}$$

in which T [Θ] is temperature, and $H(T)$ [E] and $H_w(T)$ [E] are the enthalpy of soil-water-

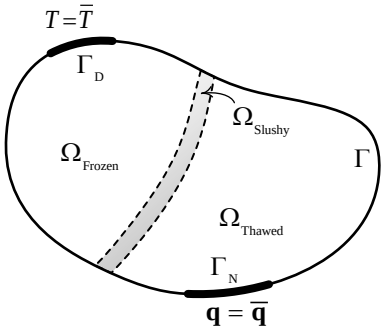

Figure 4.1 The domain Ω and relevant definitions. The frozen, slushy, and thawed zones of the soil-water-ice system are denoted by Ω_{Frozen}, Ω_{Slushy}, and Ω_{Thawed}, respectively

ice system and porewater, respectively, defined as

$$H(T) = \int_{T_{\text{ref}}}^{T} \overline{\rho c}(T)\, dT + L_{\text{h}} \left(S_{\text{w}}(T) - S_{\text{w}}^{\text{res}}\right), \tag{4.2}$$

$$H_w(T) = n\rho_{\text{w}} c_{\text{w}} \int_{T_{\text{ref}}}^{T} S_{\text{w}}(T)\, dT, \tag{4.3}$$

where n, S, ρ [ML^{-3}], c [$\text{EM}^{-1}\Theta^{-1}$], and K [$\text{MLT}^{-3}\Theta^{-1}$] are the porosity, saturation, density, bulk heat capacity, and thermal conductivity, respectively. Furthermore, $\overline{\rho c}$ [$\text{EL}^{-3}\Theta^{-1}$], $\overline{K}$ [$\text{MLT}^{-3}\Theta^{-1}$], h_b [ET^{-1}] and L_{h} [E] are apparent bulk heat capacity, apparent thermal conductivity, the energy due to body heat flux and latent heat of fusion, respectively. The second term in Equation 4.2 represents the latent heat capacity induced in the system during the phase-change process. T_{ref} is an arbitrary reference temperature below the freezing range. The temperature-dependent bulk media properties, i.e., $\overline{\rho c}$ and $\overline{K}$, are expressed as (Walvoord and Kurylyk, 2016)

$$\overline{\rho c}(T) = n(S_{\text{w}}(T)\, \rho_{\text{w}} c_{\text{w}} + (1 - S_{\text{w}}(T))\rho_{\text{i}} c_{\text{i}} + (1-n)\rho_{\text{s}} c_{\text{s}}, \tag{4.4}$$

$$\overline{K}(T) = {K_{\text{w}}}^{S_{\text{w}} n} {K_{\text{i}}}^{S_{\text{i}} n} K_{\text{s}}^{(1-n)}. \tag{4.5}$$

One can calculate the apparent thermal conductivity by averaging the thermal conductivity of soil components arithmetically or harmonically. In the case that multi-dimensional heat transfer occurs, geometric averaging is preferable and can be calculated by Equation 4.5 (Walvoord and Kurylyk, 2016).

The phase-change or slushy zone (Ω_{Slushy}) is defined by the region where the temperature is in the interval defined by the freezing temperature T_{F} and and thawing temperature T_{T}, i.e. $T_{\text{F}} \leqslant T \leqslant T_{\text{T}}$ in Ω_{Slushy}. The relation between water saturation and temperature

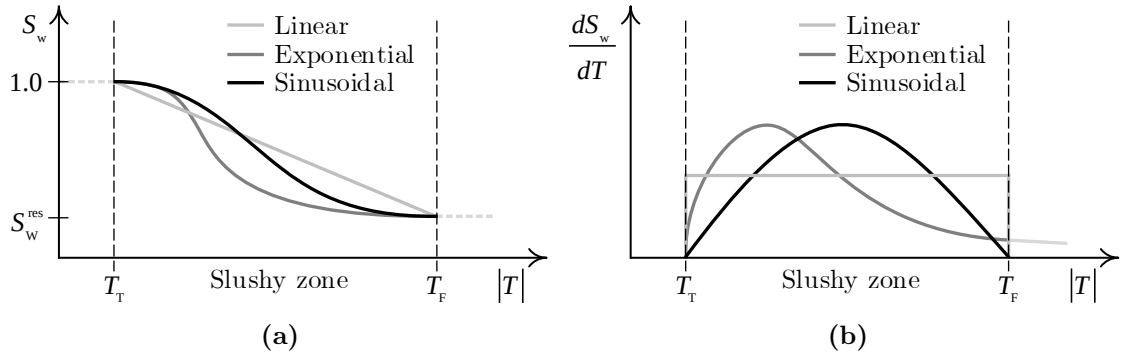

Figure 4.2 Soil freezing function schematics: (a) Freezing functions, (b) Derivatives of the functions

in this zone is technically hysteretic (Tian et al., 2014), but often a non-hysteretic is employed in numerical applications by defining a single soil freezing function (SFC), $S_{\mathrm{w}}(T)$. Two commonly used freezing functions include linear and Gaussian functions (McKenzie et al., 2007). Here, in addition, a sinusoidal freezing function is implemented. The linear, exponential and sinusoidal freezing functions are expressed in $T_{\mathrm{F}} \leqslant T \leqslant T_{\mathrm{T}}$, i.e. within the slushy zone, as

$$S_{\mathrm{w}}(T) = \frac{1 - S_{\mathrm{w}}^{\mathrm{res}}}{T_{\mathrm{F}} - T_{\mathrm{T}}} \left(T - T_{\mathrm{T}}\right) + S_{\mathrm{w}}^{\mathrm{res}}, \tag{4.6}$$

$$S_{\mathrm{w}}(T) = \left(1 - S_{\mathrm{w}}^{\mathrm{res}}\right) \exp\left[-\left(\frac{T - T_{\mathrm{f}}}{\beta}\right)^2\right] + S_{\mathrm{w}}^{\mathrm{res}}, \tag{4.7}$$

$$S_{\mathrm{w}}(T) = \frac{1 - S_{\mathrm{w}}^{\mathrm{res}}}{2} \sin\left(\frac{T - 0.5\left(T_{\mathrm{T}} + T_{\mathrm{F}}\right)}{T_{\mathrm{T}} - T_{\mathrm{F}}}\pi\right) + \frac{1 + S_{\mathrm{w}}^{\mathrm{res}}}{2}, \tag{4.8}$$

where $S_{\mathrm{w}}^{\mathrm{res}}$ is the residual water saturation and β is a shape parameter. Consistent with the above definitions, the liquid water saturation is assumed to be 1.0 in the thawed zone Ω_{Thawed} (i.e., where $T > T_{\mathrm{T}}$) and $S_{\mathrm{w}}^{\mathrm{res}}$ in the frozen zone Ω_{Frozen} (i.e., where $T > T_{\mathrm{F}}$). The derivatives of the above freezing functions are expressed as:

$$\frac{dS_{\mathrm{w}}}{dT}(T) = \frac{1 - S_{\mathrm{w}}^{\mathrm{res}}}{T_{\mathrm{F}} - T_{\mathrm{T}}}, \tag{4.9}$$

$$\frac{dS_{\mathrm{w}}}{dT}(T) = -2\left(1 - S_{\mathrm{w}}^{\mathrm{res}}\right) \frac{T - T_{\mathrm{f}}}{\beta^2} \exp\left[-\left(\frac{T - T_{\mathrm{f}}}{\beta}\right)^2\right], \tag{4.10}$$

$$\frac{dS_{\mathrm{w}}}{dT}(T) = \frac{\pi\left(1 - S_{\mathrm{w}}^{\mathrm{res}}\right)}{2\left(T_{\mathrm{T}} - T_{\mathrm{F}}\right)} \cos\left(\frac{T - 0.5\left(T_{\mathrm{T}} + T_{\mathrm{F}}\right)}{T_{\mathrm{T}} - T_{\mathrm{F}}}\pi\right). \tag{4.11}$$

The schematics of the freezing functions and their derivatives are illustrated in Figure 4.2. To avoid numerical issues, it is generally preferable to use smooth and globally differentiable freezing functions. Since the linear freezing function contains two non-differentiable points (at $T = T_{\mathrm{T}}$ and $T = T_{\mathrm{F}}$), the use of exponential and sinusoidal forms of the freezing function is preferable. The non-linear soil freezing functions in Equations 4.6 to 4.8 make the governing boundary value problem presented in this section non-linear in nature.

4.3 Derivation of potential function

The present work follows the procedure of calculating the variational form of a BVP discussed in Bhatti (2005). Integrating the product of the energy conservation equation (Equation 4.1 without advective and body force terms) multiplied by the test function δT over the domain Ω, applying the divergence theorem and taking into account the boundary conditions leads to

$$\delta\pi = \int_{\Omega} \delta T \left(\frac{\partial H(T)}{\partial T} \dot{T} - \nabla \cdot \left(\overline{K} \nabla T \right) \right) dV. \tag{4.12}$$

It follows,

$$\begin{aligned}
\delta\pi &= \int_{\Omega} \delta T \left(\frac{\partial H(T)}{\partial T} \dot{T} - \nabla . \left(K\left(T\right) \nabla T \right) \right) dV \\
&= \int_{\Omega} \delta T \left(\frac{\partial H(T)}{\partial T} \frac{T - \hat{T}}{\gamma \Delta t} - \nabla . \left(K\left(T\right) \nabla T \right) \right) dV \\
&= \underbrace{\frac{1}{\gamma \Delta t} \int_{\Omega} \delta T \frac{\partial H(T)}{\partial T} T dV}_{\delta\pi^{\mathrm{I}}} \underbrace{- \frac{\hat{T}}{\gamma \Delta t} \int_{\Omega} \delta T \frac{\partial H(T)}{\partial T} dV}_{\delta\pi^{\mathrm{II}}} \underbrace{- \int_{\Omega} \delta T \nabla \cdot \left(\overline{K} \nabla T \right) dV}_{\delta\pi^{\mathrm{III}}},
\end{aligned} \tag{4.13}$$

which implies that $\pi = \pi^{\mathrm{I}} + \pi^{\mathrm{II}} + \pi^{\mathrm{III}}$. In what follows, we will obtain π^{I}, π^{II} and π^{III}. Recall that $G(T) = \int_{T_{ref}}^{T} \frac{\partial H(T)}{\partial T} T dT$, see Equation 4.33. Applying integration by parts yield

$$G(T) = H(T)\, T - \int_{T_{ref}}^{T} H(T)\, dT. \tag{4.14}$$

π^{I} is derived as

$$\delta\pi^{\mathrm{I}} = \delta\left(\frac{1}{\gamma\Delta t}\int_{\Omega} G(T)\,dV\right), \tag{4.15}$$

$$\pi^{\mathrm{I}} = \frac{1}{\gamma\Delta t}\int_{\Omega} G(T)\,dV. \tag{4.16}$$

Following the same procedure, π^{II} is calculated as

$$\delta\pi^{\mathrm{II}} = \delta\left(-\frac{\hat{T}}{\gamma\Delta t}\int_{\Omega} H(T)\,dV\right), \tag{4.17}$$

$$\pi^{\mathrm{II}} = -\frac{\hat{T}}{\gamma\Delta t}\int_{\Omega} H(T)\,dV. \tag{4.18}$$

For derivation of π^{III} we follow the same procedure:

$$\begin{aligned}
\delta\pi^{\mathrm{III}} &= -\int_{\Omega} \delta T\left(\nabla\cdot\left(\overline{K}\nabla T\right)\right) dV \\
&= \underbrace{-\int_{\Gamma} \delta T\overline{K}\nabla T\cdot\tilde{\mathbf{n}}dS}_{0} + \int_{\Omega}\overline{K}\left(\nabla\delta T\nabla T\right) dV \\
&= \delta\left(\frac{1}{2}\int_{\Omega}\overline{K}(\nabla T\cdot\nabla T)\,dV\right), \qquad (4.19)\\
\pi^{\mathrm{III}} &= \frac{1}{2}\int_{\Omega}\overline{K}(\nabla T\cdot\nabla T)\,dV. \qquad (4.20)
\end{aligned}$$

In an inverse procedure, one could equivalently show that the variation of π leads to the expression given for $\delta\pi$ in equation Equation 4.31.

4.4 Matrix equations

In order to formulate a finite element solution to the problem given by Equations 4.31 and 4.32, the approximate trial and test functions T_h and δT_h are sought within finite dimensional spaces $\mathbb{T}_h$ and $\delta\mathbb{T}_h$ spanned by linearly independent finite element basis functions which approximate $\mathbb{T}$ and $\delta\mathbb{T}$, respectively. The finite element approximations to the

trial and test functions, T_h and δT_h, are expressed as

$$T_h = \tilde{\mathbf{N}}^T \tilde{\mathbf{T}}, \tag{4.21}$$

$$\delta T_h = \tilde{\mathbf{N}}^T \delta\tilde{\mathbf{T}}, \tag{4.22}$$

respectively, where $\tilde{\mathbf{N}}$ contains the finite element shape functions and $\tilde{\mathbf{T}}$ and $\delta\tilde{\mathbf{T}}$ represent nodal unknowns.

Substituting the finite element approximations Equations 4.21 and 4.22 in Equation 4.31, and noting that $\delta\pi_h = \delta\tilde{\mathbf{T}} \cdot \nabla\pi_h\left(\tilde{\mathbf{T}}\right)$, it is straightforward to obtain the corresponding discrete gradient $\nabla\pi_h\left(\tilde{\mathbf{T}}\right) = \mathbf{g}\left(\tilde{\mathbf{T}}\right)$ as

$$\mathbf{g}\left(\tilde{\mathbf{T}}\right) = \mathbf{H}\tilde{\mathbf{T}} + \tilde{\mathbf{M}}\left(\tilde{\mathbf{T}}\right) + \tilde{\mathbf{F}}, \tag{4.23}$$

where

$$\mathbf{H} = \int_\Omega \mathbf{B}^T \overline{K}\mathbf{B} dV, \tag{4.24}$$

$$\tilde{\mathbf{M}} = \int_\Omega \tilde{\mathbf{N}}^T \frac{\partial H(T)}{\partial T}\dot{\tilde{\mathbf{T}}} dV, \tag{4.25}$$

$$\tilde{\mathbf{F}} = \int_\Gamma \tilde{\mathbf{N}}^T \overline{\mathbf{q}} \cdot \tilde{\mathbf{n}} dS, \tag{4.26}$$

and $\mathbf{B}$ is a matrix containing the spatial derivatives of finite element shape function defined as $\mathbf{B} = \nabla\tilde{\mathbf{N}}$.

The Hessian matrix $\mathbf{H}_{total} = \nabla^2\pi_h\left(\tilde{\mathbf{T}}\right)$, which may be viewed as being the equivalent stiffness matrix in a standard Newton-Raphson scheme, is obtained as follows:

$$\begin{aligned}
\mathbf{H}_{\text{total}} &= \frac{\partial\Psi}{\partial\tilde{\mathbf{T}}} \\
&= \mathbf{H} + \frac{\partial\tilde{\mathbf{M}}}{\partial\tilde{\mathbf{T}}} \\
&= \mathbf{H} + \frac{\partial\tilde{\mathbf{M}}}{\partial\dot{\tilde{\mathbf{T}}}}\frac{\partial\dot{\tilde{\mathbf{T}}}}{\partial\tilde{\mathbf{T}}} \\
&= \mathbf{H} + \frac{1}{\gamma\Delta t}\int_\Omega \tilde{\mathbf{N}}^T \frac{\partial H(T)}{\partial T}\tilde{\mathbf{N}} dV.
\end{aligned} \tag{4.27}$$

4.4.1 Variational formulation

We now consider the time discrete case with N timesteps uniformly spaced with time intervals Δt: $t \in \{0, t_1, t_2, ..., t_n, t_{n+1}, ..., t_N\}$, where $\Delta t = t_{n+1} - t_n$. Suppose that that the solution $T_n \equiv T(\mathbf{x}, t_n)$ is known at timestep t_n and the solution $T_{n+1} \equiv T(\mathbf{x}, t_{n+1})$ is sought at timestep t_{n+1}. We make use of the generalized Newmark scheme for time domain integration in which the link between the time derivatives of the unknown field in successive timesteps is made in an implicit fashion as

$$T_{n+1} = \hat{T}_{n+1} + \gamma \Delta t \dot{T}_{n+1}, \tag{4.28}$$

in which γ is the Newmark Coefficient and $\hat{T}_{n+1} = T_n + (1-\gamma)\Delta t \dot{T}_n$. The method is unconditionally stable for $\gamma \geq 0.5$. Here and subsequently, we shall omit the subscript $n+1$ for simplicity; the formulation that follows concerns solution of the problem at a given timestep t_{n+1}. The spaces of admissible trial and test functions are defined as follows:

$$\mathbb{T} = \{T \in H^1(\Omega) \quad | \quad T = \bar{T} \quad \text{on} \quad \Gamma_{\mathrm{D}}\}, \tag{4.29}$$

$$\delta\mathbb{T} = \{\delta T \in H^1(\Omega) \quad | \quad \delta T = 0 \quad \text{on} \quad \Gamma_{\mathrm{N}}\}. \tag{4.30}$$

in which the space H^1 concerns the regularity requirement of the solution spaces. The variational formulation representing a weak formulation of the boundary value problem defined by Equation 4.1 is obtained by seeking the stationary point of a potential functional π. This may be restated as: Find $T \in \mathbb{T}$ s.t. $\delta\pi = 0 \ \forall \delta T \in \delta\mathbb{T}$, where the variation $\delta\pi$ and the corresponding potential π (for conductive heat transfer and $\mathrm{h_b} = 0$) are defined in Section 4.3 by integrating Equation 4.1 multiplied by a test function δT

$$\delta\pi = \int_\Omega \delta T \left(\frac{\partial H(T)}{\partial T} \dot{T} - \nabla \cdot \left(\overline{K} \nabla T \right) \right) dV, \tag{4.31}$$

then, subsequently, the potential functions is derived as:

$$\pi = \frac{1}{\gamma \Delta t} \int_\Omega G(T)\, dV - \frac{\hat{T}}{\gamma \Delta t} \int_\Omega H(T)\, dV + \frac{1}{2} \int_\Omega \overline{K} (\nabla T \cdot \nabla T)\, dV. \tag{4.32}$$

For the details regarding the derivation of the potential Equation 4.32, the reader is referred to Section 4.3. In the above, the function $G(T)$ is defined as

$$G(T) = \int_{T_{ref}}^{T} \frac{\partial H(T)}{\partial T} T dT. \tag{4.33}$$

It is worth noting that the particular form of the potential Equation 4.32 depends on the type of the temporal discretization scheme employed due to the presence of time derivatives of the temperature filed, $\dot{T}$.

4.5 Solution strategy: the trust region algorithm

In a usual solution strategy, one would now linearize the discrete finite element equations arising from Equation 4.31 within a standard iterative Newton-Raphson scheme. While this would still be a valid approach, we found that standard Newton-Raphson procedures fail to converge in many scenarios. This is firstly due to the highly non-linear nature of the problem at hand, and secondly due the non-convex form of the enthalpy function in potential Equation 4.32 which may affect the definiteness of the Jacobian matrix, a requirement of the standard Newton-Raphson scheme. We, therefore, approach the solution to the variational formulation expressed through Equations 4.31 and 4.32 from an energy minimization perspective using the trust region minimization algorithm (Nocedal and Wright, 2006). The trust region algorithm always converges to a solution and is notably capable of handling non-convex objective functions. It is known that the second-order necessary conditions for minimality will be satisfied at the termination point (Nocedal and Wright, 2006). The present approach also has a firm physical basis and, to the best of authors' knowledge, is the first application of energy minimization methods in modeling phase-change processes.

We apply a finite element discretization to Equation 4.32 and tackle the resulting finite dimensional minimization problem. Let $\pi_h(\mathbf{T})$ denote the discrete potential resulting from applying the finite element discretization to $\pi(T)$, where $\mathbf{T}$ is the vector of nodal unknowns. The trust region algorithm used for the minimization of $\pi_h(\mathbf{T})$ is outlined in Table 4.1. The algorithm seeks the solution to the following constrained minimization problem in each of its iterations

$$\min_{d\mathbf{T}\in\mathbb{R}^n} m_k(d\mathbf{T}) = \pi_h(\mathbf{T}_k) + \mathbf{g}\cdot d\mathbf{T} + \frac{1}{2} d\mathbf{T}\cdot \mathbf{H}\cdot d\mathbf{T} \quad \text{s.t.} \quad \|d\mathbf{T}\| \leqslant \Delta_k, \tag{4.34}$$

Table 4.1 Trust-region algorithm description

At timestep $n+1$ and iteration k; given $\bar{\Delta} > 0$, $\Delta \in \big(0, \bar{\Delta}\big)$, and $\bar{\eta} \in \big[0, \frac{1}{4}\big)$
Trust region loop: $k = 1, 2, ...$ until convergence:
    Convergence critera:
        if $\frac{\|\mathbf{g}(\mathbf{T}_k)\|}{\|\mathbf{g}(\mathbf{T}_0)\|} \leq \epsilon_{\mathbf{g}}$ **and** $\frac{\pi_h(\mathbf{T}_k) - \pi_h(\mathbf{T}_{k-1})}{\pi_h(\mathbf{T}_0)} \leq \epsilon_\pi \rightarrow$ converged, next n
    Minimize Equation 4.34 and solve for $d\mathbf{T}_k^*$
    Calculate $\eta_k = \frac{\pi_h\big(\tau + d\mathbf{T}_k^*\big) - \pi_h(\tau)}{m_k\big(d\mathbf{T}_k^*\big) - m_k(0)}$
    if $\eta_k < \frac{1}{4}$
        $\Delta_{k+1} = \frac{1}{4}\Delta_{k+1}$
    else
        if $\eta_k > \frac{3}{4}$ and $\|d\mathbf{T}_k^*\| = \Delta_k$
            $\Delta_{k+1} = \min\big(2\Delta_{k+1}, \bar{\Delta}\big)$
        else
            $\Delta_{k+1} = \Delta_k$
    if $\eta_k > \bar{\eta}$
        $\mathbf{T}_{k+1} = \mathbf{T}_k + d\mathbf{T}_k^*$
    else
        $\mathbf{T}_{k+1} = \mathbf{T}_k$
End of trust region loop

where k is the iteration index and $m_k(d\mathbf{T})$ is a quadratic model of the potential around $\mathbf{T}_k$ obtained from the first three terms of the Taylor series expansion of π_h with $\mathbf{g} = \nabla\pi_h(\mathbf{T}_k)$ and $\mathbf{H} = \nabla^2\pi_h(\mathbf{T}_k)$ being the gradient and Hessian of the discrete potential, respectively. For the details regarding the matrix form of the gradient and Hessian of the potential, the reader is referred to Appendix B. Since the model is more accurate near $\mathbf{T}_k$, the method tries to find a minimum within a sphere of radius Δ_k in which the model can be "trusted". We note here that were it not for the constraint $\|d\mathbf{T}\| \leqslant \Delta_k$, the trust region method would correspond exactly to the Newton-Raphson method in the case of a positive definite Hessian. We recall that the Newton-Raphson iteration essentially minimizes a quadratic model of the objective function on each of its iterations.

The iteration is initialized with an initial approximate solution $\mathbf{T}_0$, which is taken to be the converged solution from the previous timestep, and an initial trust region radius Δ_0, which is taken to be correlated with the size of the freezing temperature range in our implementation. Within each iteration, a solution $d\mathbf{T}_k^*$ to Equation 4.34 is accepted as a valid increment in $\mathbf{T}$ only if the actual change to π_h given by $\pi_h(\mathbf{T}_k + d\mathbf{T}_k^*) - \pi_h(\mathbf{T}_k)$ is "big" enough compared to the reduction induced in the quadratic model given by $m_k(\mathbf{0}) - m_k(d\mathbf{T}_k^*)$, see the ratio η_k defined in Table 4.1. Additionally, the method modifies the size of the trust region from one iteration to the next based on the value of η, so that Δ_{k+1} could be twice

as large, twice as small, or equal to Δ_k. The iterations are terminated when the desired tolerance for the first order minimality condition, i.e. $||\nabla\pi|| \leq \epsilon_\pi$, is achieved. It should be noted that the solution obtained is not sensitive to the values chosen for Δ_0, $\bar{\Delta}$, and $\bar{\eta}$. However, these parameters can affect the number of iterations required to converge and must therefore be chosen wisely for each unique problem to optimize computational cost. We took $\Delta_0 = 10^2\,^\circ$C, $\bar{\Delta} = 10^3\,^\circ$C and $\bar{\eta} = 0.1$ in the numerical simulations presented in Section 4.6.

In order to solve the constrained minimization subproblem defined by Equation 4.34, various approximate methods such as the Dogleg or Conjugate gradient method could be used (Nocedal and Wright, 2006). In the present work, we use the "nearly exact" method of More and Sorensen (Nocedal and Wright, 2006; More and Sorensen, 1983) particularly because of its capability in handling indefinite Hessians. The method reduces Equation 4.34 to a 1-D root finding problem expressed as $p(\lambda) = \Delta_k$, $p(\lambda) = -(\mathbf{H}(\mathbf{T}_k) + \lambda\mathbf{I})^{-1}\mathbf{g}(\mathbf{T}_k)$, which must be solved for λ. It has been proven (More and Sorensen, 1983) that the trust region algorithm converges to a solution $\mathbf{T}_k$ or a limiting value $\mathbf{T}^*$ in the limit of $k \to \infty$ that satisfy the second-order optimality conditions (i.e., $\mathbf{g} = \mathbf{0}$ and $\mathbf{H}$ positive semi-definite). For more details on the theoretical convergence proof of the nearly-exact trust region algorithm, the reader is referred to the work of More and Sorensen (1983).

4.6 Numerical simulation results

In this section, numerical finite element solutions of various 1-D and 2-D problems are presented based on the trust region methodology presented in the previous section. Solutions are initially verified against existing analytical solutions for a 1-D soil column. In addition, convergence studies are conducted in both 1-D and 2-D to examine robustness of the finite element formulation and dependence of the results on timestep and mesh sizes. The material and solution properties used in the simulations are found in Table 4.2.

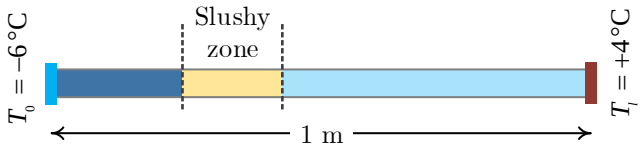

Figure 4.3 1-D problem domain configuration: geometry and boundary conditions. $\Delta T = T_1 - T_0$

Table 4.2 Properties used in simulations

Parameters	Values	Parameters	Values
K_{s} $\left[\mathrm{W.m^{-1}.K^{-1}}\right]$	0.1	K_{i} $\left[\mathrm{W.m^{-1}.K^{-1}}\right]$	2.14
c_{s} $\left[\mathrm{J.kg^{-1}.K^{-1}}\right]$	630	c_{i} $\left[\mathrm{J.kg^{-1}.K^{-1}}\right]$	2108
ρ_{s} $\left[\mathrm{kg.m^{-3}}\right]$	250	ρ_{i} $\left[\mathrm{kg.m^{-3}}\right]$	920
n (porosity)	0.8	L_{heat} $\left[\mathrm{J.kg^{-1}}\right]$	334000
$S_{\mathrm{w}}^{\mathrm{res}}$	0	Δt [s]	28 to 7200
K_{w} $\left[\mathrm{W.m^{-1}.K^{-1}}\right]$	0.58	ϵ_{π}	1.0E–6
c_{w} $\left[\mathrm{J.kg^{-1}.K^{-1}}\right]$	4187	ϵ_{g}	1.0E–5
ρ_{w} $\left[\mathrm{kg.m^{-3}}\right]$	1000		

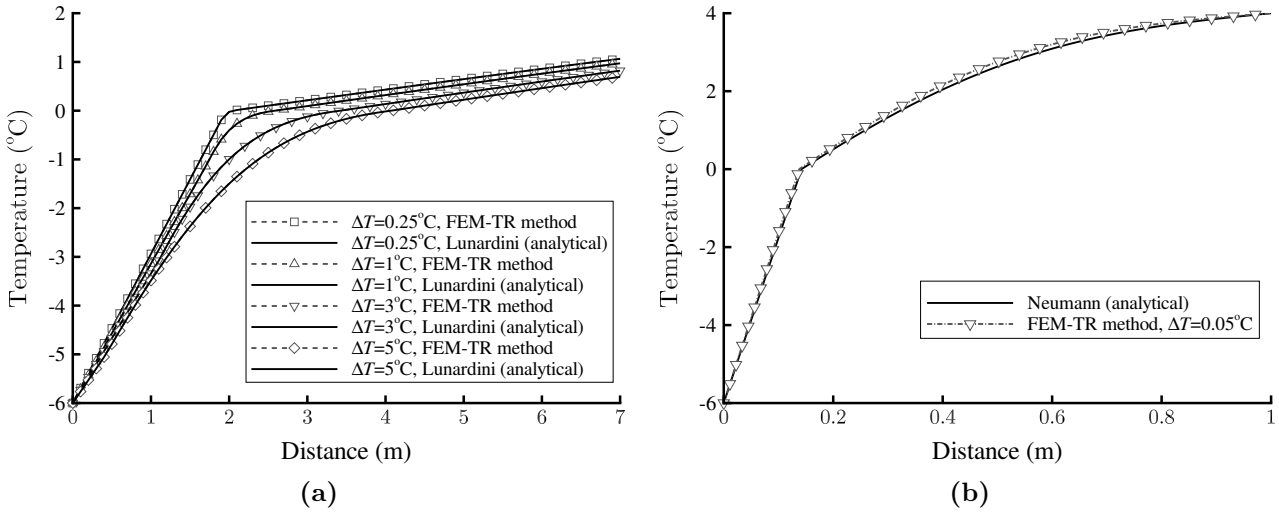

Figure 4.4 Verifying FEM-TR model against: (a) the analytical solution for non-isothermal phase-change presented by Lunardini (1981), (b) Neumann's analytical solutions for a near isothermal phase-change

4.6.1 One-dimensional soil column

The numerical solution is verified against an analytical solution presented by Lunardini (1981) for a three-zone 1-D domain with non-isothermal phase change. The geometry of the problem along with the boundary conditions are give in Figure 4.3. The three frozen, slushy, and thawed zones were all taken into account in the analytic solution. As evident in Figure 4.4a, the FEM-trust-region (FEM-TR) model developed here precisely matches the analytical solution for a fairly wide range of freezing temperature intervals $\Delta T = T_T - T_F$, from $\Delta T = 0.25°\mathrm{C}$ to $\Delta T = 5°\mathrm{C}$. In order to test the model for the case approaching an

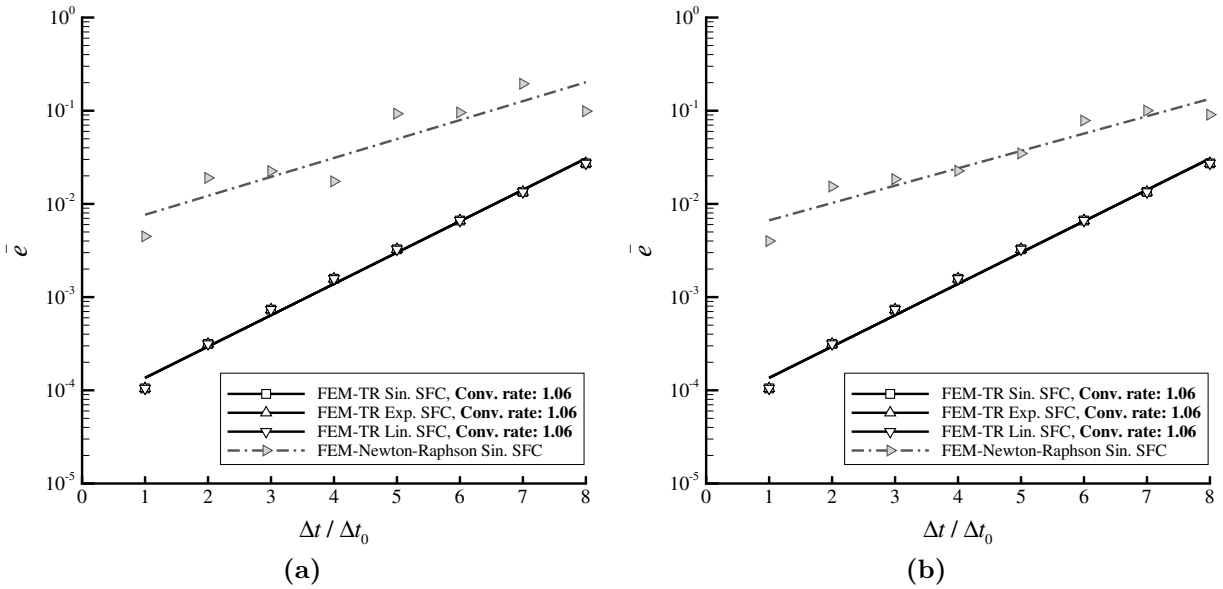

Figure 4.5 Comparison between FEM-TR and FEM-Newton-Raphson methods by varying (a) timestep size for freezing temperature range of 0.25°C and (b) timestep size for freezing temperature range of 1°C

isothermal phase-change (i.e., sharp interface criterion), we solved the problem with a very small freezing temperature interval as $\Delta T = 0.05$°C (-0.05°C to 0°C). Results shown in Figure 4.4b indicate that for a freezing temperature range of 0.05°C, the slushy-zone gets narrower as expected and the solution converges to the Neumann analytical solutions.

We also performed temporal and spatial convergence studies to examine robustness of the proposed FEM-TR model with regards to independence of the results from timestep and mesh grid sizes. In each case, two freezing temperature intervals of $\Delta T = 0.25$°C and $\Delta T = 1$°C are considered to show that the numerical results are insensitive to this input parameter. Results of the temporal and spatial convergence studies are shown in Figures 4.5 and 4.6. In these graphs, the normalized error norm (L^2 norm) in s defined as

$$\bar{e} = \frac{\sqrt{\int_\Omega (T_{\text{numerical}} - T_{\text{exact}}) \cdot (T_{\text{numerical}} - T_{\text{exact}})\, dV}}{\sqrt{\int_\Omega T_{\text{exact}} \cdot T_{\text{exact}} dV}}, \tag{4.35}$$

where T_{exact} is the analytical solution and $T_{\text{numerical}}$ is the solution obtained from the numerical simulation. It should be noted that, in the convergence studies, T_{exact} is taken to be the solution for the smallest timestep (in the timestep convergence study) or the solution for the finest mesh (in the mesh convergence study). For the temporal convergence study (Figure 4.5), the mesh was kept fixed (500 uniform elements) and the problem was

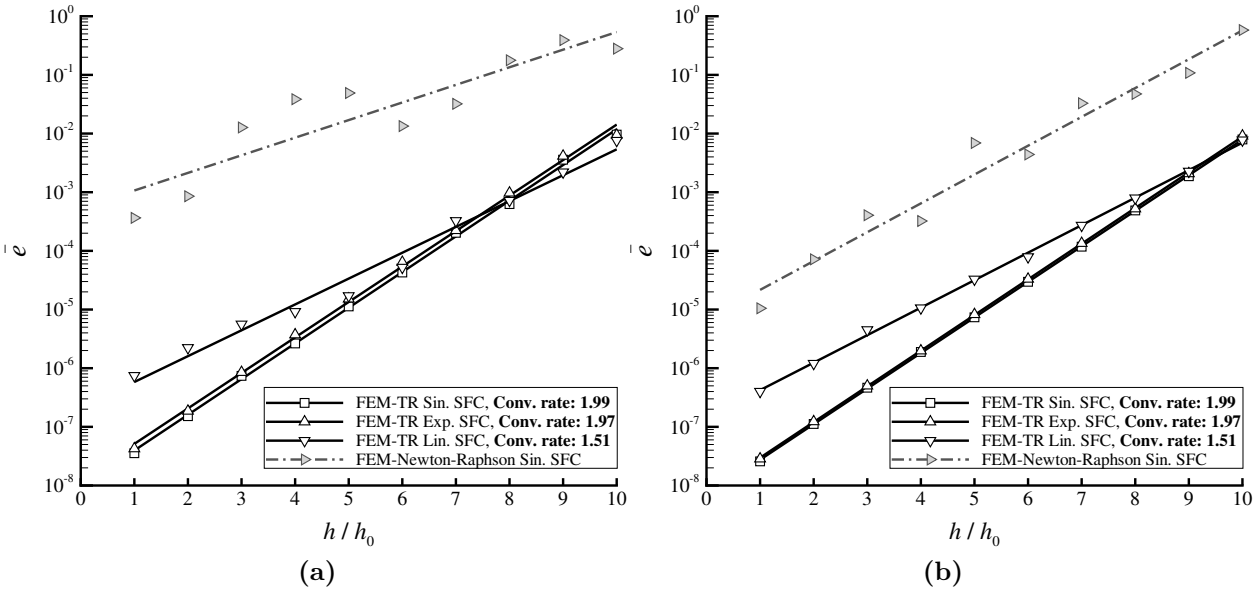

Figure 4.6 Comparison between FEM-TR and FEM-Newton-Raphson methods by varying (a) mesh size for freezing temperature range of 0.25°C and (b) mesh size for freezing temperature range of 1°C

solved for a series of successively increasing timestep sizes $\Delta t_i = \Delta t_0 \times 2^i$, $i = 0 : 8$, where $\Delta t_0 = 28.125\,\text{sec}$. For a temporally convergent method, one expects the rate of convergence with timestep refinement corresponding to the Newmark's scheme to be equal to 1.0 in a log-log scale. We observe that this rate is recovered in the numerical simulation results irrespective of the size of the freezing temperature interval.

Next, we consider convergence with mesh size refinement shown in Figure 4.6. Results were obtained by solving the problem with a fixed timestep size $\Delta t = 1800\,\text{sec}$ (total solution time $t_N = 5.4 \times 10^5 \text{sec}$) on a sequence of 10 FE meshes, each one having an element size twice as small as the previous one. The finest mesh used was obtained by a uniform discretization of the 1D domain with 10240 elements, i.e., $h_0 \simeq 10^{-4}$. As can be observed in Figure 4.6, the estimated asymptotic rate of convergence in $\bar{e}$ is approximately 2.0 as expected from the linear two-noded elements used in our finite element implementation. We notice that the results obtained with the linear SFC show slightly sub-optimal convergence rates, which may be attributed to the discontinuity introduced by the derivative of this function at the boundaries of the freezing zone region. These results confirm that the proposed algorithm preserves robustness of the finite element method and is free of non-physical timestep and mesh size dependence. We also report the results obtained by a standard Newton-Raphson's scheme in which the convergence criterion of the iterations was significantly relaxed compared to the one used for the trust-region iteration (i.e., using

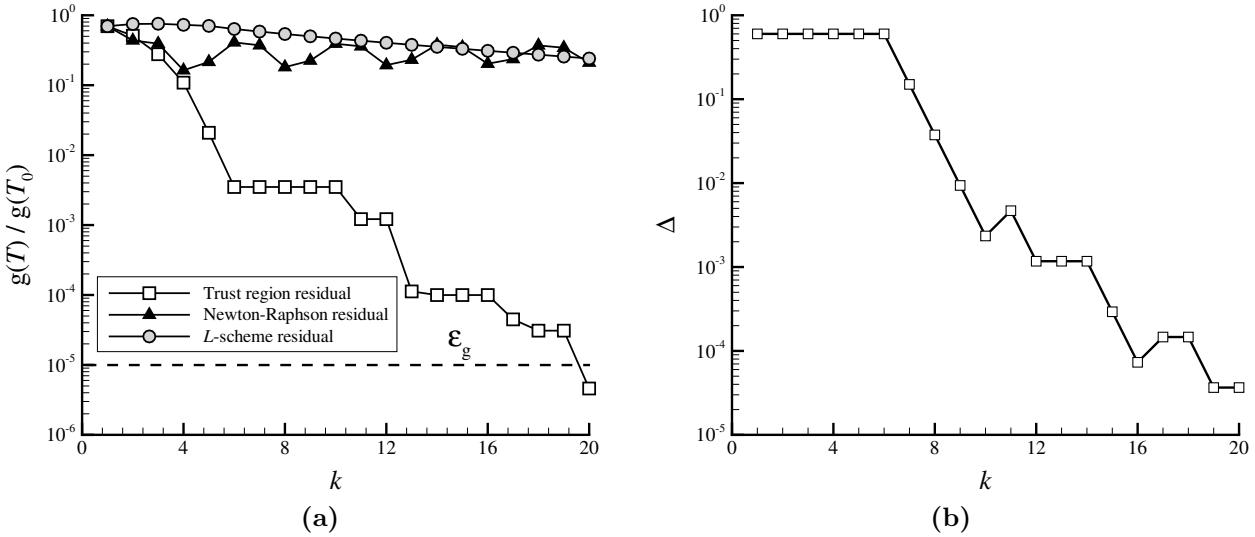

Figure 4.7 Comparison between trust region, Newton-Raphson, and L-scheme algorithms: (a) residuals and (b) trust region radius.

a relatively large $\epsilon_g = 10^{-2}$). As can be observed in Figures 4.5 and 4.6, this approach leads to unsatisfactory results so that convergence of the numerical solution is highly influenced by the error of the Newton-Raphson solver.

Finally, we show that a standard Newton-Raphson solution strategy is insufficient to obtain a solution by showing an instance of loss of convergence in Newton-Raphson iterations. Figure 4.7a compares profiles of the residual errors obtained in the proposed TR-

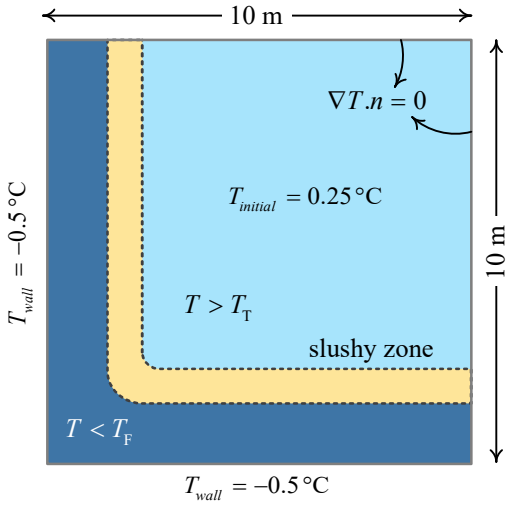

Figure 4.8 2-D problem domain configuration: geometry and boundary conditions

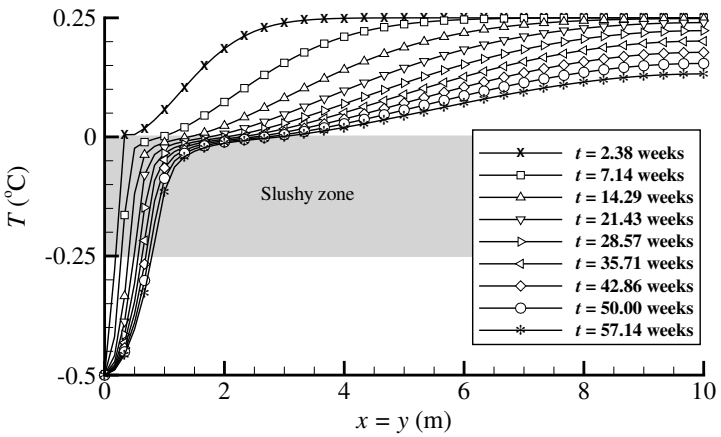

Figure 4.9 Diagonal temperature profile at different timesteps ($t = 7.14$ to $t = 57.14$ weeks)

FEM scheme, a standard Newton-Raphson scheme at $t = 900\,\text{sec}$. The Newton-Raphson scheme exhibits an oscillatory behaviour and fails to converge no matter how many iterations are carried out. On the other hand, the trust region algorithm always successfully achieved a solution within the pre-determined tolerance error. The trust region size is successively changed within the trust region iterations, as shown in Figure 4.7b, and a solution increment is only accepted if it leads to a satisfactory reduction in the objective functional as discussed in Section 4.5. We have also reported the convergence profile of an L-scheme solution strategy similar to the one proposed in (List and Radu, 2016) for the problem of Section 4.6.1. As explained in (List and Radu, 2016), the constant L in the L-scheme

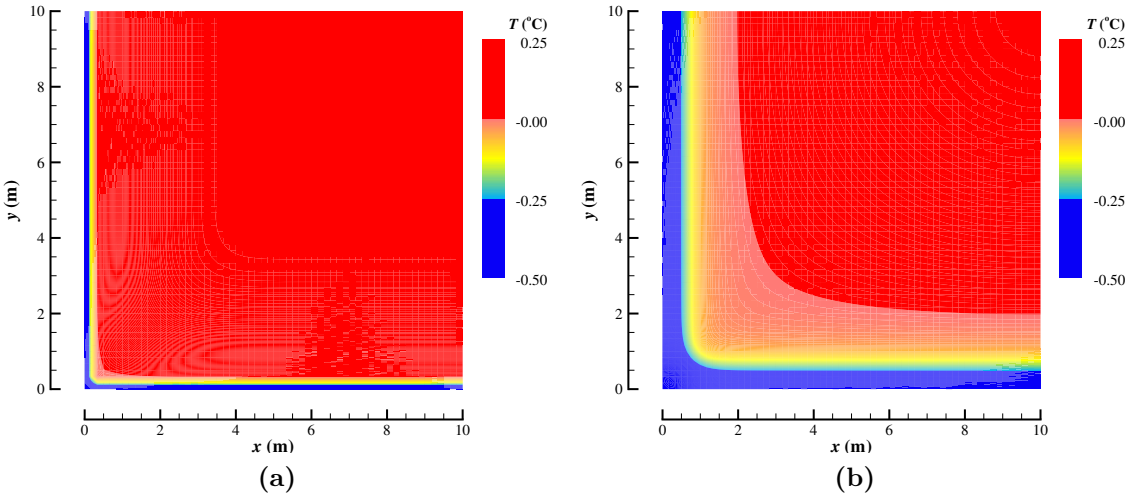

Figure 4.10 Temperature distribution contours: (a) FEM-TR algorithm at $t = 7.14$ weeks and (b) FEM-TR algorithm at $t = 57.14$ weeks

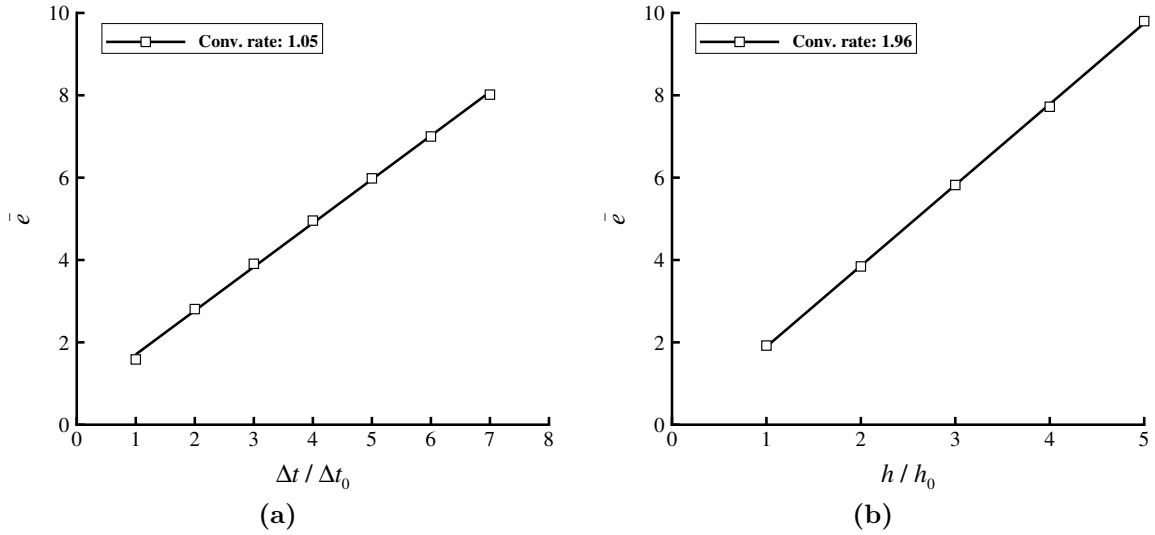

Figure 4.11 Calculated convergence rates for a corner freezing problem by varying sizes of (a) timestep, and (b) mesh

should satisfy $L \geq L_0$ where $L_0 = \sup_T |H'(T)|$. We used $L = 540$ in the present simulation by taking into account the above mentioned criterion. As is evident in Figure 4.7a, no oscillation is observed in the solution obtained by the L-scheme, however, the iteration fails to converge to the desired tolerance of ϵ_g within the the first 20 iterations are shown in Figure Figure 4.7a. In fact, the L-scheme took more than 350 iterations to converge to the same pre-determined tolerance in this case. Simulation of the problem using the FEM-TR algorithm took approximately 23 times shorter than the L-scheme iteration when using similar computer codes on the same machine.

4.6.2 Two-dimensional corner freezing block

To further examine the performance of the method in more complicated 2-D settings, a soil domain with a freezing corner is simulated in this example. As shown in Figure 4.8, a 10×10 m initially thawed domain is considered with left and bottom sides maintained at a temperature lower than the freezing temperature of the soil. The corner freezing problem with isothermal phase-change has been solved both analytically (Budhia and Kreith, 1973; Comini et al., 1974; Rathjen and Jiji, 1971) and numerically (Lazaridis, 1970; Chessa et al., 2002) using other numerical methods. Figure 4.9 shows the numerical temperature distribution along the diagonal of the domain at different instants of the simulation ($t = 7.14$ to $t = 57.14$ weeks), and Figure 4.12 illustrates the temperature history at different diag-

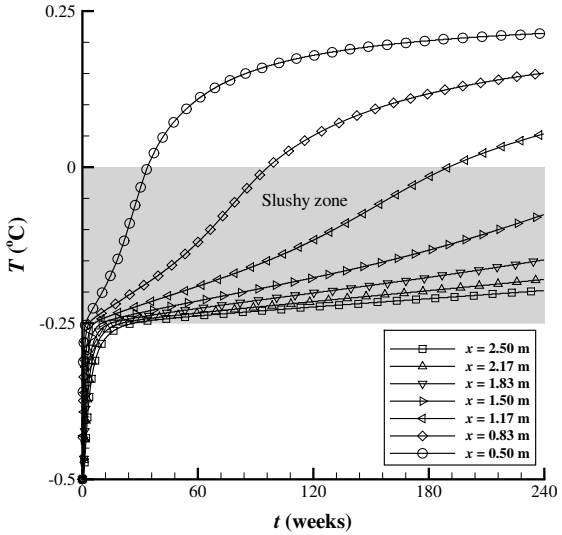

Figure 4.12 Diagonal temperature history profile

onal nodes. Furthermore, Figure 4.10 shows the temperature distribution at two different timesteps of the simulation. The proposed algorithm is based on a non-isothermal phase-change criterion for which no analytical solution is available in the literature to the authors' knowledge to perform a comparison. The mesh size and timestep sensitivity analyses shown in Figure 4.11, however, show a convergent behaviour indicative of the robustness of the numerical results.

4.7 Conclusion

In the present work, a finite element model was proposed for the simulation of heat transfer with a non-isothermal phase-change on the basis of an energy minimization strategy. The main goal of this model is to simulate permafrost processes or, in general, conductive heat transfer problems with non-isothermal first order phase transition, in which the release of latent heat occurs within a temperature range. The model is verified against an existing analytical solution for 1-D non-isothermal phase-change, indicating favourable accuracy. In addition, we showed that the method is capable of handling different regimes of phase transition by showing numerical results obtained for a narrow freezing temperature range (-0.05 to $0°C$) and making comparison with the Neumann solution available for the classical Stefan Problem. Several timestep and mesh size convergence studies was also presented in 1-D and 2-D in order to show the robustness of the finite element formulation and that the method is free of nonphysical timestep and grid size dependence. Based upon the con-

vergence rates for different SFCs, the numerical behavior of the exponential and sinusoidal SFCs are better than the linear SFC. The use of the trust region minimization algorithm is am essential ingredient of the proposed method. In particular, it was shown that standard and modified Newton's solution strategies fail to obtain a solution in many cases in our setting. Future efforts may be devoted to examine the efficiency of this model in coupled heat transfer-fluid flow problems involving advective heat transfer.

Chapter 5

Effect of heterogeneity on permafrost thaw

Statement of contribution

Part of the following chapter was presented and published at Cold Regions Engineering 2019 proceeding:

Amiri, E. A., and Craig, J. R. (2019). Effect of Soil Thermal Heterogeneity on Permafrost Evolution. Cold Regions Engineering 2019, 492–499.

The following chapter is prepared to be submitted to the journal Advances in Water Resources. The journal article would be co-authored by myself, Dr. James R. Craig (my supervisor), Dr. Juliane Mai, Research Assistant Professor in the Department of Civil and Environmental Engineering, Élise G. Devoie, PhD Candidate in the Department of Civil and Environmental Engineering. I developed and implemented the computer program written in C++; designed and ran the experimental and sensitivity analysis simulations; and wrote the major components of the manuscripts. Dr. Craig provided supervision over designing the experimental and sensitivity analyses, and editing the manuscript. Dr. Mai provided the idea of Sobol' sensitivity analysis; prepared the descriptions of the details of the Sobol' scheme; and ran the Sobol' analysis with the provided results of the sensitivity analysis simulations. Devoie significantly contributes to the field data collection at the Scotty Creek Research Station (SCRS); hence, she provided the field data and field related insights, and prepared the study site descriptions.

5.1 Introduction

Permafrost underlies nearly a quarter of the exposed land on Earth. The recent state of the global climate is causing permafrost degradation in several regions, including the discontinuous permafrost in the south of Northwest Territories (NWT), Canada (Quinton and Baltzer, 2013). Climate projections show a rapid increase in the mean annual temperature of the discontinuous permafrost zone of the NWT (Johannessen et al., 2004). Permafrost thaw has several effects including, but not limited to, the changes in surface and subsurface bodies that rely on groundwater exchange (Walvoord and Kurylyk, 2016); changes in the thermal, hydro-mechanical, and geo-mechanical properties of soil (Qi et al., 2006; Tang and Yan, 2014; Jamshidi et al., 2015); disturbance in the Earth's carbon balance via an increase in greenhouse gas (GHG) emissions due to an increase in microbial activities in the unthawed soil (Kurganova et al., 2007); and changes in the landscape of permafrost peat plateaus (Connon et al., 2014). During the last two decades, the permafrost body temperature in discontinuous permafrost regions such as the NWT has increased from -2°C (Dyke and Brooks, 2000) to just below 0 °C (Devoie et al., 2019; Environment and Natural resources - Northwest Territories, 2014); thus, a slight increase in the mean annual temperature can lead to an extreme degradation or complete disappearance of the permafrost. In addition to the mean climate forcing, heterogeneity in system properties and surface energies can also impact the local evolution of permafrost. The question addressed here, in part, is what is the significance of such local spatial variability? Recent efforts have been made focusing on uncertainties in representing the hydrological processes (Slater and Lawrence, 2013), in part, the thermal processes in the models (Koven et al., 2013).

Permafrost thaws occur in several modes. Jorgenson and Osterkamp (2005) categorized permafrost thaw modes based on permafrost distribution, thaw rates, ecological effects using hydrologic changes, soil types, and surface vegetation. It has been observed in the Scotty Creek Research Station (SCRS) that, in some regions, lateral permafrost thaw is more significant than the vertical degradation of permafrost. There has been little work done studying the important drivers of lateral permafrost thaw. Ling et al. (2012) studied the effect of thermokarst lakes (thaw lakes) on the formation of open taliks and lateral permafrost thaw, and showed that lakes with mean bottom temperature of greater than 0 °C act as heat sources with a positive feedback on talik formation. Kurylyk et al. (2016) investigated the influence of lateral and vertical permafrost thaw on landscape changes, and noted the importance of characterizing the lateral sources of energy in permafrost modeling. The body temperature of discontinuous permafrost is typically close to zero,

and its thickness is less than that of continuous permafrost (McClymont et al., 2013); thus, a slight change in the input energy may lead to dramatic thaws.

The typical purpose of permafrost modeling is to produce realistic short- and long-term projections of the state of permafrost. In this regard, multiple permafrost models have been developed with different levels of complexity, e.g. incorporating coupled processes and adding multidimensionality. The two-dimensional trust region model developed in Chapter 4 has demonstrated superior convergence and stability relative to alternative methods which makes it uniquely useful for testing over a wide range of conditions and for the evaluation of ensembles. The main objectives of this chapter are to validate the developed permafrost model, which has been verified against the analytical solution in Section 4.6, with field data; to study the effect of heterogeneity on permafrost body evolution through sensitivity analyses; and to investigate the effect of the presence of hydrologic features and the resultant advective heat transfer on lateral permafrost thaw.

5.1.1 Study area

The SCRS is located in the southern NWT, approximately 50 km south of Fort Simpson. This research station is situated in an ecosystem-protected peatland dominated by discontinuous permafrost, which is actively degrading due to increases in the mean annual temperature and changes to precipitation regimes (Quinton et al., 2018). This site was chosen for this study focusing on heterogeneity because the landscape is made up of a mosaic of differing land cover types, whose interfaces (and evolution) are dependent, in part, on subsurface heterogeneity. The peat deposits in the study site range from 2 m to 8 m in depth, overlaying low-permeability glacial till (Quinton et al., 2018). The dominant land-cover types in the study area include fens, which act as low-gradient hydrological routing features; collapse scar bogs, which mainly act as storage features; and peat plateaus (Quinton et al., 2009). The peat plateaus are elevated above the surrounding wetland features due to the presence of segregated ground ice, allowing the high-permeability peat to drain to the surrounding wetland features and resulting in a relatively dry vadose zone which is capable of supporting a black spruce canopy unlike the surrounding wetland features (Quinton et al., 2009). Given the current degradation of the permafrost, the peat plateaus in this landscape often include taliks which may be isolated, or may become connected to each other and adjacent wetland features (Connon et al., 2018). Movement of water through these features is thought to be a driver of preferential thaw in the landscape, which may help explain variability in permafrost degradation rates (Connon et al., 2014). This

is supported by observations of peat plateaus adjacent to wetland features that degrade more quickly (both vertically and laterally) than plateaus with isolated taliks (McClymont et al., 2013; Baltzer et al., 2014).

The field data used to describe the boundary conditions of the model were collected at ten sites across the SCRS, capturing the variability in surface temperature across landcover types. Data was collected using Onset HOBO U12 4-channel thermistors as well as Decagon Em50 5-channel thermistors and loggers. Vertical temperature profiles extended to an average depth of 80 cm below the soil surface, with sensor spacing between 10 and 20 cm, depending on location. It should be noted that the data was collected by the Scotty Creek research group at Wilfrid Laurier University.

5.2 Methodology

5.2.1 Heterogeneous field realization

To investigate the effect of heterogeneity on permafrost thaw patterns, realistic realizations of heterogeneous media respecting the specified geostatistical correlation structure are required. Here, geostatistical software library (GSLIB) is deployed to generate spatially correlated soil realizations using a sequential Gaussian approach (Section 2.4). In this process, a realization of spatially correlated heterogeneous field is generated from the specified semivariogram. Then, the heterogeneous soil property fields (density, thermal conductivity, and hydraulic conductivity) are calculated using the generated perturbation coefficient field. The mathematical procedure of this perturbation process is as follows:

$$\Psi\left(\mu_p,\, \Xi\left(x,\, z\right),\, \sigma_p\right) = \mu_p + \Xi\left(x,\, z\right)\sigma_p, \tag{5.1}$$

where μ_p, $\Xi\left(x,\, z\right)$, and σ_p are the homogeneous property (mean value), perturbation coefficient, and standard deviation of the property, respectively. The calculated field is then truncated (if necessary) using the feasible ranges of the properties reported in the literature to avoid the unrealistic values.

5.2.2 Surface spatial variability

Due to the surface spatial variability (e.g. vegetation, topography, and snow pack) in permafrost complex, the input surface energy and surface temperature will consequently be

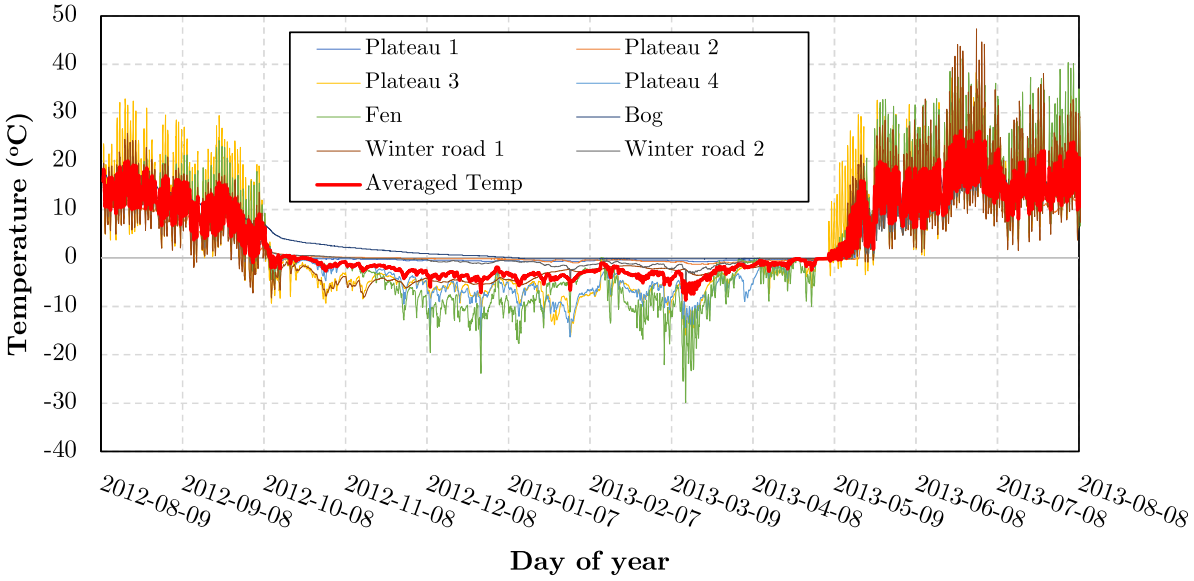

(a)

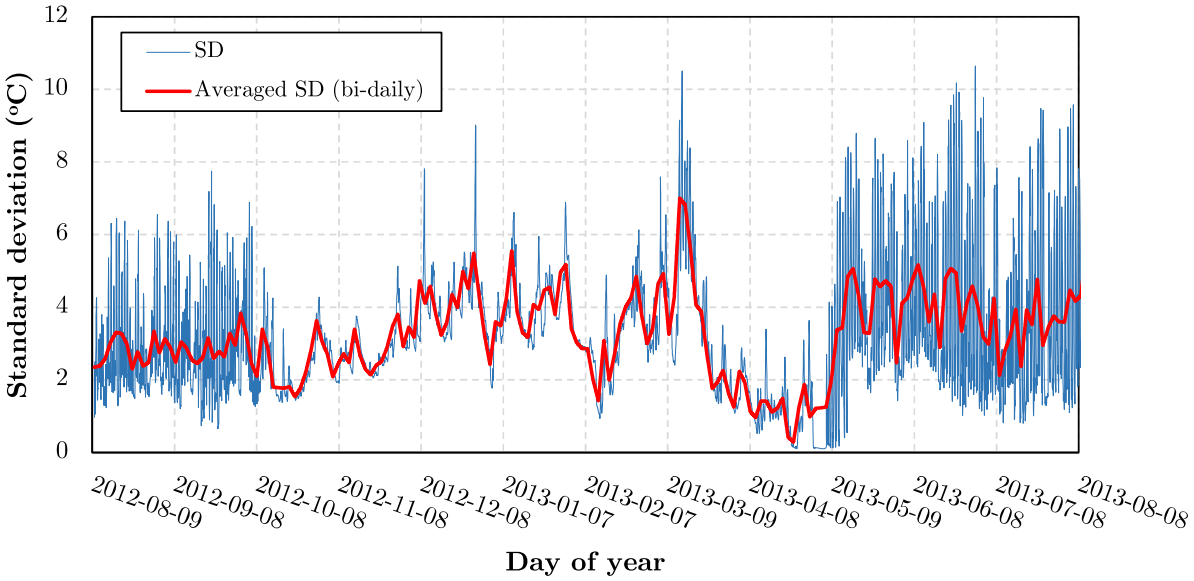

(b)

Figure 5.1 Process of generating a time-dependent standard deviation of boundary condition: (a) temperature profiles collected at difference locations at the same time of the year (b) standard deviation of the temperatures

heterogeneous. One way to represent would be to apply detailed soil-vegatation-atmosphere (SVAT) model with variable leaf area index (LAI), evapotranspiration (ET), etc. However, this type representation requires extensive data and a complicated coupled modeling.

Alternately, to precisely characterize the spatial variability in surface input energy and generate a realistic semivariogram, extensive metadata collection is required, including temperature collection at a multiple depths at a large number of different locations of a research site for a long period. To the best of the author's knowledge, such data does not exist at SCRS, or not easily accessible. To circumvent the limited data, the correlation length for surface is assumed variable (1 to 5 m based on visual inspection of landscape). It should be noted that using "naïve" procedures for applying a shift in temperature time-series (e.g. using additive or multiplicative factors) leads to unrealistic modifications such as shifting the zero-curtain temperature range and period; thus, here, the time-dependent spatial standard deviation of temperature is estimated using the temperatures collected from nine different locations at the depth of 10 cm at the same time of the year (Figure 5.1a). Then, the standard deviation of the temperatures is calculated (Figure 5.1b)

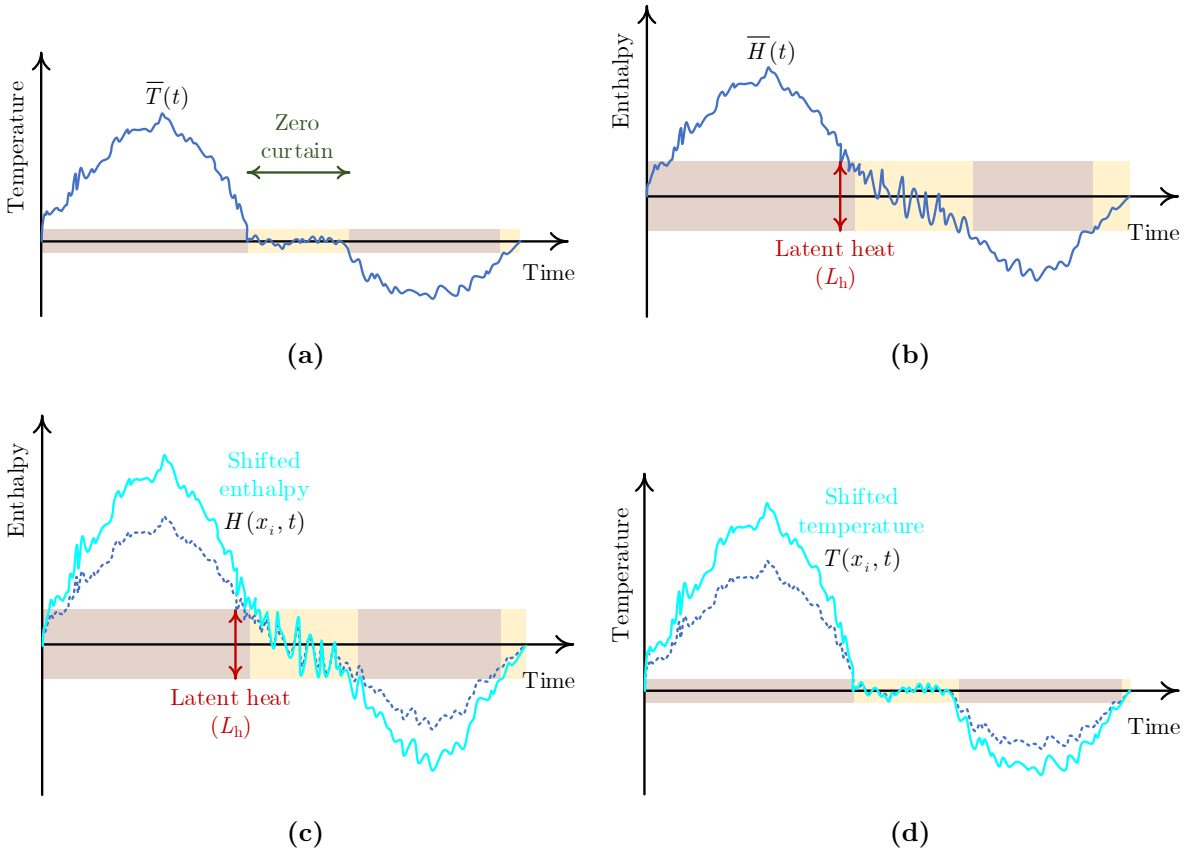

Figure 5.2 Temperature boundary condition correction procedure at point x: (a) mean temperature boundary condition profile (b) mapping temperature profile to enthalpy domain (c) applying the correction to the enthalpy (d) mapping the shifted enthalpy profile back to temperature domain

and smoothed (Figure 5.1b) for a better behavior in the numerical model. To determine a plausible surface boundary temperature distribution in space and time, a one-dimensional spatially correlated field with a sill value of 1.0 and mean of 0 is generated. Correcting the temperature boundary condition using the generated field is challenging. Because the zero-curtain effect must be preserved, neither a multiplicative or additive factor can therefore be used to examine future plausible surface conditions. This issue arises due to the use of temperature boundary condition rather than an input energy flux. One solution would be to simulate the snowpack, vegetation, etc., coupled to two-dimensional model. This solution requires an extremely complicated coupling and with several field-informed inputs, which was here deemed infeasible. The proposed solution includes calculating the enthalpy profile, applying a shift in the enghalpy using the field-informed standard deviation and spatially correlated perturbation coefficients, and mapping the enthalpy profile back to the temperature domain. The schematic of this procedure is illustrated in Figure 5.2. The mathematical implementation of the procedure is as follows:

The correction subroutine is presented as

$$\bar{T_{\mathrm{c}}} = \Phi\left(x,\, t,\, \sigma_T\left(t\right),\, \bar{T},\, L_{\mathrm{h}},\, \overline{\rho c},\, \xi,\, S_{\mathrm{w}},\right), \tag{5.2}$$

in which $\bar{T_{\mathrm{c}}}$ is the corrected surface temperature, x is the horizontal location of the boundary, t is time, $\sigma_T\left(t\right)$ is the time dependent standard deviation, $\bar{T}$ is the mean surface temperature, and L_{h} is the latent heat of fusion. Also, $\overline{\rho c}$, ξ, and S_{w} are the soil bulk heat capacity, perturbation coefficient, and water saturation at x, respectively. The steps in this subroutine are:

1. Convert the mean temperature ($\bar{T}$) to mean enthalpy by assuming a buffer zone for capturing the zero-curtain effect (here, -0.5 to $+0.5\,^{\circ}\mathrm{C}$):

$$\bar{H}\left(\bar{T}\right) = \overline{\rho c}\bar{T} + S_{\mathrm{w}}L_{\mathrm{h}}, \tag{5.3}$$

2. Apply the correction to the enthalpy, corresponding to a shift in total energy content of surface:

$$H_{\mathrm{c}} = \bar{H}\left(\bar{T}\right) + \overline{\rho c}\sigma_T\left(t\right)\xi, \tag{5.4}$$

3. Return to the temperature domain by converting the corrected enthalpy to temper-

ature using the inverse of Equation 5.4:

$$T_{\mathrm{c}} = \bar{H}^{-1}\left(H_{\mathrm{c}}\right). \tag{5.5}$$

The results and discussions of investigating the effect of surface spatial temperature variability will be provided in Section 5.3.2

5.2.3 Sensitivity analysis using Sobol' scheme

A global sensitivity analysis was performed in order to identify the most sensitive parameters of the permafrost model. The method employed here is the Sobol' sensitivity method (Saltelli and Sobol', 1995). The Sobol' method is a variance-based sensitivity analysis deriving sensitivities of inputs (i.e. model parameters) based on estimates of the variance of target variables (i.e. model outputs) that is caused by perturbing the inputs. The Sobol' sensitivity indices derived using this method are traditionally the main and the total Sobol' sensitivity indices. The first describes the impact of the perturbation of a single parameter on the model output while the latter includes interactions of this parameter with other model parameters. Both Sobol' indices (main and total) are normalized with respect to the overall model variability that can be achieved when all parameters are randomly perturbed. Hence, the main effect is bound between zero and one, where a zero sensitivity indicates a parameter that is not sensitive at all, and a sensitivity of one indicates to a parameter that is responsible for all changes in the model outputs. The total effect only has a lower bound of zero. The upper bound can be greater than one due to parameter interactions. The difference between the total and main effect of a parameter indicates the magnitude of interactions between this parameter and any other parameter or group of parameters. Although the theory behind the Sobol' method is still the one introduced by Saltelli and Sobol' (1995), there are plenty of implementations available due to the necessary approximation of the variances in the model outputs. Several of these methods are compared by Saltelli et al. (2010). Cuntz et al. (2015) evaluated all these methods and identified one set of implementations for the main and total effect that converges comparably faster for insensitive parameters (see Appendix D in Cuntz et al., 2015). This set of implementations has been used in several studies thereafter (Cuntz et al., 2016; Mai and Tolson, 2019).

The Sobol' sensitivity analysis is based on only model outputs. This is in contrast to other sensitivity methods, so called derivative-based methods, that may also require the

parameter sets that were used to derive these model outputs. The Sobol' method, similar to any other variance-based methods, only requires parameter sets that are uniformly sampled covering the full parameter space. To achieve a uniform and most efficient sampling of the high-dimensional parameter space, a stratified sampling method is commonly used (Campolongo et al., 2007; Saltelli, 2002; Saltelli et al., 2008). In this work, the method of Sobol' sequences was used (Sobol, 1976). Note that it is only by coincidence that the sampling and the sensitivity methods are based on Sobol'. Technically, any stratified sampling method (e.g. Latin Hypercube sampling) could be coupled with the Sobol' sensitivity method.

The model outputs analyzed in the Sobol' analysis were total permafrost and talik areas, in consideration of the model parameters: correlation length, freezing point standard deviation, and density standard deviation. Information about the fixed model parameters are given in Table 5.2 with the ranges of parameters in Table 5.4. The table contains information on the uniform ranges from which the model parameters are sampled using the stratified sampling of Sobol' sequences. In total $K = 1000$ Sobol' sequences have been used. The budget of a Sobol' analysis deriving main and total effects for N model parameters is $(N + 2) \times K$; therefore, 5,000 simulations were run. Each simulation took almost 2 hours on Sharcnet system; thus, a set of 500 parallel simulations were configured (i.e. each parallel simulation consists of 10 simulations in a row). This budget calculation is independent of the implementation but may require more parameter sets, K, to obtain convergence of sensitivity estimates for insensitive parameters.

The results of the Sobol' sensitivity analysis will be provided and discussed in Section 5.3.1.

5.3 Validation and numerical results

The results obtained by the model developed for this research are validated against the field data collected at the SCRS in the NWT. The simulation designed for validation is based upon the measured temperatures at different depths of the active layer of a nearly saturated peat plateau. The simulated temperatures at two different depths ($z = 35$ cm and $z = 65$ cm) are compared with the the temperatures measured at the same depths of the plateau (Figure 5.3). The validation period is 15 years (starting on August 20^{th}, 2001 at $22 : 00 : 00$ and ending on August 20^{th}, 2016 at $21 : 30 : 00$). The soil properties and numerical solution parameters are listed in Table 5.1. The initial condition was calculated

Table 5.1 Properties used in the simulations with heterogeneous boundary condition

Parameters	Values	Parameters	Values
K_s $[\mathrm{W.m^{-1}.K^{-1}}]$	0.1	K_i $[\mathrm{W.m^{-1}.K^{-1}}]$	2.14
c_s $[\mathrm{J.kg^{-1}.K^{-1}}]$	630	c_i $[\mathrm{J.kg^{-1}.K^{-1}}]$	2108
ρ_s $[\mathrm{kg.m^{-3}}]$	250	ρ_i $[\mathrm{kg.m^{-3}}]$	920
n (porosity)	0.8	L_{heat} $[\mathrm{J.kg^{-1}}]$	334000
S_w^{res}	18%	Δt [s]	1600
K_w $[\mathrm{W.m^{-1}.K^{-1}}]$	0.58	ϵ_π	1.0E–4
c_w $[\mathrm{J.kg^{-1}.K^{-1}}]$	4187	ϵ_g	1.0E–3
ρ_w $[\mathrm{kg.m^{-3}}]$	1000		

by fitting a curve to the temperature profile vs. depth using piecewise cubic Hermite interpolating polynomial (PCHIP).

The simulated and measured temperature profiles are shown in Figure 5.4. The mean absolute error (MAE) and standard error (SE) at $z = 35$ cm are 0.68 °C and 0.0011 °C, and at $z = 65$ cm are 0.78 °C and 0.0022 °C, respectively. It should be noted that the results were obtained without calibrating the model properties. As is evident in Figure 5.4, the simulated temperature profiles are in an acceptable agreement with the measured temperature profile during the 15-year simulation period. Particularly, the model captures the active layer refreeze during the winter periods, which is not as successfully captured by

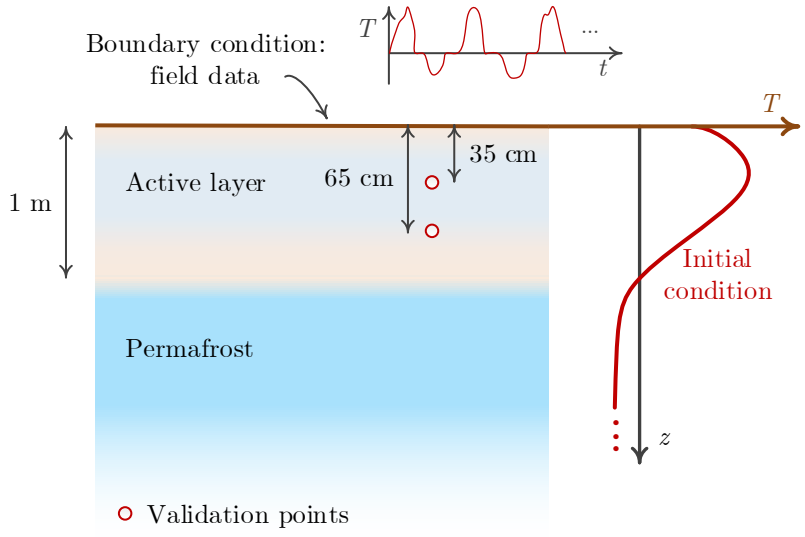

Figure 5.3 Schematics of the experimental simulation

popular models such as the FEFLOW used by Langford et al. (2019) and NEST (Zhang et al., 2003) used by Kurylyk et al. (2016). It should be noted that the forcing functions used by Langford et al. (2019) and Kurylyk et al. (2016) are derived using a coupled model (e.g. SHAW model), which is more complex than a temperature forcing function and may explain some of this deficit in performance. The validation period for the model developed in this research is 15 years, which is relatively longer than common validation periods in the literature (one to six years).

5.3.1 Sensitivity analyses

To study the effect of soil heterogeneity on permafrost thaw rates, a set of sensitivity analyses is carried out. The results are analyzed using Sobol' sensitivity analysis scheme (Section 5.2.3). An initially fully frozen two-dimensional domain (50 m in length and 5 m in depth) is considered for each simulation. The domain is subjected to the 15-year field

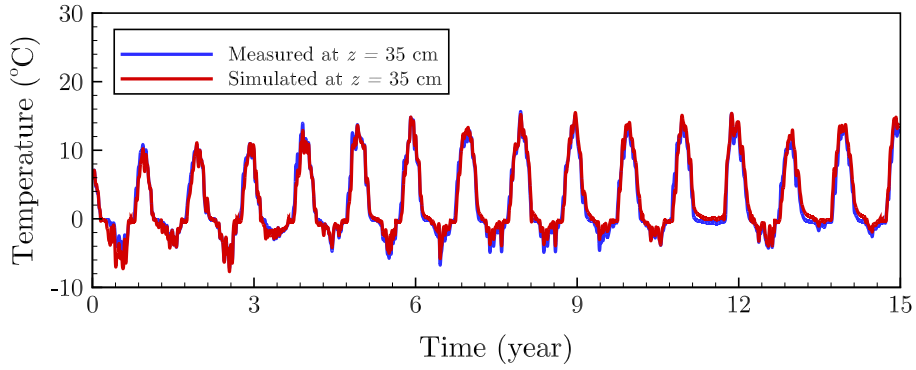

(a)

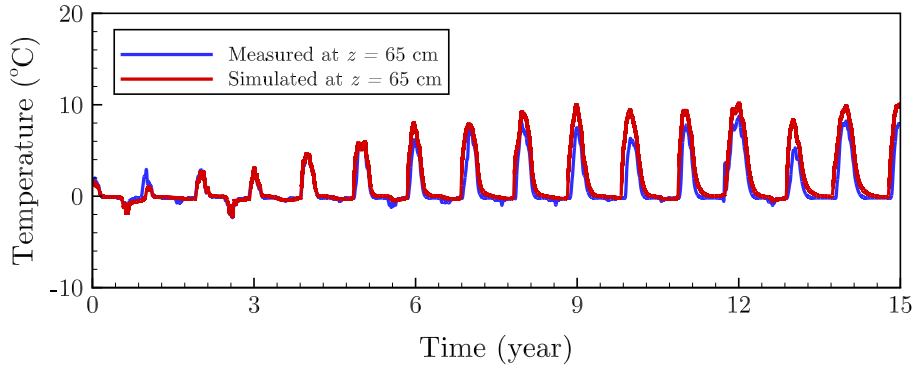

(b)

Figure 5.4 Simulated vs. measured temperature profiles: (a) at depth = 35 cm (b) at dept = 65 cm

Table 5.2 Constant properties used in the simulations

Parameters	Values	Parameters	Values
K_{w} $\left[\mathrm{W.m^{-1}.K^{-1}}\right]$	0.58	K_{i} $\left[\mathrm{W.m^{-1}.K^{-1}}\right]$	2.14
c_{w} $\left[\mathrm{J.kg^{-1}.K^{-1}}\right]$	4187	c_{i} $\left[\mathrm{J.kg^{-1}.K^{-1}}\right]$	2108
ρ_{w} $\left[\mathrm{kg.m^{-3}}\right]$	1000	ρ_{i} $\left[\mathrm{kg.m^{-3}}\right]$	920
Δt [s]	3600	L_{heat} $\left[\mathrm{J.kg^{-1}}\right]$	334000
ϵ_{π}	1.0E–4	ϵ_{g}	1.0E–3

collected temperature (starting on August 20, 2001 at 22:00:00 and ending on August 20, 2016 at 21:30:00) along the top boundary and allowed to cyclically thaw. At the end of each simulation, the total permafrost and talik areas are calculated as the diagnostic functions of the sensitivity analysis. The variable properties in each simulation are the heterogeneity correlation length and standard deviations of soil density and freezing point. The mean values of soil density and freezing point are 385 $\left[\mathrm{kg.m^{-3}}\right]$ and -0.75 [°C], respectively. The heterogeneous properties are generated using GSLIB. It should be noted that the thermal conductivity (K_{s}) and hydraulic conductivity (λ_{s}) of soil become heterogeneous as a by-product of the heterogeneity of soil density using the following pedotransfer functions:

$$K = \frac{0.135\rho_{\mathrm{s}} + 64.7}{2700 - 0.947\rho_{\mathrm{s}}}, \tag{5.6}$$

$$\log_{10}(\lambda) = 3.491 - 15.802\rho_{\mathrm{s}} + 19.552\rho_{\mathrm{s}}^2. \tag{5.7}$$

The summary of the parameters and cut-off ranges used in the sensitivity analysis is listed in Tables 5.2 and 5.3. After running Sobol' analysis, the main (S) and total (S_{T}) Sobol' sensitivity indices at the end of the simulation are calculated as follows:

The Sobol' sensitivity indices of permafrost evolution and talik formation during the last 10 years of simulation are depicted in Figures 5.6 and 5.7, which indicate a stable

Table 5.3 Heterogeneous soil properties used in the experimental analyses

Type	λ_{s} $\left[\mathrm{m.s^{-1}}\right]$	K_{s} $\left[\mathrm{W.m^{-1}.K^{-1}}\right]$	c_{s} $\left[\mathrm{J.kg^{-1}.K^{-1}}\right]$	ρ_{s} $\left[\mathrm{kg.m^{-3}}\right]$	n [–]	$S_{\mathrm{w}}^{\mathrm{res}}$ [–]
Peat	$\left[10^{-3}, 10^{-6}\right]$	[0.025, 0.1]	630	[10, 760]	0.8	0.18
Silty clay	$\left[10^{-5}, 10^{-10}\right]$	[0.4, 2.5]	1381	[700, 1300]	0.5	0.18
Fen	10^{-3}	0.25	400	200	0.95	0

Table 5.4 Main and total Sobol' sensitivity indices at the end of the simulation

Parameter	[min, max]	Permafrost area		Talik area	
		S	S_{T}	S	S_{T}
Correlation length [m]	[1, 12]	0.230	0.247	0.867	0.886
Freezing point SD* [°C]	[0, 0.5]	0.755	0.764	0.0	0.071
Soil dry density SD* $\left[\mathrm{kg.m}^{-3}\right]$	[0, 375]	0.005	0.004	0.105	0.110

*standard deviation

sensitivity analysis with almost no seasonal effect. The Sobol' sensitivity analysis results suggest that the total area of permafrost is most sensitive to the relatively narrow range of soil freezing point, and the total area of talik is most sensitive to the heterogeneity correlation length. An interpretation of the negligible sensitivity of freezing point ($S \simeq 0$) on the talik formations is that the depth of active layer can increase due to permafrost thaw, and talik area simply shifts down. It is interesting that the analyses indicate that soil density (and therefore porosity and thermal conductivity) has minimal effect on both model outputs; thus, it is inferred that the common homogeneity assumption for soil diffusivity may be realistic in the permafrost simulation area (at least when in-plane advective heat transfer is neglected). The distribution of the permafrost and talik areas at the end of the 5,000 simulations are plotted in Figure 5.5. No clear interdependecies between the

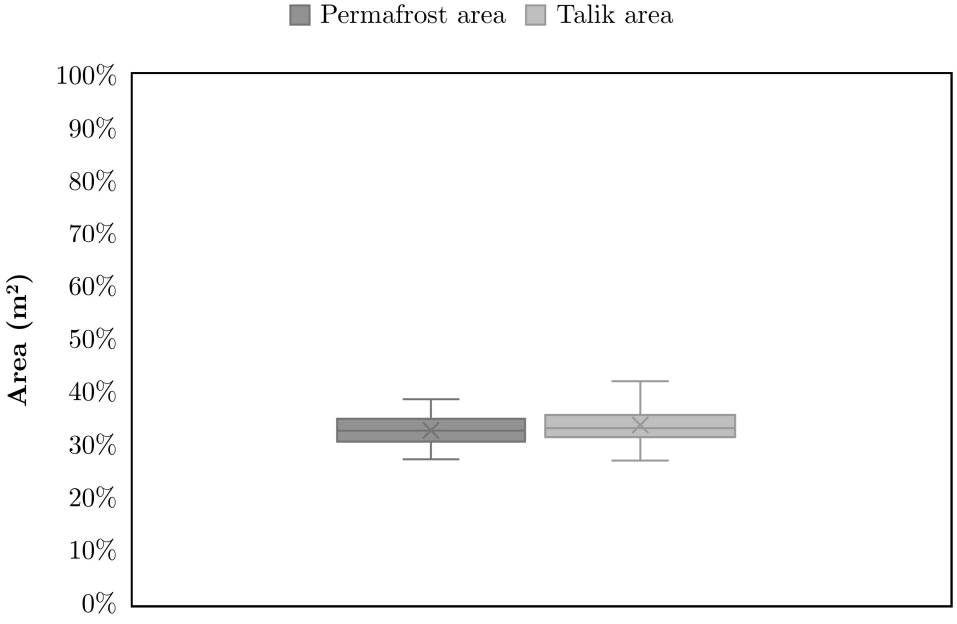

Figure 5.5 Permafrost and talik area distributions in the sensitivity analysis

parameters are evident since the main and total Sobol' indices are similar.

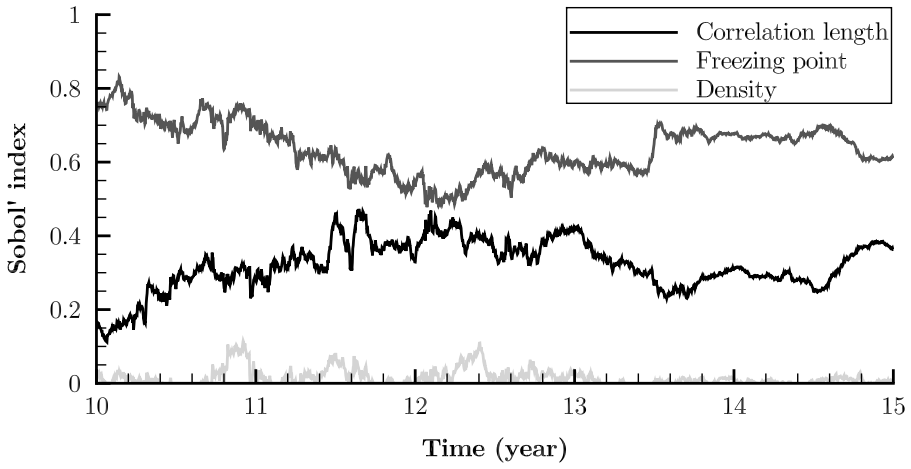

(a)

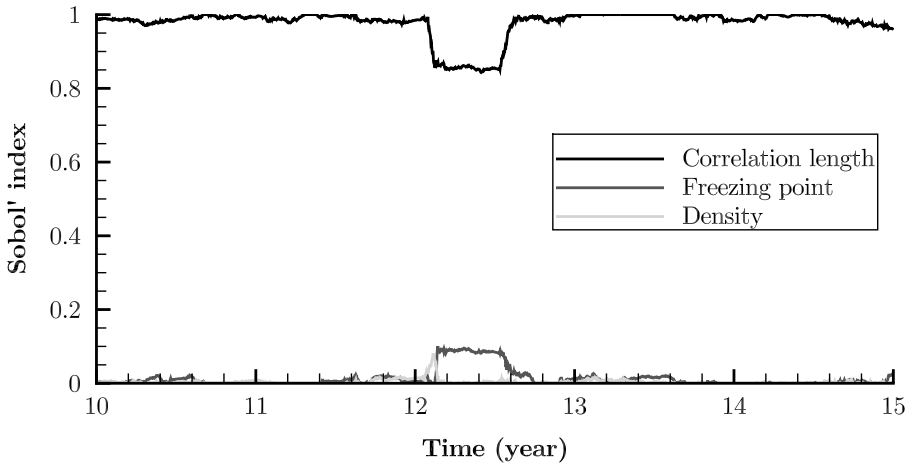

(b)

Figure 5.6 Sobol' analysis indices: (a) sensitivity of permafrost (b) sensitivity of talik

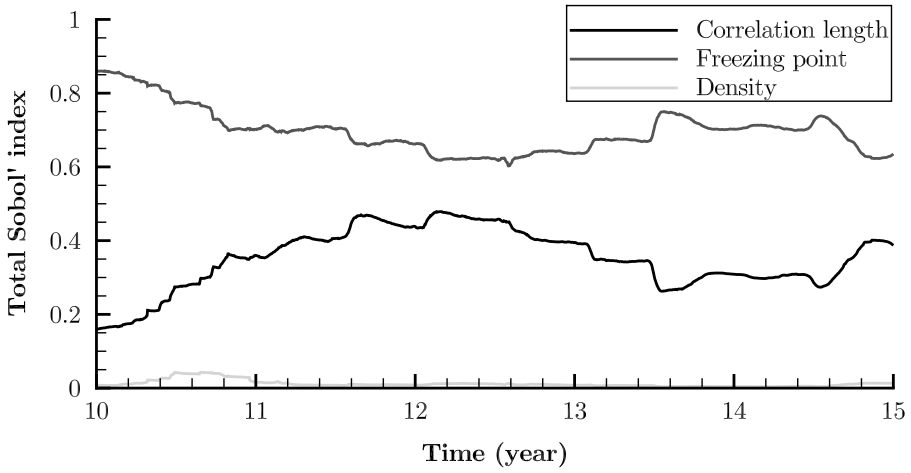

(a)

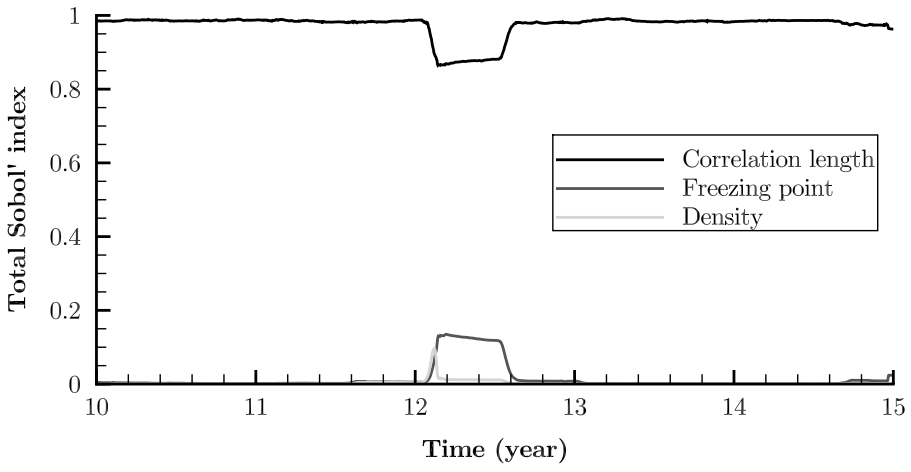

(b)

Figure 5.7 Total Sobol' analysis indices: (a) sensitivity of permafrost (b) sensitivity of talik

5.3.2 Effect of surface input energy spatial variability on permafrost thaw patterns

The surface input energy of a permafrost complex varies due to spatial variability of the vegetation, land cover, snowpack, presence of adjacent hydrologic features, etc. The procedure of accounting for these variabilities is elaborated on in Section 5.2.2; In this simulation, a $50\,\mathrm{m} \times 5\,\mathrm{m}$ heterogeneous domain is considered, and a uniform initial condition of $-2.1\,^{\circ}\mathrm{C}$ (fully frozen) is assumed. The surface boundary is subjected to a 10-year spatially heterogeneous surface boundary condition derived from the mean and standard deviation of 8 different locations at SCRS at 10 cm depth (Figure 5.1). The simulations are repeated for 5 different boundary condition correlation lengths ($\alpha = 1\,\mathrm{m}$, $2\,\mathrm{m}$, $3\,\mathrm{m}$, $4\,\mathrm{m}$, and $5\,\mathrm{m}$). The boundary condition perturbation coefficients along the surface boundary for different correlation lengths are plotted in Figures 5.8 to 5.12 (for a sample realization). The domain's spatial heterogeneity perturbation coefficients and resultant heterogeneous soil property fields for the same sample realization are illustrated in Figures 5.13 to 5.15. The distribution of the mean and standard deviation of the boundary condition perturbation coefficients are showed in Figure 5.13, which confirms acceptable values for the mean (almost zero) and the standard deviation (almost 1.0) for the perturbation coefficients of 50 realizations. It should be noted that tolerances for the mean and standard deviation are expected since the perturbation coefficients are randomly generated based on a theoretical semivariogram with a nugget value zero and sill value of 1.0 (details are presented in Section 2.4).

A comparison between the water saturation profile of a sample realization and that of the simulation with homogeneous boundary condition is depicted in Figure 5.15. As is evident, in the absence of any form of advective heat transfer, the heterogeneous surface boundary condition can lead to formation of a highly variable permafrost depth profile, which may become preferential water pathways. The normalized ice saturation ($\bar{S}_{\mathrm{ice}}$) is presented by the spatial integration (vertically and horizontally) of the ice saturation field in Figure 5.16. The normalized horizontal and vertical ice saturation are calculated as follows:

$$\bar{S}_{\mathrm{ice}}(z) = \frac{1}{W}\int_0^W S_{\mathrm{ice}}(x,\, z)\, dx, \tag{5.8}$$

$$\bar{S}_{\mathrm{ice}}(x) = \frac{1}{D}\int_0^D S_{\mathrm{ice}}(x,\, z)\, dz, \tag{5.9}$$

where W and D are the width and depth of the domain. Figure 5.16 shows the similarity between the average of the results of 50 heterogeneous boundary condition realizations and the result of the homogeneous boundary condition simulation. The formation of confined taliks is evident in Figure 5.15c. The distribution of permafrost and talik areas for the 50 heterogeneous boundary condition simulations at the end of year 10 are plotted in Figure 5.17. Although the mean of the boundary condition perturbation coefficients for each realization is almost zero (Figure 5.13a), a relatively wide range of permafrost depletion and talik formation is evident, which depicts how spatial variability in the input energy influences permafrost thaw patterns. The quartiles of the permafrost evolution and talik formations during the solution time for the simulation set using $\alpha = 3$ m is plotted in Figure 5.18.

The boundary condition variability factor, τ [°C], is presented here to quantify the effect of boundary condition spatial variability on permafrost evolution, which can be a representation of the level of land surface patchiness. τ is defined as the temporal mean of the standard deviations of the surface temperature from the mean surface temperature and is expressed as follows:

$$\tau = \frac{1}{N}\sum_{t=0}^{N}\sqrt{\frac{1}{X-1}\sum_{i=1}^{X}\left(T_{\mathrm{c}}\left(x_i,t\right)-\bar{T}\left(t\right)\right)^2}, \tag{5.10}$$

in which T_{C} is corrected surface temperature, $\bar{T}$ is mean temperature, X is the number of surface boundary nodes, N is the number of timesteps. Larger τ value represents higher spatial variability in the boundary condition.

The scatter plot of permafrost area vs. τ for different realizations and correlation lengths is depicted in Figure 5.19. Fitting a linear trendline to the data grouped by each correlation length reveals an notable pattern. As the correlation length increases, the sensitivity to the value of τ increases as well. At a constant τ value, the total area of remaining permafrost is higher for the simulations with a larger correlation length. Moreover, for a constant correlation length, the total area of remaining permafrost increases in the realizations with larger τ values. It can be interpreted that the τ coefficient is statistically significant due to its correlation with remaining permafrost area. The combination of τ coefficient and the correlation length of surface spatial heterogeneity may be used in projecting the patterns of permafrost thaw.

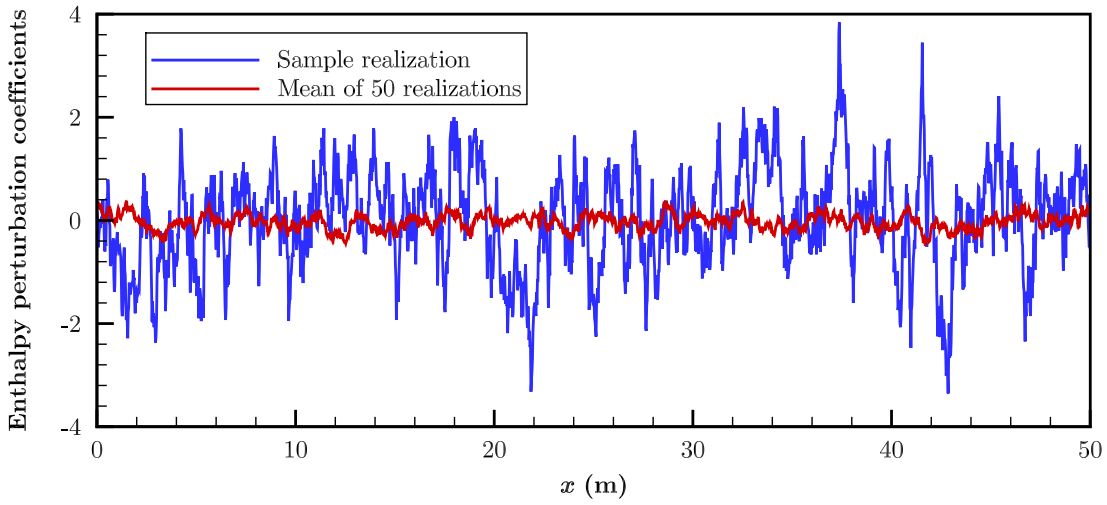

Figure 5.8 BC perturbation coefficients for a realization generated with GSLIB (correlation length - $\alpha = 1$ m)

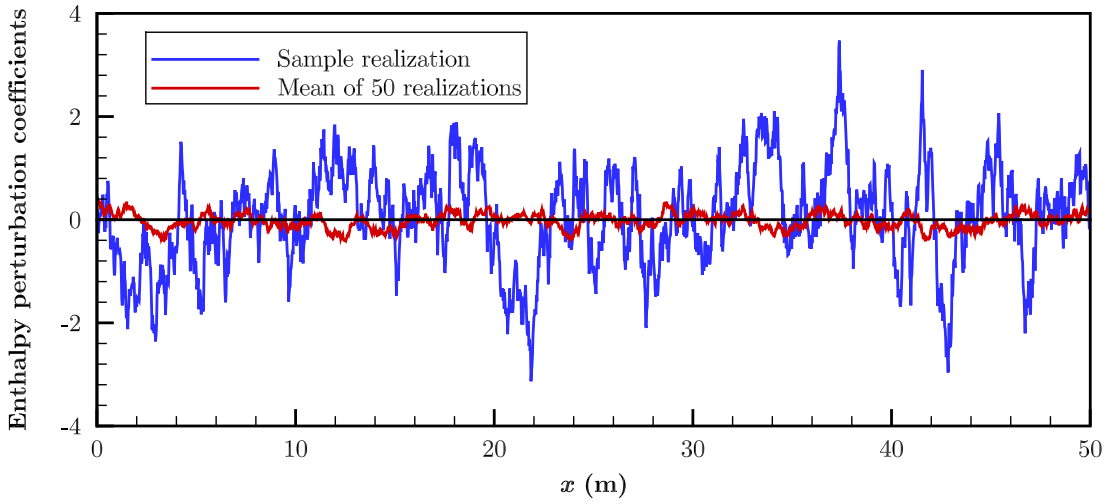

Figure 5.9 BC perturbation coefficients for a realization generated with GSLIB (correlation length - $\alpha = 2$ m)

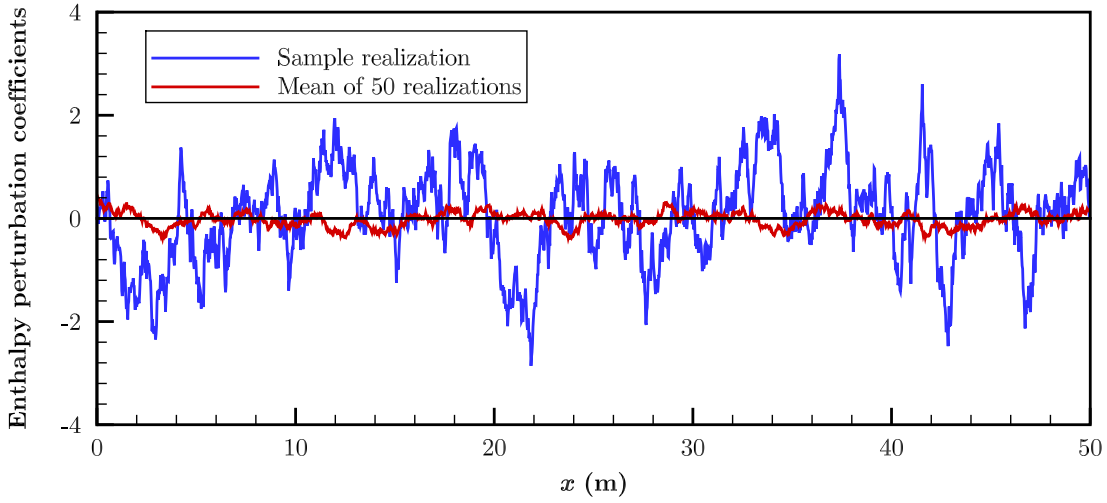

Figure 5.10 BC perturbation coefficients for a realization generated with GSLIB (correlation length - $\alpha = 3$ m)

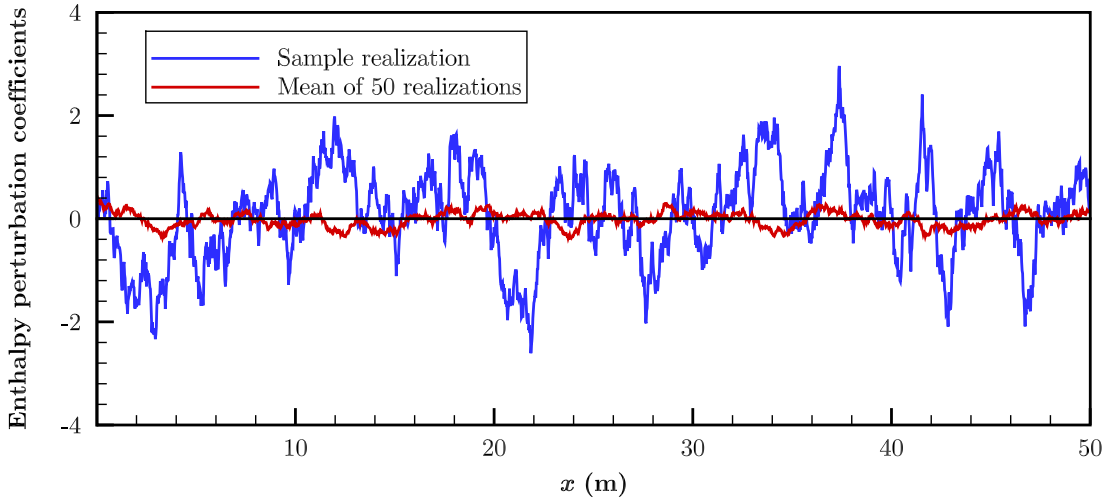

Figure 5.11 BC perturbation coefficients for a realization generated with GSLIB (correlation length - $\alpha = 4$ m)

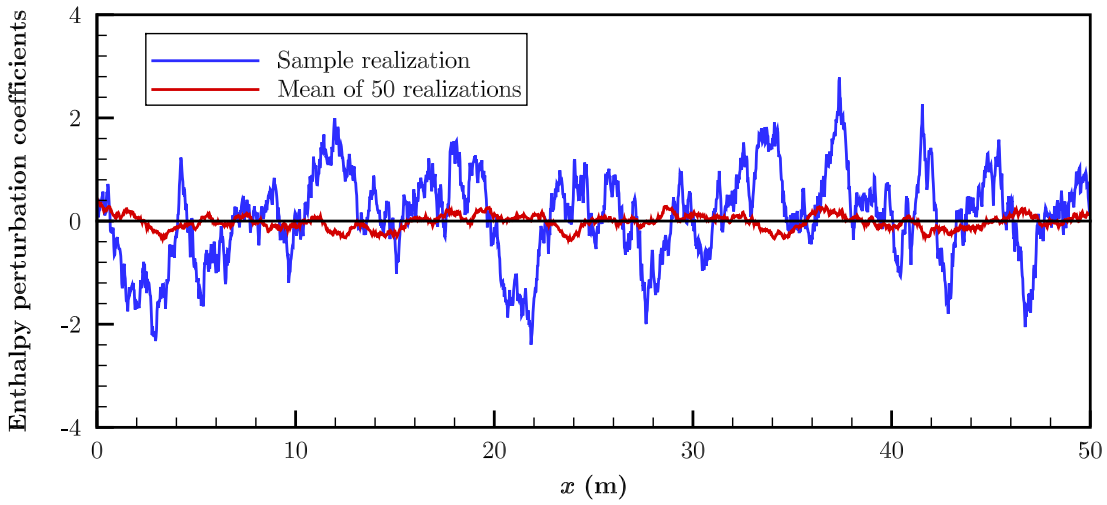

Figure 5.12 BC perturbation coefficients for a realization generated with GSLIB (correlation length - $\alpha = 5$ m)

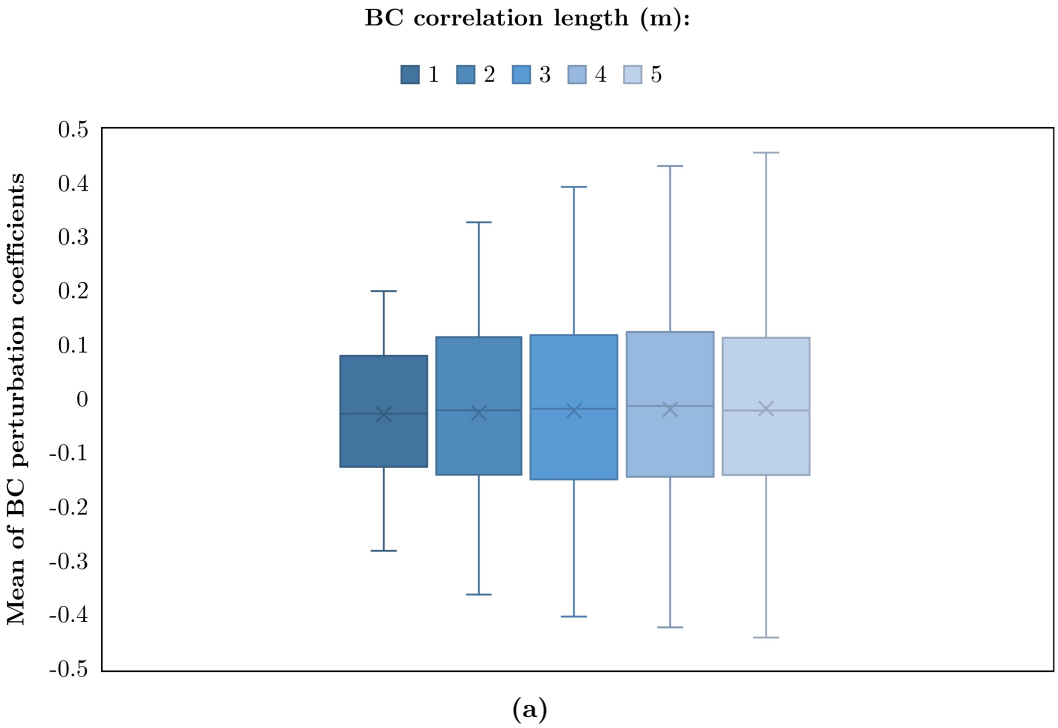

(a)

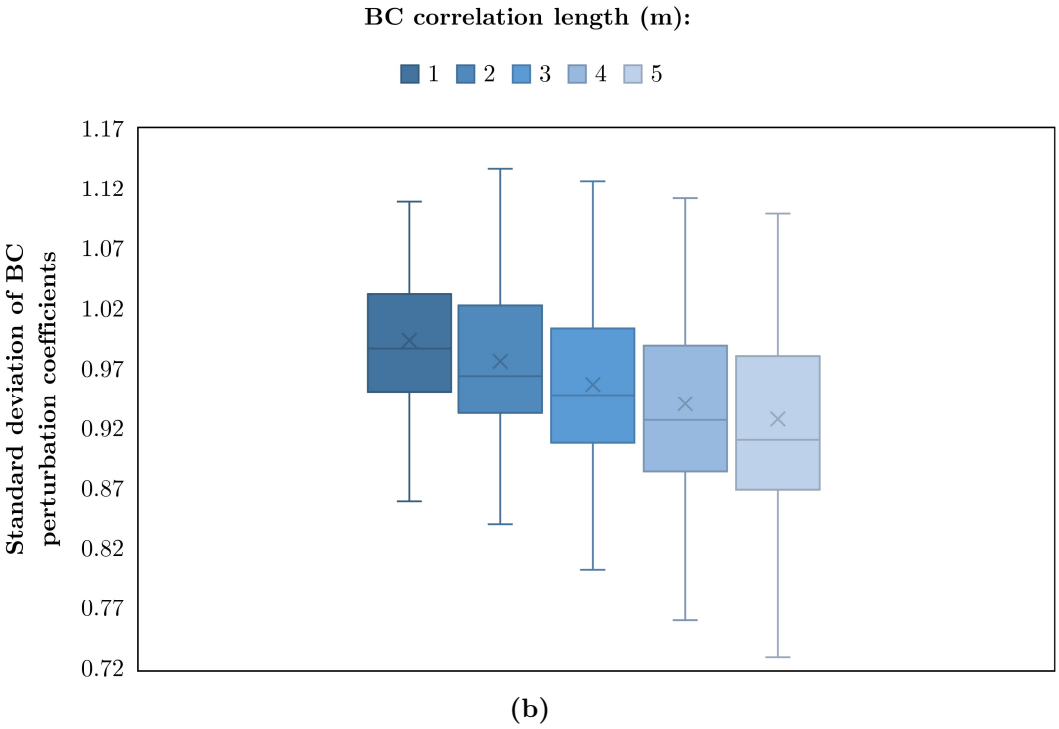

(b)

Figure 5.13 Boundary condition perturbation coefficient statistical parameters: (a) mean (b) standard deviation

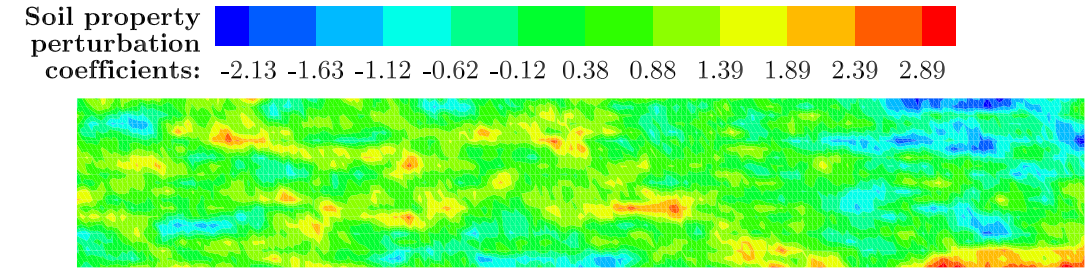

(a)

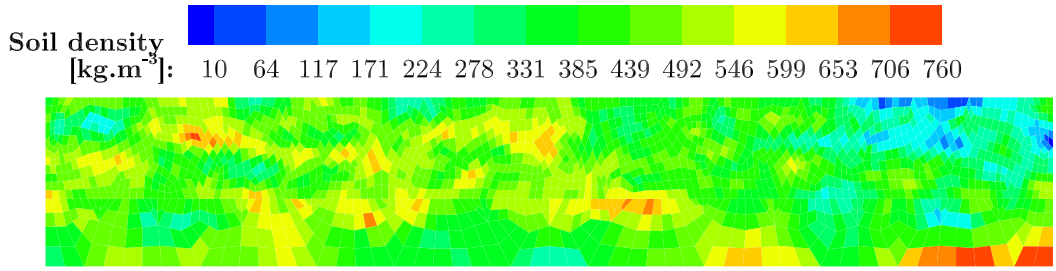

(b)

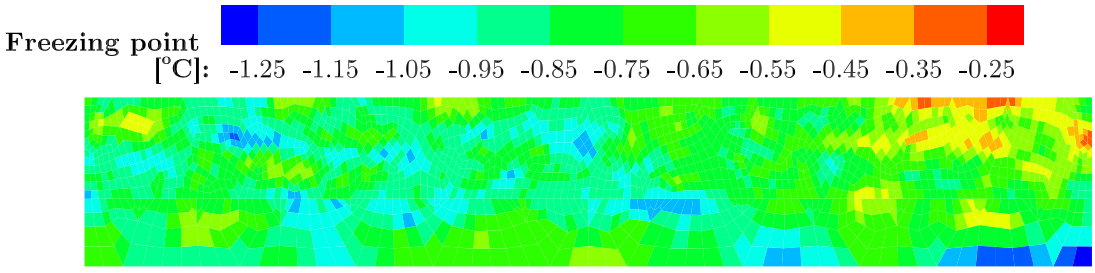

(c)

Figure 5.14 Upscaled heterogeneous soil property fields: (a) soil property perturbation coefficients for one realization (b) soil density (c) soil freezing point

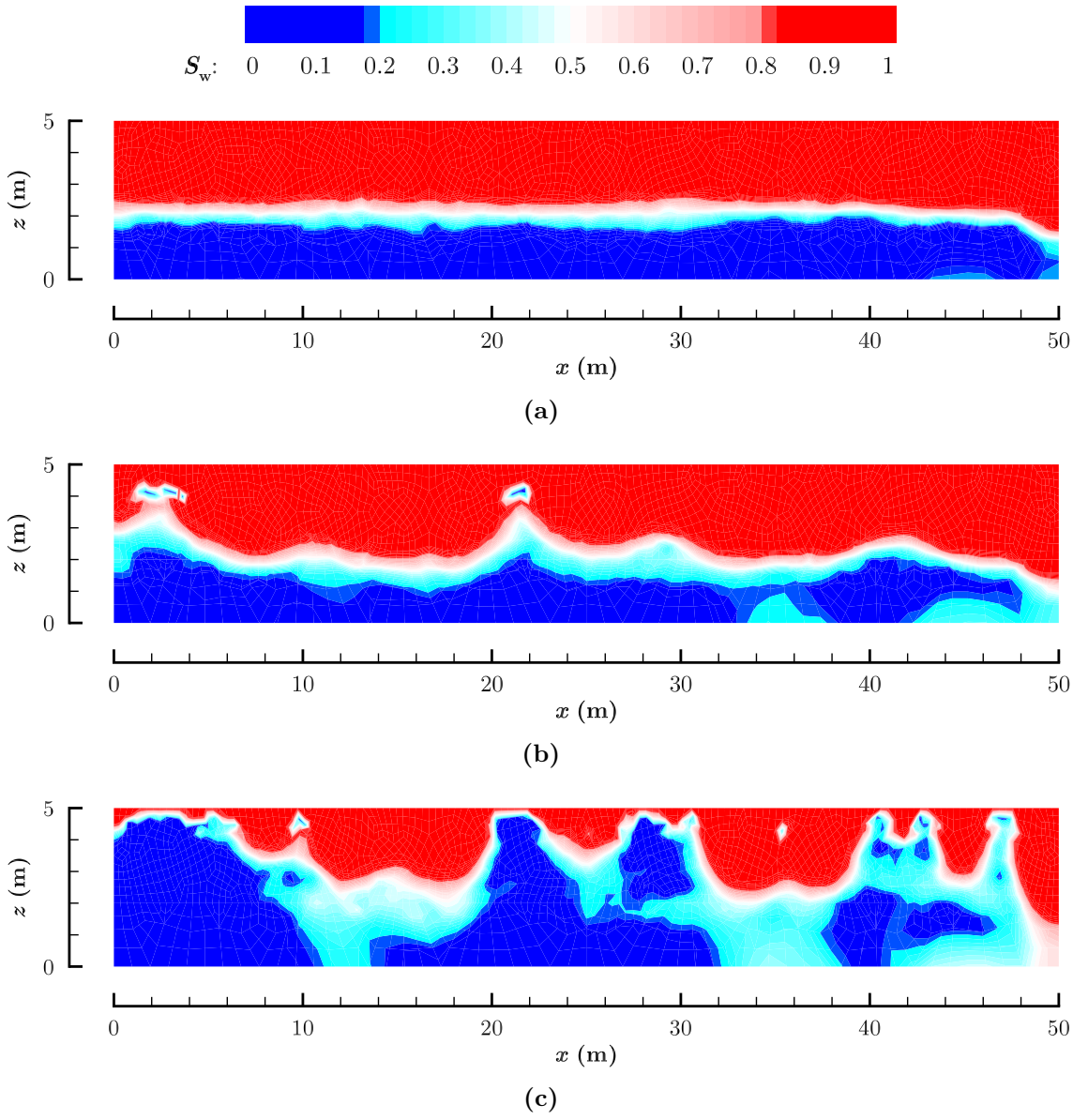

Figure 5.15 Effect of boundary condition heterogeneity on talik formations: water saturation for (a) homogeneous boundary condition (b) heterogeneous boundary condition ($\alpha = 1$m (b) heterogeneous boundary condition ($\alpha = 5$m))

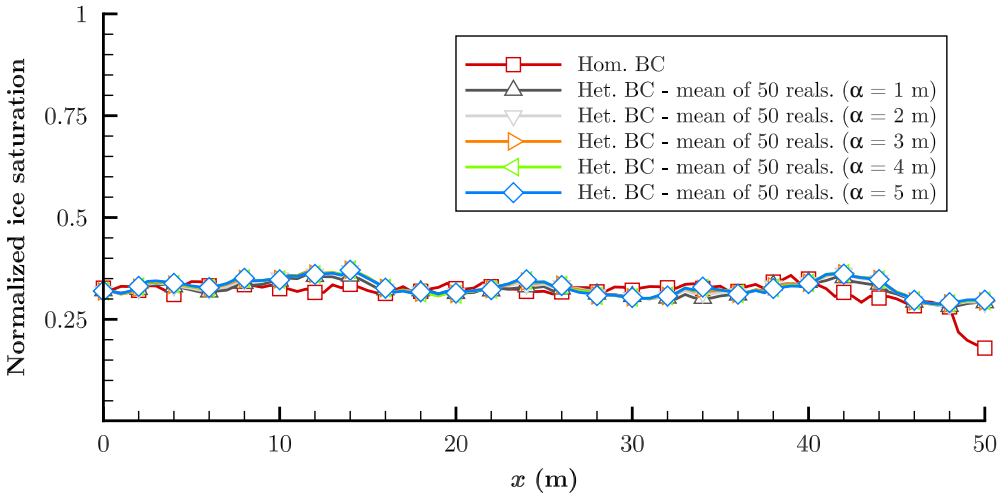

(a)

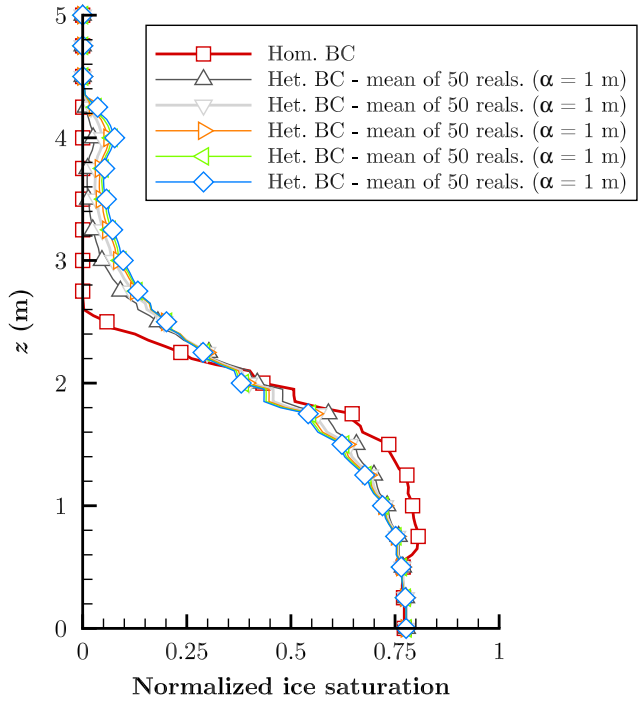

(b)

Figure 5.16 Normalized ice saturation integration. Mean vs. homogeneous case: (a) vertical integration (b) horizontal integration

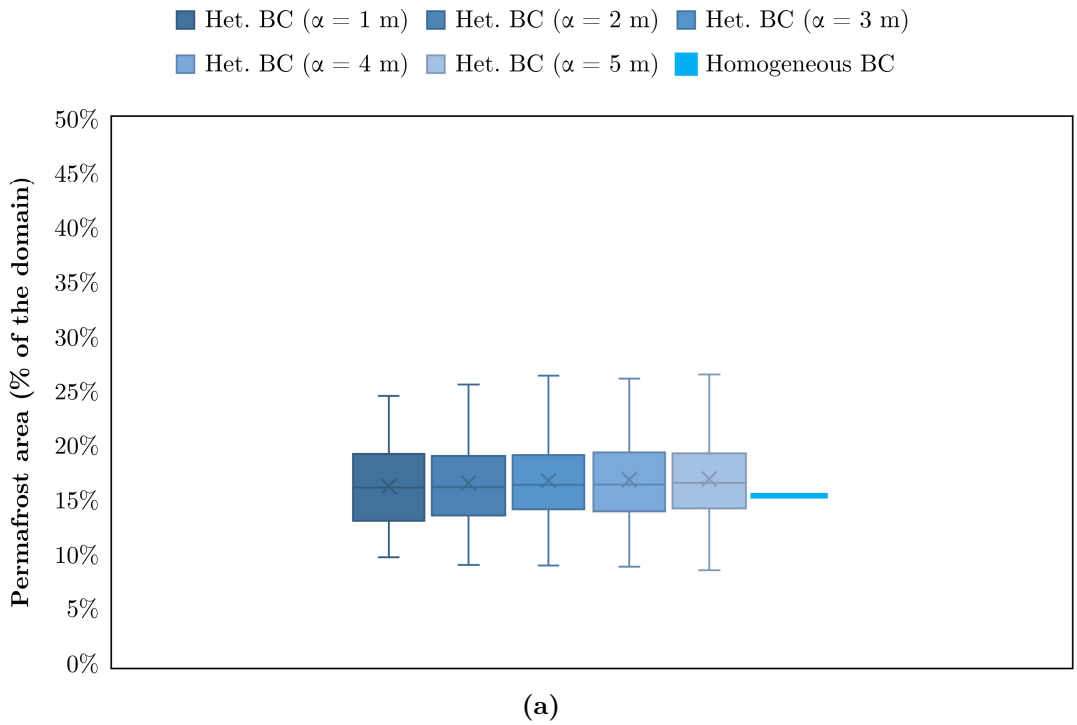

(a)

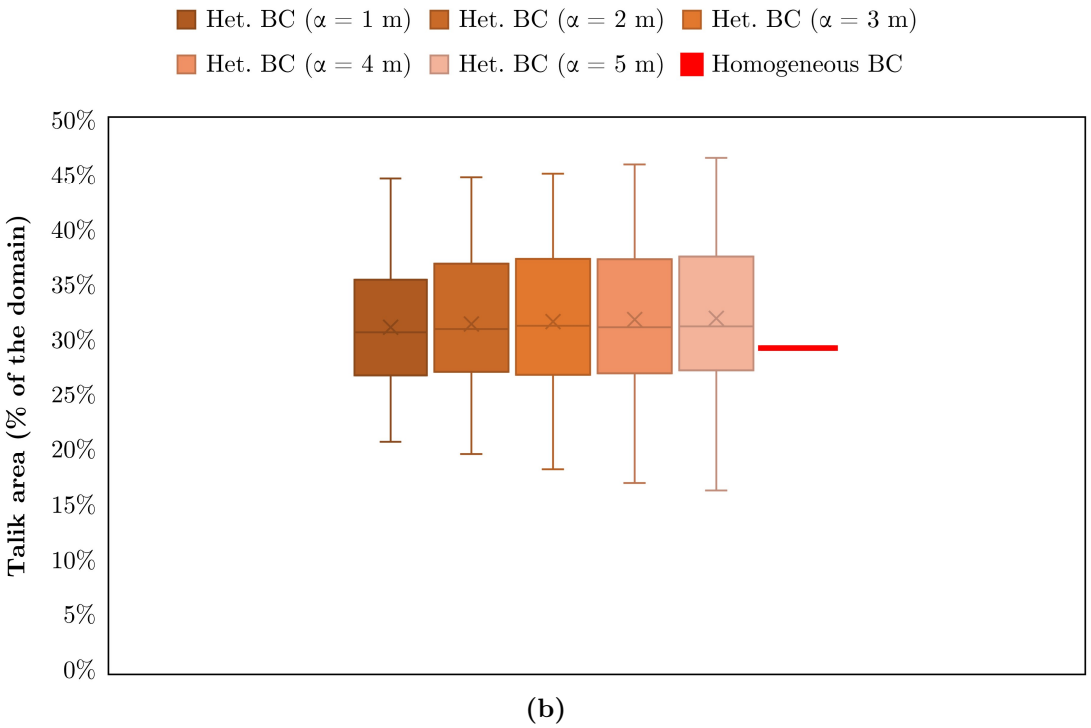

(b)

Figure 5.17 (a) Permafrost area distributions for different realizations and correlation lengths at the end of the simulation (a) Talik area distributions for different realizations and correlation lengths at the end of the simulation

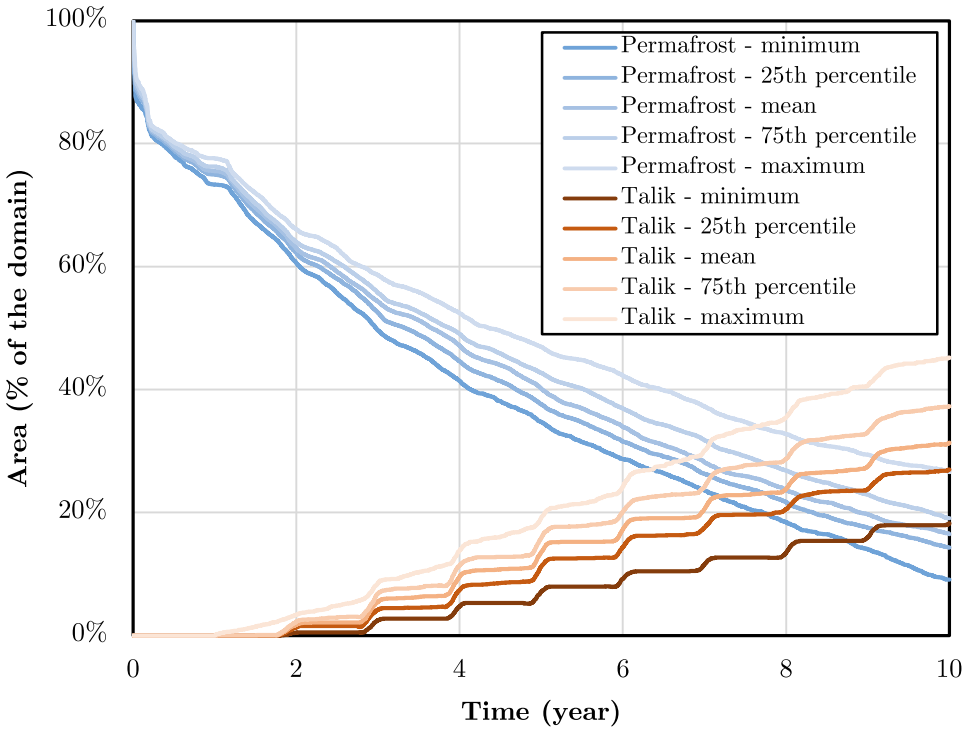

Figure 5.18 Permafrost and talik evolution during the simulation period for the simulation with $\alpha = 3$ m

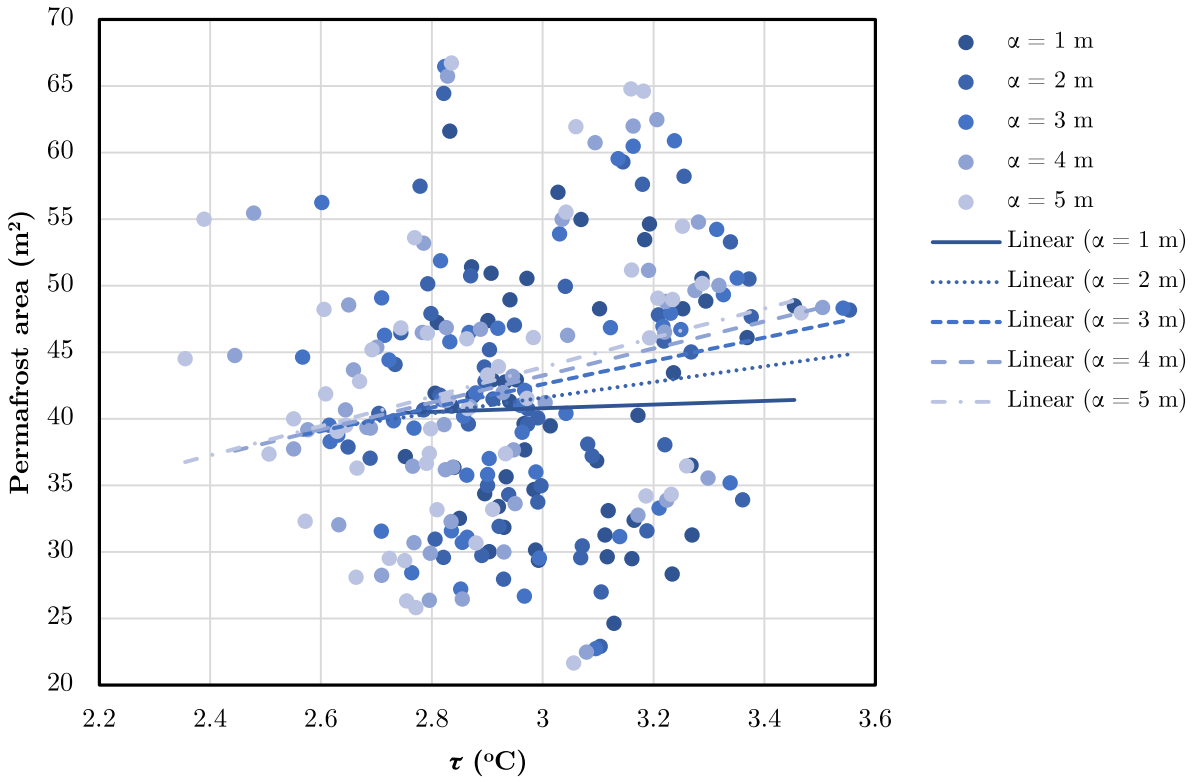

Figure 5.19 Permafrost area vs. boundary condition spatial variability factor (τ)

5.3.3 Effect of advective heat transfer on lateral permafrost thaw

In this simulation, the effect of an adjacent hydrologic feature on lateral permafrost thaw is studied with the goal of explaining the lateral degradation of permafrost observed at SCRS. A conceptual configuration similar to the observed plateaus at SCRS is considered, which is a $50\,\mathrm{m} \times 8\,\mathrm{m}$ perennially frozen heterogeneous domain ($-2.1\,^{\circ}\mathrm{C}$) initialized with a fen at the top left of the cross section (Figures 5.20 and 5.21b). The fen has material properties consistent with a flow through feature. Three 30-year simulations are run using boundary conditions with three different mean annual surface temperatures: $-2.0\,^{\circ}\mathrm{C}$, $0\,^{\circ}\mathrm{C}$, and $+2.0\,^{\circ}\mathrm{C}$ (Figure 5.22). It should be noted that to generate a surface boundary condition with the desired mean annual temperatures, the technique explained in Section 5.2.2 is used. The properties used in this simulation are listed Tables 5.2 and 5.3. The details of applying advective heat transfer are presented in Section 2.2.1. The partial differential equation governing this problem is defined as

$$\frac{\partial}{\partial t}\left(\overline{\rho c}T\right) = \frac{\partial}{\partial x}\left(\overline{K}\frac{\partial T}{\partial x}\right) + \frac{\partial}{\partial z}\left(\overline{K}\frac{\partial T}{\partial z}\right) + \rho_{\mathrm{w}} c_{\mathrm{w}} \lambda \alpha_y \Delta T, \tag{5.11}$$

where λ $[\mathrm{L}^1\mathrm{T}^{-1}]$ is the isotropic hydraulic conductivity, α_y is the hydraulic gradient (i.e. into page) in y direction, and ΔT $[\Theta]$ is the temperature difference between the ambient soil and flowing water. ρ_{w} $[\mathrm{ML}^{-3}]$ and c_{w} $[\mathrm{L}^2\mathrm{T}^{-2}\Theta^{-1}]$ are the density and specific heat capacity of water. Here, the values below are assumed for the parameters of advective heat transfer: The water saturation distribution at the end of year 30 is plotted in Figure 5.23.

Table 5.5 Advective heat transfer parameters

λ $[\mathrm{m.s}^{-1}]$	α_y $[-]$	ΔT $[^{\circ}\mathrm{C}]$
10^{-3}	0.01	0.5

In addition, the ice saturation is integrated vertically and normalized using Equation 5.9. The normalized ice saturation profiles are plotted in Figure 5.24 at 5-year intervals. The simulation results indicate a massive lateral thaw due to the existence of a channel fen, although a small temperature difference between the flowing water and ambient soil is assumed. The advective heat transfer is applied only during spring and summer (when the surface temperature is greater than zero). It can be inferred from Figure 5.23 that an increase in the mean annual temperature leads to vertical depletion of permafrost, and presence of a channel fen leads to a significant lateral degradation of permafrost. However, changes in mean annual temperature do not impact the degree of lateral thaw, which is

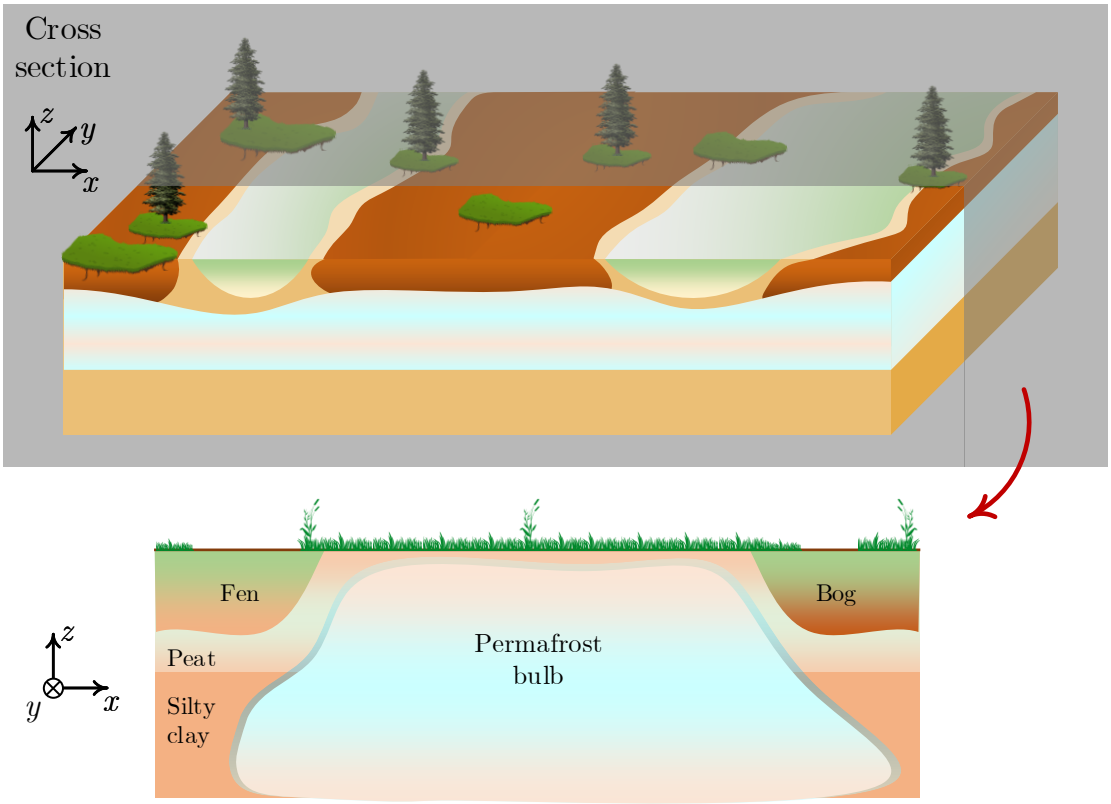

Figure 5.20 Schematics of the conceptual configuration of a permafrost-fen-bog complex

controlled by fixed inflowing temperature. More realistic simulations may be needed to study the effect of λ, ΔT, and α_y on degree of lateral thaw.

A mesh refinement study has been done to ensure the stability of the model for three different element sizes: 1800 elements (Figure 5.25a), 3500 elements (Figure 5.25b), and 6000 elements (Figure 5.25c). As is evident in Figures 5.26 and 5.27, the solutions for three different element sizes appear to be converging. This indicates that the solution is not significantly impacted by the used grid resolution.

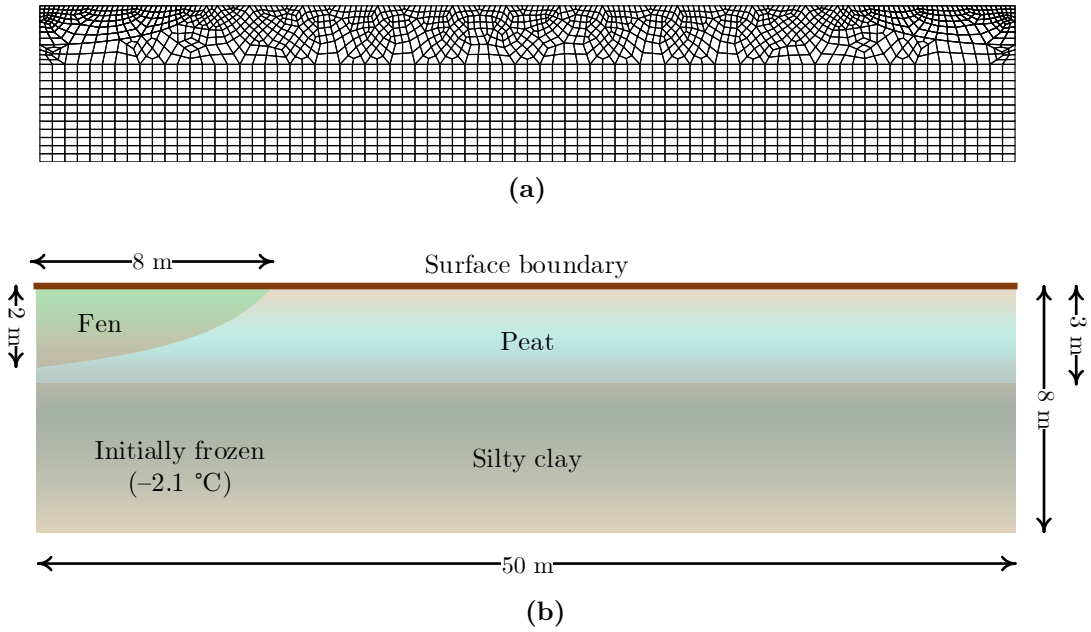

Figure 5.21 (a) Mesh of the numerical solution and (b) simulation domain configuration and initial condition

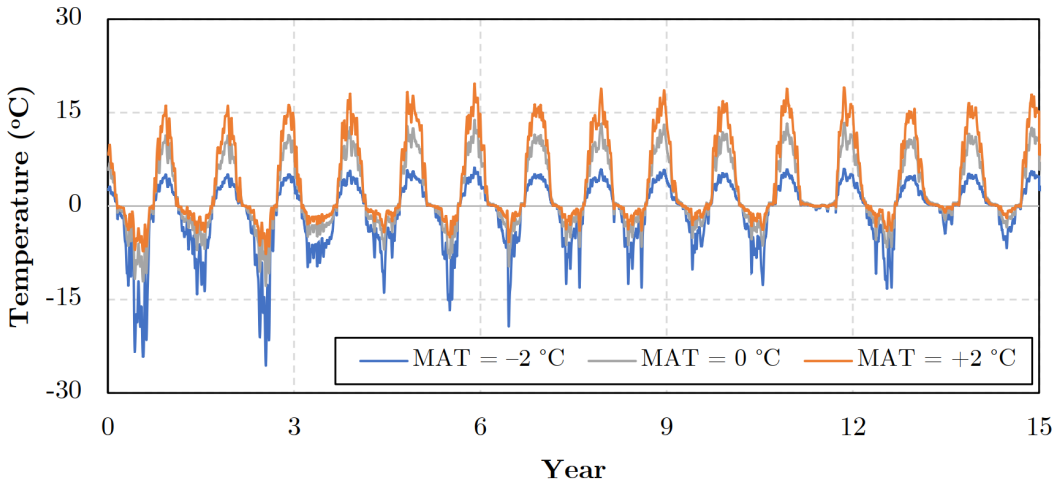

Figure 5.22 Boundary conditions with different mean annual temperatures (MATs)

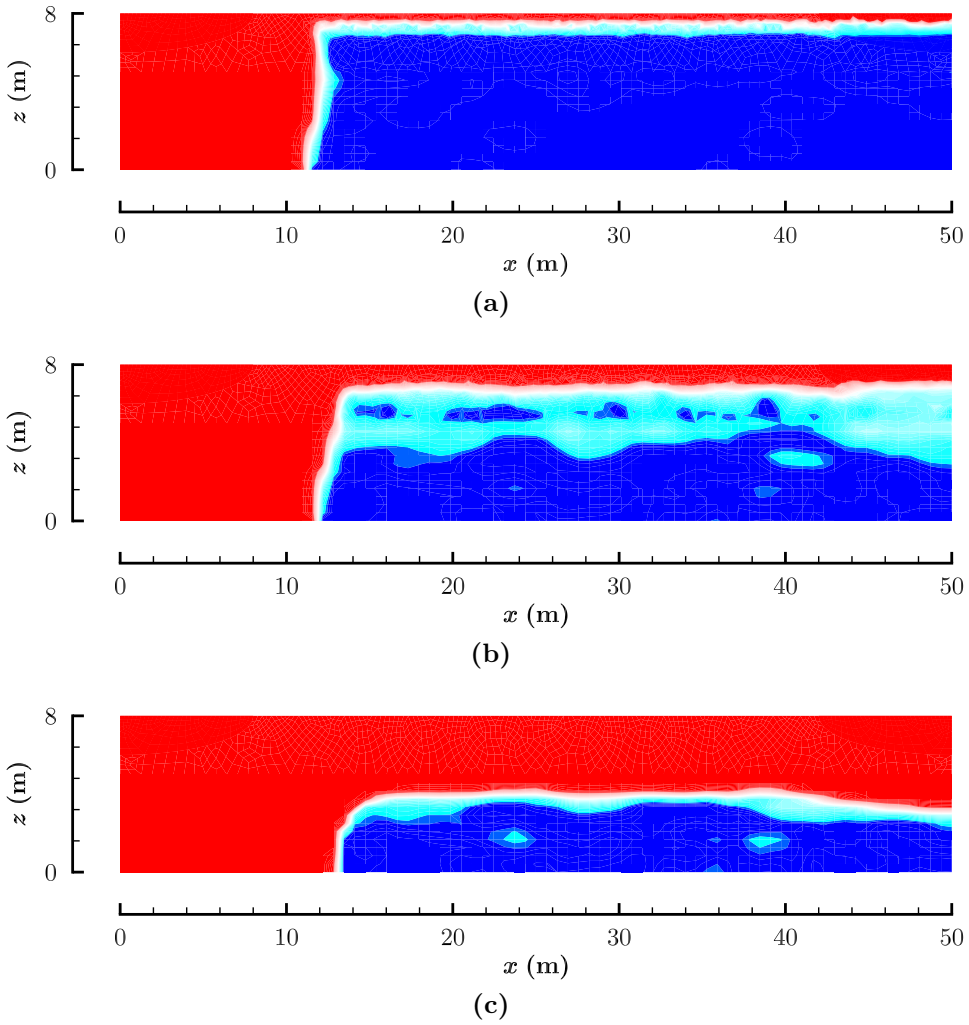

Figure 5.23 Water saturation distribution at the end of year 30. Mean annual temperature of the surface boundary: (a) −2°C, (b) 0°C, and (c) +2°C

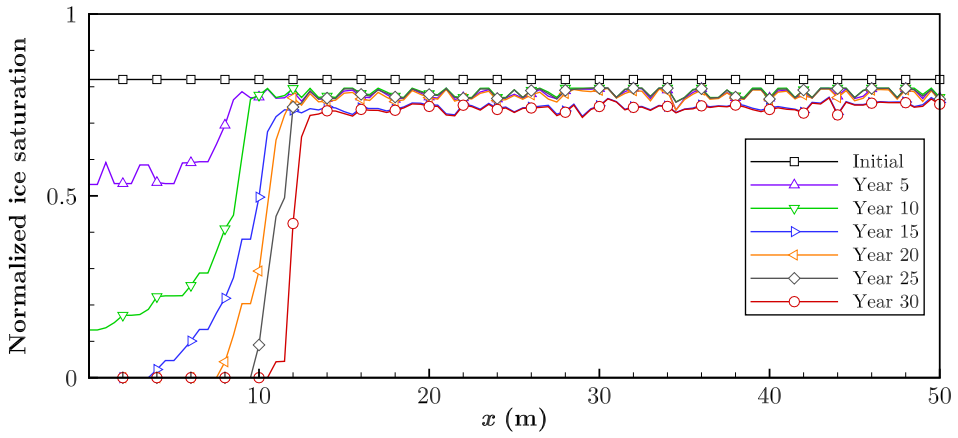

(a)

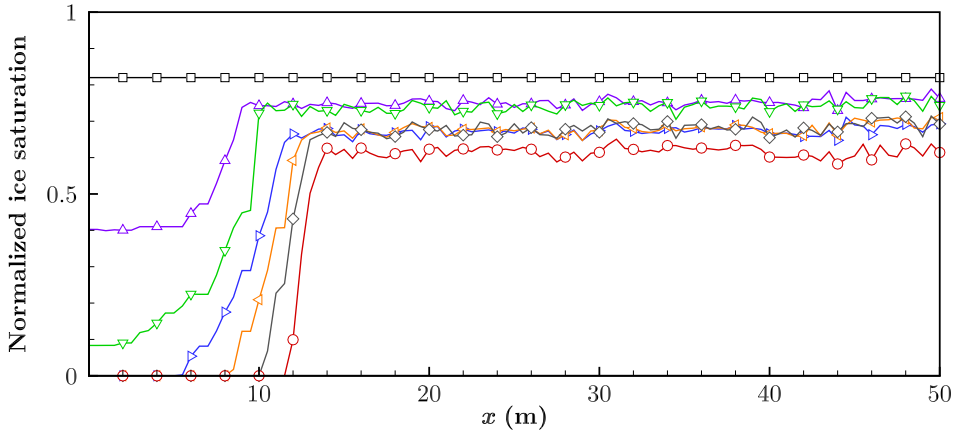

(b)

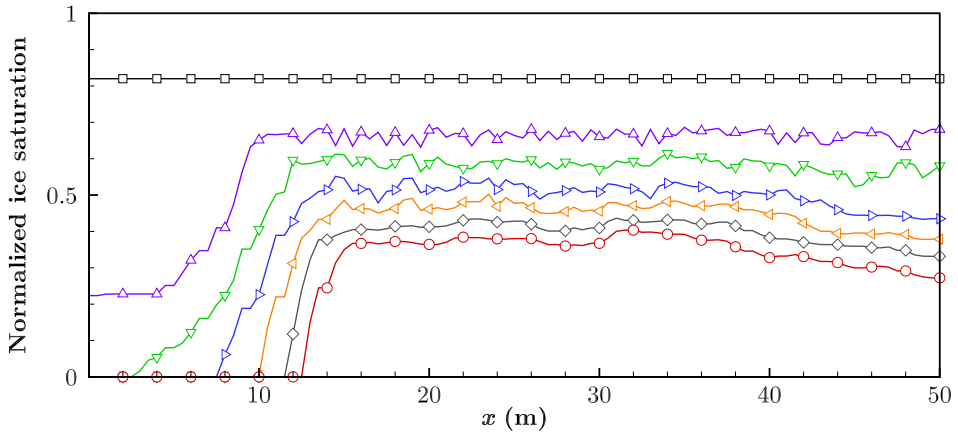

(c)

Figure 5.24 Normalized vertical integration of ice saturation. Mean annual temperature of the surface boundary: (a) −2°C, (b) 0°C, and (c) +2°C

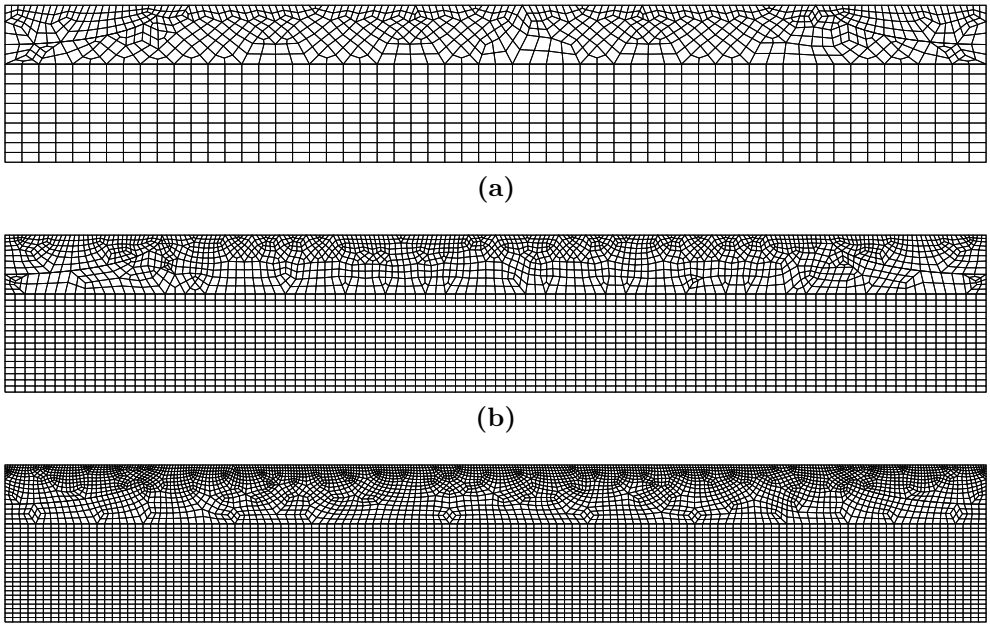

(a)

(b)

(c)

Figure 5.25 Finite element meshes for the grid size study (a) 1800 elements, (b) 3500 elements, and (c) 6000 elements

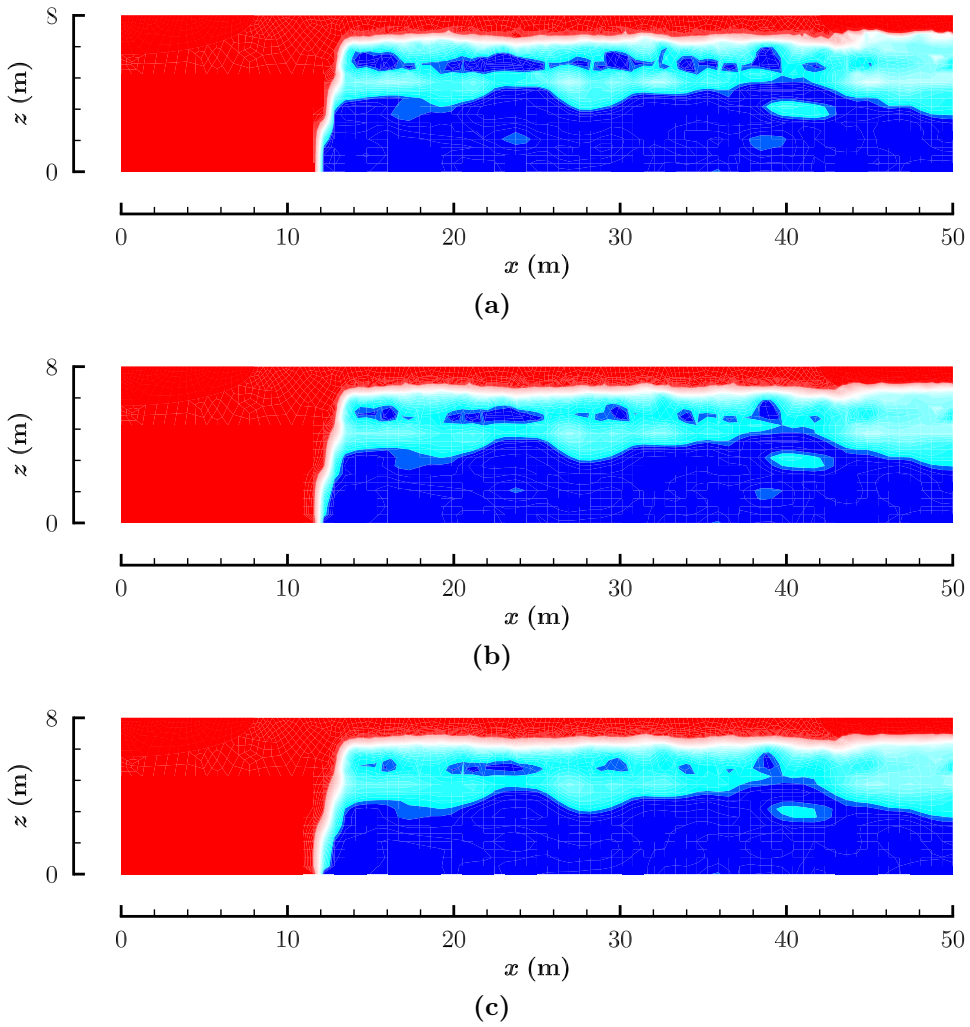

Figure 5.26 Water saturation distribution at the end of year 30 for three different meshes. Mean annual temperature of the surface boundary is 0 °C. (a) 1800 elements, (b) 3500 elements, and (c) 6000 elements

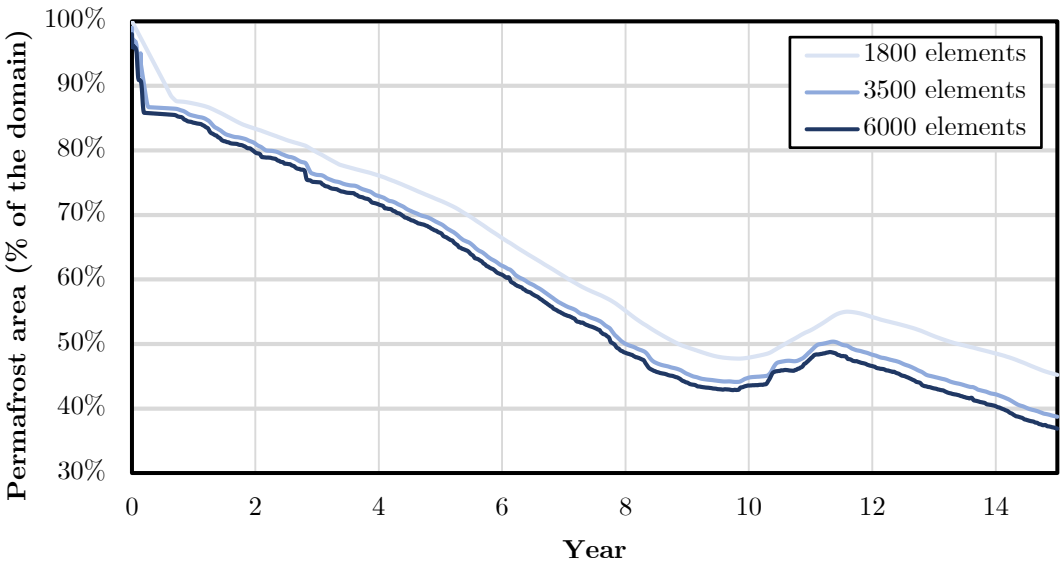

Figure 5.27 Permafrost area timeseries for solutions with different grid sizes

5.4 Conclusions

In this chapter, the developed permafrost model has been successfully validated against a 15-year temperature data collected at SCRS. The validated model has been deployed in investigating the effect of soil spatial heterogeneity on permafrost thaw patterns. A set of sensitivity analyses has been carried out to identify the parameters that permafrost thaw is most sensitive to. The results of the sensitivity analyses are analyzed using Sobol' scheme, which is a variance-based sensitivity analysis method. The Sobol' analysis indicated that correlation length of the spatially correlated heterogeneous medium has minimal effect on the long term evolution of permafrost when surface conditions are homogeneous. In addition, permafrost evolution and talik formation are most sensitive to the variation of freezing point (even within a very small temperature range) and heterogeneity correlation length, respectively.

The heterogeneity of the surface energy boundary condition was represented by locally perturbing field collected surface temperatures by generating spatially correlated surface temperature field-informed by spatial temperature variance observed at SCRS. The averaged 15-year permafrost and talik areas for 50 simulations are close to those of the simulation with homogeneous boundary condition; however, a close look at the water saturation contours of the heterogeneous cases reveals the effect of heterogeneity on the confined talik formations, which may become preferential water pathways. A factor, τ, was introduced for quantifying boundary condition variability, which is calculated as the time average of the standard deviation of the surface temperature. Simulations with larger surface correlation lengths showed more sensitivity to an increase in surface temperature variability. Moreover, for a constant surface variability correlation length, the general pattern was that more permafrost would remain frozen at the end of the realizations with higher spatial variability in boundary condition; however, a patchier distribution of surface land cover can be expected at end of the simulation (e.g. confined and open talik formation). The most important outcome of this experiment is the potential necessity of running higher spatial resolution permafrost simulations that can handle talik formation because the thaw patterns of permafrost using a heterogeneous boundary condition can be significantly different from that of using a homogeneous boundary condition.

The effect of out-of-page flow on the lateral permafrost thaw has been investigated. The results indicate that the presence of a hydrologic feature with a relatively higher hydraulic conductivity than the ambient soil can lead to a massive lateral permafrost thaw, similar to what is observed at SCRS.

Chapter 6

Conclusions and suggestions for future research

6.1 Summary of the research

In this research, characterizing the effect of heterogeneity on permafrost thaw was the central goal. As a starting point, a realistic and robust permafrost model was developed that was capable of handling thaw scenarios in highly heterogeneous media without convergence issues. In order to realistically capture the phase-change process in soil, the enthalpy approach was deployed, which enables us to simulate phase-change over a range of temperatures. The model was verified against the existing theoretical solution for a non-isothermal phase change and was validated against 15 years of temperature data collected at Scotty Creek Research Station (SCRS).

In Chapter 3 (Amiri et al., 2018), an extended finite element method (XFEM) model was developed and implemented to study the the effect of microscopic heterogeneity on the shape of soil freezing curves (SFCs). The study suggests that the relation between the soil water characteristic curve (SWCC) and SFC might not be wholly characterizing the extent of SFCs, and that local heterogeneity may also impact SFC shape and range. The implemented approach led to a closed-form relationship for representing the SFC, which is dependent solely upon the soil-water-ice system heterogeneity. It was shown that the heterogeneity-informed SFC generated using a small standard deviation for the soil properties yields to an almost sharp relation between temperature and water saturation, which is expected for homogeneous materials. While the impact of heterogeneity in soil properties at the representative elementary volume (REV) scale was shown to be small relative to that due to the media pore size distribution, this is the first study to demonstrate that local material heterogeneity plays any role in influencing the SFC.

Chapter 4 (Amiri et al., 2019) provides the details of the implementation of the trust region algorithm that was deployed for alleviating the non-linearity induced by the non-convex and highly non-linear functions used in the enthalpy approach. The model was verified against the analytical solution provided by Lunardini (1981). The spatial and temporal convergence studies were conducted to guarantee acceptable convergence rates. In this chapter, it was shown that standard methods (e.g. standard Newton-Raphson and *L*-scheme) suffer from convergence issues. Moreover, different functions were used for representing the SFC to illustrate the effect of the shape of the SFC on the convergence rates. Subsequent application of this model in Chapter 5 further confirmed the robustness of implementation, as the model was deployed for 15,000 stochastic material property distributions without failing.

Chapter 5 (Amiri and Craig, 2019) addresses the main goal of this research. The geo-

statistical software library (GSLIB) was linked to the C++ computer program of the model to run heterogeneous simulations. A comprehensive sensitivity analysis was conducted to identify the sensitivity levels of permafrost thaw to the ranges of the heterogeneous soil parameters with uniform external forcing. The Sobol' sensitivity analysis indicated a minimal dependency of permafrost systems on the degree of heterogeneity of soil dry density (and therefore thermal and hydraulic conductivities). In addition, the dependency of permafrost evolution on the range of freezing point and talik formation on the heterogeneity correlation length were shown. The results of the simulations using heterogeneous boundary conditions revealed a completely different distribution of permafrost thaw pattern for the 50 different realizations of the spatially correlated heterogeneous boundary condition compared with the simulation with a homogeneous boundary condition. Results demonstrated that while soil property heterogeneity moderately impacted system response, the impact was fully eclipsed by the much stronger influence of boundary condition heterogeneity. The practical implications of this are that the conventional treatment of frozen soils in permafrost models as laterally homogeneous is acceptable, but that local heterogeneity in surface energetics will generally need to be represented explicitly, particularly when correlation lengths are large. Finally, an experimental simulation was designed and conducted to investigate the effect of advective heat transfer on the vertical and lateral degradation of permafrost, where influence of advection in the y-direction was treated as a distributed energy source in the xz-plane. This experimental simulation set indicates that the presence of a highly-conductive hydrologic feature, i.e. a channel fen, can accelerate the lateral permafrost thaw rates. The use of boundary conditions with different mean annual temperature revealed that an increase in the mean annual temperature solely cannot create dramatic lateral permafrost degradation, although an increase in the mean annual temperature has a direct effect on the vertical permafrost degradation.

6.2 Suggestions for future research

Some of the pathways that can be pursued as a continuation of this work are as follows:

1. The advective heat transfer considered in this model was taken to occur due to a constant pressure head perpendicular to the domain of the problem. The energy balance equation with mass balance can be coupled to better understand the effect of advective heat transfer on permafrost thaw.

2. The developed code can be coupled with land cover models for a better representation of surface boundary heterogeneity.

3. The existing code can be extended to three dimensions. By this extension, a field scale simulation can be run, which might provide better insights regarding the projections of the state of permafrost in the Northwest Territories (NWT).

4. Extend the current work to unsaturated media. Such an extension requires a complicated coupling of two-phase fluid flow (water and air) with heat transfer. Moreover, this coupling enables the recreation of field conditions in summer, during which the active layer is almost dry according to field observations.

6.3 Publications and presentations

6.3.1 Journal and conference articles

Chapters 3 and 4 of this thesis is published in peer-reviewed journals, and Chapter 5 is prepared for a journal article. The list of the publications are as follows:

- **Amiri, E. A.**, Craig, J. R., and Kurylyk, B. L. (2018). A theoretical extension of the soil freezing curve paradigm. Advances in Water Resources, 111(November 2017), 319-328. https://doi.org/10.1016/j.advwatres.2017.11.021

- **Amiri, E. A.**, Craig, J. R., and Hirmand, M. R. (2019). A trust region approach for numerical modeling of non-isothermal phase change. Computational Geosciences, 911-923. https://doi.org/10.1007/s10596-019-09846-3

- **Amiri, E. A.**, and Craig, J. R. (2019). Effect of Soil Thermal Heterogeneity on Permafrost Evolution. In Cold Regions Engineering 2019 (pp. 492-499). Reston, VA: American Society of Civil Engineers. https://doi.org/10.1061/9780784482599.057

6.3.2 Conference presentations

Segments of this research were presented at the following conferences:

- **Amiri, E. A.**, Craig, J. R. (2019). Effect of soil thermal heterogeneity on permafrost evolution. 18th International Conference on Cold Regions Engineering, August 2019, Quebec City, Quebec, Canada.

- **Amiri, E. A.**, Craig, J. R. (2019). Soil freezing point heterogeneity and talik formations. 27th IUGG General Assembly, July 2019, Montreal, Quebec, Canada.

- **Amiri, E. A.**, Craig, J. R., Hirmand, MR., Devoie, E. G., Quinton, W. L. (2018). Numerical simulation of lateral permafrost thaw in Northwest Territories. 5th European Conference on Permafrost. June 2018, Chamonix Mont-Blanc, France.

- **Amiri, E. A.**, Craig, J. R., Hirmand, MR., Devoie, E. G. (2018). Controlling factors on lateral permafrost thaw in the Northwest Territories: a numerical study. 2018 Joint Meeting of CGU, CSSS, CIG, ES-SSA and CSAFM. June 2018. Niagara Falls, Ontario, Canada.

- **Amiri, E. A.**, Craig, J. R. (2018). Numerical modelling of permafrost. Cold Regions Research Centre Days. November 2018, Wilfrid Laurier University, Waterloo, Ontario, Canada.

References

Adalsteinsson, D. and Sethian, J. (1999), 'The Fast Construction of Extension Velocities in Level Set Methods', *Journal of Computational Physics* **148**(1), 2–22.

Adams, E. E. and Gelhar, L. W. (1992), 'Field study of dispersion in a heterogeneous aquifer: 2. Spatial moments analysis', *Water Resources Research* **28**(12), 3293–3307.

Alexiades, V. and Solomon, A. D. A. (1993), *Mathematical modeling of melting and freezing processes*, Vol. 251, CRC Press.

Amiri, E. A. and Craig, J. R. (2019), Effect of Soil Thermal Heterogeneity on Permafrost Evolution, *in* 'Cold Regions Engineering 2019', American Society of Civil Engineers, E, pp. 492–499.

Amiri, E. A., Craig, J. R. and Hirmand, M. R. (2019), 'A trust region approach for numerical modeling of non-isothermal phase change', *Computational Geosciences* **23**(5), 911–923.

Amiri, E. A., Craig, J. R. and Kurylyk, B. L. (2018), 'A theoretical extension of the soil freezing curve paradigm', *Advances in Water Resources* **111**(November 2017), 319–328.

Atchley, A. L., Painter, S. L., Harp, D. R., Coon, E. T., Wilson, C. J., Liljedahl, A. K. and Romanovsky, V. E. (2015), 'Using field observations to inform thermal hydrology models of permafrost dynamics with ATS (v0.83)', *Geoscientific Model Development* **8**(9), 2701–2722.

Ayasoufi, A. and Keith, T. G. (2004), 'Application of the Conservation Element and Solution Element Method in Numerical Modeling of Axisymmetric Heat Conduction with Melting and/or Freezing', *JSME International Journal* **47**(1), 11.

Baltzer, J. L., Veness, T., Chasmer, L. E., Sniderhan, A. E. and Quinton, W. L. (2014), 'Forests on thawing permafrost: Fragmentation, edge effects, and net forest loss', *Global Change Biology* **20**(3), 824–834.

Banin, A. and Anderson, M. D. (1974), 'Effects of Salt Concentration Changes During Freezing on the Unfrozen Water Content of Porous Materials', *Water Resources Research* **10**(1), 124–128.

Bao, H., Koike, T., Yang, K., Wang, L., Shrestha, M. and Lawford, P. (2016), 'Development of an enthalpy-based frozen soil model and its validation in a cold region in China', *Journal of Geophysical Research: Atmospheres* **121**(10), 1–19.

Belshe, E. F., Schuur, E. A. G., Bolker, B. M. and Bracho, R. (2012), 'Incorporating spatial heterogeneity created by permafrost thaw into a landscape carbon estimate', *Journal of Geophysical Research: Biogeosciences* **117**(1), 1–14.

Belytschko, T. and Black, T. (1999), 'Elastic Crack Growth in Finite Elements With Minimal Remeshing', *Int. J. Numer. Meth. Engng* **45**(July 1998), 601–620.

Bense, V. F., Ferguson, G. and Kooi, H. (2009), 'Evolution of shallow groundwater flow systems in areas of degrading permafrost', *Geophysical Research Letters* **36**(22), L22401.

Bernauer, M. K. and Herzog, R. (2012), 'Implementation of an X-FEM solver for the classical two-phase stefan problem', *Journal of Scientific Computing* **52**(2), 271–293.

Bhatti, M. A. (2005), 'Fundamental Finite Element Analysis and Applications: with Mathematica and Matlab Computations', p. 720.

Bonan, G. B. (2008), *Ecological climatology : concepts and applications*, Cambridge University Press.

Bouchard, F., MacDonald, L. A., Turner, K. W., Thienpont, J. R., Medeiros, A. S., Biskaborn, B. K., Korosi, J., Hall, R. I., Pienitz, R. and Wolfe, B. B. (2017), 'Paleolimnology of thermokarst lakes: a window into permafrost landscape evolution', *Arctic Science* **3**(2), 91–117.

Budhia, H. and Kreith, F. (1973), 'Heat transfer with melting or freezing in a wedge', *International Journal of Heat and Mass Transfer* **16**(1), 195–211.

Bundschuh, J. (2010), *Introduction to the Numerical Modeling of Groundwater and Geothermal Systems*, CRC Press.

Campolongo, F., Cariboni, J. and Saltelli, A. (2007), 'An effective screening design for sensitivity analysis of large models', *Environmental Modelling and Software* **22**(10), 1509–1518.

Cannell, G. H. and Gardner, W. H. (1959), 'Freezing-Point Depressions in Stabilized Soil Aggregates, Synthetic Soil, and Quartz Sand1', *Soil Science Society of America Journal* **23**(6), 418.

Celia, M. A., Bouloutas, E. T. and Zarba, R. L. (1990), 'A general Mass-Consesrvative Numerical Solution for the Unsaturated Flow Equation', *Water Resources Research* **26**(1), 1483–1496.

Chamberlain, E. J. and Gow, A. J. (1979), 'Effect of freezing and thawing on the permeability and structure of soils', *Engineering Geology* **13**(1-4), 73–92.

Chessa, J., Smolinski, P. and Belytschko, T. (2002), 'The extended finite element method (XFEM) for solidification problems', *International Journal for Numerical Methods in Engineering* **53**(8), 1959–1977.

Clauser, C. and Huenges, E. (1999), 'Thermal Conductivity of Rocks and Minerals', *Rock Physics & Phase Relations* (1), 1–22.

Comini, G., Del Guidice, S., Lewis, R. W. and Zienkiewicz, O. C. (1974), 'Finite element solution of non-linear heat conduction problems with special reference to phase change', *Int. J. num. Meth. Engng.* **8**(3), 613–624.

Connon, R., Devoie, É., Hayashi, M., Veness, T. and Quinton, W. (2018), 'The Influence of Shallow Taliks on Permafrost Thaw and Active Layer Dynamics in Subarctic Canada', *Journal of Geophysical Research: Earth Surface* **123**(2), 281–297.

Connon, R. F., Quinton, W. L., Craig, J. R. and Hayashi, M. (2014), 'Changing hydrologic connectivity due to permafrost thaw in the lower Liard River valley, NWT, Canada', *Hydrological Processes* **28**(14), 4163–4178.

Crank, J. (1999*a*), *Free and moving boundary problems*.

Crank, J. (1999*b*), *Free and moving boundary problems*.

Cuntz, M., Mai, J., Samaniego, L., Clark, M., Wulfmeyer, V., Branch, O., Attinger, S. and Thober, S. (2016), 'The impact of standard and hard-coded parameters on the

hydrologic fluxes in the Noah-MP land surface model', *Journal of Geophysical Research* **121**(18), 10,676–10,700.

Cuntz, M., Mai, J., Zink, M., Thober, S., Kumar, R., Schäfer, D., Schrön, M., Craven, J., Rakovec, O., Spieler, D., Prykhodko, V., Dalmasso, G., Musuuza, J., Langenberg, B., Attinger, S. and Samaniego, L. (2015), 'Computationally inexpensive identification of noninformative model parameters by sequential screening', *Water Resources Research* **51**(8), 6417–6441.

Dall'Amico, M., Endrizzi, S., Gruber, S. and Rigon, R. (2011), 'A robust and energy-conserving model of freezing variably-saturated soil', *Cryosphere* **5**(2), 469–484.

Deutsch, C. V. and Journel, A. G. (1997), *GSLIB: Geostatistical software library and user's guide*, Vol. 369, 2nd edn, Oxford University Press.

Devoie, É. G., Craig, J. R., Connon, R. F. and Quinton, W. L. (2019), 'Taliks: A Tipping Point in Discontinuous Permafrost Degradation in Peatlands', *Water Resources Research* **55**(11), 9838–9857.

DHI-WAYS (2016), piFreeze: a freeze/thaw plug-in for FEFLOW, Technical report, MIKE - Powered by DHI.

Douglas, J. (1956), 'A uniqueness theorem for the solution of a Stefan problem', *Proceedings of the American Mathematical Society* **8**, 402–408.

Dyke, L. D. and Brooks, G. R. (2000), 'The physical environment of the Mackenzie valley, Northwest Territories : a base line for the assessment of environmental change', p. 208.

Entekhabi, D. and Eagleson, P. S. (1989), 'Land Surface Hydrology Parameterization for Atmospheric General Circulation models Including Subgrid Scale Spatial Variability', *Journal of Climate* **2**(8), 816–831.

Environment and Natural resources - Northwest Territories (2014), '13. Permafrost — Environment and Natural Resources'.

Evans, G. (1951), 'A note on the existence of a solution to a problem of Stefan', *Quarterly of Applied Mathematics* **9**(2), 185–193.

Eyres, N. R., Hartree, D. R., Ingham, J., Jackson, R., Sarjant, R. J. and Wagstaff, J. B. (1946), 'The Calculation of Variable Heat Flow in Solids', *Philosophical Transactions of*

the Royal Society of London. Series A, Mathematical and Physical Sciences **240**(813), 1 LP – 57.

Flerchinger, G. G. N. G. G. N. (2000), 'The Simultaneous Heat and Water (SHAW) Model: Technical documentation', *Northwest Watershed Research Center USDA ...* p. 40.

Flerchinger, G. N. and Saxton, K. E. (1989), 'Snow-Residue-Soil System I . Theory and Development', *Soil and Water Division, ASAE* **32**(2), 565–567.

Flerchinger, G. N., Seyfried, M. S. and Hardegree, S. P. (2006), 'Using Soil Freezing Characteristics to Model Multi-Season Soil Water Dynamics', *Vadose Zone Journal* **5**(4), 1143–1153.

Grenier, C., Anbergen, H., Bense, V., Chanzy, Q., Coon, E., Collier, N., Costard, F., Ferry, M., Frampton, A., Frederick, J., Gonçalvès, J., Holmén, J., Jost, A., Kokh, S., Kurylyk, B., McKenzie, J., Molson, J., Mouche, E., Orgogozo, L., Pannetier, R., Rivière, A., Roux, N., Rühaak, W., Scheidegger, J., Selroos, J. O., Therrien, R., Vidstrand, P. and Voss, C. (2018), 'Groundwater flow and heat transport for systems undergoing freeze-thaw: Intercomparison of numerical simulators for 2D test cases', *Advances in Water Resources* **114**(February), 196–218.

Groenevelt, P. H. and Kay, B. D. (1974), 'On the Interaction of Water and Heat Transport in Frozen and Unfrozen Soils: II. The Liquid Phase', *Soil Science Society of America Journal* **38**(3), 400.

GSLIB Help Page: Programs - http://www.gslib.com/gslib_help/programs.html (n.d.).

Hansson, K., Šimunek, J., Mizoguchi, M., Lundin, L.-C., van Genuchten, M. T., Šimůnek, J., Mizoguchi, M., Lundin, L.-C. and van Genuchten, M. T. (2004), 'Water flow and heat transport in frozen soil', *Vadose Zone Journal* **3**(2), 693–704.

Harp, D. R., Atchley, A. L., Painter, S. L., Coon, E. T., Wilson, C. J., Romanovsky, V. E. and Rowland, J. C. (2016), 'Effect of soil property uncertainties on permafrost thaw projections: A calibration-constrained analysis', *Cryosphere* **10**(1), 341–358.

Hayashi, M., Van Der Kamp, G. and Schmidt, R. (2003), 'Focused infiltration of snowmelt water in partially frozen soil under small depressions', *Journal of Hydrology* **270**(3-4), 214–229.

Hill, J. (1987), *One-Dimensional Stefan Problems: An Introduction*, Longman Scientific and Technical, New York, USA.

Hinzman, L. D., Bettez, N. D., Bolton, W. R., Chapin, F. S., Dyurgerov, M. B., Fastie, C. L., Griffith, B., Hollister, R. D., Hope, A., Huntington, H. P., Jensen, A. M., Jia, G. J., Jorgenson, T., Kane, D. L., Klein, D. R., Kofinas, G., Lynch, A. H., Lloyd, A. H., McGuire, A. D., Nelson, F. E., Oechel, W. C., Osterkamp, T. E., Racine, C. H., Romanovsky, V. E., Stone, R. S., Stow, D. A., Sturm, M., Tweedie, C. E., Vourlitis, G. L., Walker, M. D., Walker, D. A., Webber, P. J., Welker, J. M., Winker, K. S. and Yoshikawa, K. (2005), 'Evidence and implications of recent climate change in Northern Alaska and other Arctic regions', *Climatic Change* **72**(3), 251–298.

Hirmand, M. R. and Papoulia, K. D. (2018), 'A continuation method for rigid-cohesive fracture in a discontinuous Galerkin finite element setting', *International Journal for Numerical Methods in Engineering* (April), 627–650.

Hwang, C., Murray, D. and Brooker, E. (1971), 'A Thermal Analysis for Structures on permafrost', *Canadian Geotechnical Journal* .

Ippisch, O. (2001), Coupled Transport in Natural Porous Media, PhD thesis, Heidelberg, Germany: Rupertus Carola University.

Jamshidi, R. J., Lake, C. B. and Barnes, C. L. (2015), 'Examining Freeze/Thaw Cycling and its Impact on the Hydraulic Performance of a Cement-Treated Silty Sand', *Journal of Cold Regions Engineering* **29**(3).

Jansson, P. E. and Karlberg, L. (2004), 'Coupled heat and mass transfer model for soil-plant-atmosphere systems', p. 365.

Johannessen, O. M., Bengtsson, L., Miles, M. W., Kuzmina, S. I., Semenov, V. A., Alekseev, G. V., Nagurnyi, A. P., Zakharov, V. F., Bobylev, L. P., Pettersson, L. H., Hasselmann, K. and Cattle, H. P. (2004), 'Arctic climate change: observed and modelled temperature and sea-ice variability', *Tellus A: Dynamic Meteorology and Oceanography* **56**(4), 328–341.

Jorgenson, M. T. and Osterkamp, T. E. (2005), 'Response of boreal ecosystems to varying modes of permafrost degradation', *Canadian Journal of Forest Research* **35**(9), 2100–2111.

Kay, B. D. and Groenevelt, P. H. (1974), 'On the Interaction of Water and Heat Transport in Frozen and Unfrozen Soils: I. Basic Theory; The Vapor Phase', *Soil Science Society of America Journal* **38**(3), 395.

Kemper, W. D. W. and Rosenau, R. C. R. C. (1986), 'Aggregate Stability and Size Distributlon', *Methods of Soil Analysis, Part 1 - Physical and Mineralogical Methods* **9**(9), 425–442.

Khoei, A. R. (2005), *Computational Plasticity in Powder Forming Processes*, Elsevier.

Khoei, A. R. (2015), *Extended Finite Element Method: Theory and Applications*.

Koopmans, R. W. R. and Miller, R. D. (1966), 'Soil freezing and soil water characteristic curves', *Soil Sci. Soc. Am. Proc.* **30**(6), 680–685.

Koven, C. D., Riley, W. J. and Stern, A. (2013), 'Analysis of permafrost thermal dynamics and response to climate change in the CMIP5 earth system models', *Journal of Climate* **26**(6), 1877–1900.

Krane, J. (2007), 'Thermal Modeling with TEMP/W'.

Kurganova, I., Teepe, R. and Loftfield, N. (2007), 'Influence of freeze/thaw events on carbon dioxide emission from soils at different moisture and land use.', *Carbon balance and management* **2**, 2.

Kurylyk, B. L., Hayashi, M., Quinton, W. L., McKenzie, J. M. and Voss, C. I. (2016), 'Influence of vertical and lateral heat transfer on permafrost thaw, peatland landscape transition, and groundwater flow', *Water Resources Research* pp. 1286–1305.

Kurylyk, B. L., MacQuarrie, K. T. B. and McKenzie, J. M. (2014), 'Climate change impacts on groundwater and soil temperatures in cold and temperate regions: Implications, mathematical theory, and emerging simulation tools', *Earth-Science Reviews* **138**, 313–334.

Kurylyk, B. L. and Watanabe, K. (2013), 'The mathematical representation of freezing and thawing processes in variably-saturated, non-deformable soils', *Advances in Water Resources* **60**, 160–177.

Lamontagne-Hallé, P., McKenzie, J. M., Kurylyk, B. L. and Zipper, S. C. (2018), 'Changing groundwater discharge dynamics in permafrost regions', *Environmental Research Letters* **13**(8).

Langford, J. E., Schincariol, R. A., Nagare, R. M., Quinton, W. and Mohammed, A. A. (2019), 'Transient and transition factors in modeling permafrost thaw and groundwater flow', *Groundwater* .

Larsen, K. S., Jonasson, S. and Michelsen, A. (2002), 'Repeated freeze-thaw cycles and their effects on biological processes in two arctic ecosystem types', *Applied Soil Ecology* **21**(3), 187–195.

Lawrence, D., Fisher, R., Koven, C., Oleson, K., Swenson, S., Vertenstein, M., Andre, B., Bonan, G., Ghimire, B., van Kampenhout, L., Kennedy, D., Kluzek, E., Knox, R., Lawrence, P., Li, F., Li, H., Lombardozzi, D. and Yaqi, C. X. (2018), 'CLM5 Documentation', *CLM technical note* .

Lazaridis, A. (1970), 'A numerical solution of the multidimensional solidification (or melting) problem', *International Journal of Heat and Mass Transfer* **13**(9), 1459–1477.

Leblanc, R., Hess, K. M., Gelhar, L. W. and Wood, W. (1991), 'Large-Scale Natural Gradient Tracer Test in Sand and Gravel, Cape Cod, Massachusetts: 1. Experimental Design and Observed Tracer Movement', *Water Resources* **27**(5), 895–910.

Ling, F., Wu, Q., Zhang, T. and Niu, F. (2012), 'Modelling Open-Talik Formation and Permafrost Lateral Thaw under a Thermokarst Lake, Beiluhe Basin, Qinghai-Tibet Plateau', *Permafrost and Periglacial Processes* **23**(4), 312–321.

List, F. and Radu, F. A. (2016), 'A study on iterative methods for solving Richards' equation', *Computational Geosciences* **20**(2), 341–353.

Liu, H. and Lennartz, B. (2018), 'Hydraulic properties of peat soils along a bulk density gradient—A meta study', *Hydrological Processes* **49**(381).

Lunardini, V. J. (1981), *Heat transfer in cold climates*, New York: Van Nostrand Reinhold Co.

Lunardini, V. J. (1985), Freezing of Soil with Phase Change Occuring over a finite temperature zone, *in* 'Proceedings of the 4th international offshore mechanics and arctic engineering symposium', ASM.

Ma, T., Wei, C., Xia, X., Zhou, J. and Chen, P. (2015), 'Soil Freezing and Soil Water Retention Characteristics: Connection and Solute Effects', *Journal of Performance of Constructed Facilities* **31**(1), D4015001.

Mai, J. and Tolson, B. A. (2019), 'Model Variable Augmentation (MVA) for Diagnostic Assessment of Sensitivity Analysis Results', *Water Resources Research* **55**(4), 2631–2651.

Mallants, D., Mohanty, B. P., Jacques, D. and Feyen, J. (1996), 'Spatial variability of hydraulic properties in a multi-layered soil profile', *Soil Science* **161**(3), 167–181.

McClymont, A. F., Hayashi, M., Bentley, L. R. and Christensen, B. S. (2013), 'Geophysical imaging and thermal modeling of subsurface morphology and thaw evolution of discontinuous permafrost', *Journal of Geophysical Research: Earth Surface* **118**(3), 1826–1837.

McKenzie, J. M., Voss, C. I. and Siegel, D. I. (2007), 'Groundwater flow with energy transport and water-ice phase change: Numerical simulations, benchmarks, and application to freezing in peat bogs', *Advances in Water Resources* **30**(4), 966–983.

Merle, R. and Dolbow, J. (2002), 'Solving thermal and phase change problems with the eXtended finite element method', *Computational Mechanics* **28**(5), 339–350.

Miller, G. E. (2012), Chapter 14 - Biomedical Transport Processes, *in* J. D. Enderle and J. D. Bronzino, eds, 'Introduction to Biomedical Engineering (Third Edition)', third edit edn, Biomedical Engineering, Academic Press, Boston, pp. 937–993.

Miller, R. (1990), Scaling of Freezing Phenomena in Soils, *in* 'Applications of Soil Physics', Soil Science Society of America, pp. 254–299.

Moës, N., Dolbow, J. and Belytschko, T. (1999), 'A finite element method for crack growth without remeshing', *International Journal for Numerical Methods in Engineering* **46**(1), 131–150.

Mohanty, B. P., Kanwar, R. S. and Horton, R. (1991), 'A Robust-Resistant Approach to Interpret Spatial Behavior of Saturated Hydraulic Conductivity of a Glacial Till Soil Under No-Tillage System', *Water Resources Research* **27**(11), 2979–2992.

More, J. J. and Sorensen, D. C. (1983), 'Computing a Trust Region Step', *SIAM Journal on Scientific and Statistical Computing* **4**(3), 553–572.

Morgan, K., Lewis, R. W. and Zienkiewicz, O. C. (1978), 'An improved algrorithm for heat conduction problems with phase change', *International Journal for Numerical Methods in Engineering* **12**(7), 1191–1195.

Nedjar, B. (2002), 'An enthalpy-based finite element method for nonlinear heat problems involving phase change', *Computers & Structures* **80**(1), 9–21.

Nocedal, J. and Wright, S. J. (2006), *Numerical Optimization*, Springer.

Nourgaliev, R., Luo, H., Weston, B., Anderson, A., Schofield, S., Dunn, T. and Delplanque, J. P. (2016), 'Fully-implicit orthogonal reconstructed Discontinuous Galerkin method for fluid dynamics with phase change', *Journal of Computational Physics* **305**, 964–996.

Olea, R. A. (1991), *Geostatistical glossary and multilingual dictionary*, Oxford University Press.

Oztas, T. and Fayetorbay, F. (2003), 'Effect of freezing and thawing processes on soil aggregate stability', *Catena* **52**(1), 1–8.

Painter, S. L., Coon, E. T., Atchley, A. L., Berndt, M., Garimella, R., Moulton, J. D., Svyatskiy, D. and Wilson, C. J. (2016), 'Integrated surface/subsurface permafrost thermal hydrology: Model formulation and proof-of-concept simulations', *Water Resources Research* **52**(8), 6062–6077.

Pop, I. S., Radu, F. and Knabner, P. (2004), 'Mixed finite elements for the Richards' equation: Linearization procedure', *Journal of Computational and Applied Mathematics* **168**(1-2), 365–373.

Provatas, N., Goldenfeld, N. and Dantzig, J. (1998), 'Adaptive Mesh Refinement Computation of Solidification Microstructures using Dynamic Data Structures', **290**, 265–290.

Qi, J., Vermeer, P. A. and Cheng, G. (2006), 'A Review of the Influence of Freeze-thaw Cycles on Soil Geotechnical Properties', *Permafrost and Periglacial Processes* **136**(17), 245–252.

Quinton, W., Berg, A., Braverman, M., Carpino, O., Chasmer, L., Connon, R., Craig, J., Devoie, É., Hayashi, M., Haynes, K., Olefeldt, D., Pietroniro, A., Rezanezhad, F., Schincariol, R. and Sonnentag, O. (2018), 'A Synthesis of Three Decades of Eco-Hydrological Research at Scotty Creek, NWT, Canada', *Hydrology and Earth System Sciences Discussions* pp. 1–36.

Quinton, W. L. and Baltzer, J. L. (2013), 'The active-layer hydrology of a peat plateau with thawing permafrost (Scotty Creek, Canada)', *Hydrogeology Journal* **21**(1), 201–220.

Quinton, W. L., Hayashi, M. and Chasmer, L. E. (2009), 'Peatland hydrology of discontinuous permafrost in the northwest territories: Overview and synthesis', *Canadian Water Resources Journal* **34**(4), 311–328.

Quinton, W. L., Shirazi, T., Carey, S. K. and Pomeroy, J. W. (2005), 'Soil water storage and active-layer development in a sub-alpine Tundra hillslope, southern Yukon Territory, Canada', *Permafrost and Periglacial Processes* **16**(4), 369–382.

Rathjen, K. A. and Jiji, L. M. (1971), 'Heat Conduction With Melting or Freezing in a Corner', *Journal of Heat Transfer* **93**(1), 101.

Reddy, J. N. J. N. and Gartling, D. K. (2010), *The finite element method in heat transfer and fluid dynamics*, CRC Press.

Rehfeldt, K. R., Boggs, J. M. and Gelhar, L. W. (1992), 'Field study of dispersion in a heterogeneous aquifer: 3. Geostatistical analysis of hydraulic conductivity', *Water Resources Research* **28**(12), 3309–3324.

Rowland, J. C., Travis, B. J. and Wilson, C. J. (2011), 'The role of advective heat transport in talik development beneath lakes and ponds in discontinuous permafrost', *Geophysical Research Letters* **38**(L17504), 1–5.

Rubio, C. M., Josa, R. and Ferrer, F. (2011), 'Influence of the Hysteretic Behaviour on Silt Loam Soil Thermal Properties', *Open Journal of Soil Science* **01**(03), 77–85.

Rühaak, W., Anbergen, H., Grenier, C., McKenzie, J., Kurylyk, B. L., Molson, J., Roux, N. and Sass, I. (2015), 'Benchmarking Numerical Freeze/Thaw Models', *Energy Procedia* **76**, 301–310.

Russo, D. and Bresler, E. (1981), 'Soil Hydraulic Properties as Stochastic Processes: I. An Analysis of Field Spatial Variability', *Soil Science Society of America Journal* **45**(4), 682.

Saltelli, A. (2002), 'Making best use of model evaluations to compute sensitivity indices', *Computer Physics Communications* **145**(2), 280–297.

Saltelli, A., Annoni, P., Azzini, I., Campolongo, F., Ratto, M. and Tarantola, S. (2010), 'Variance based sensitivity analysis of model output. Design and estimator for the total sensitivity index', *Computer Physics Communications* **181**(2), 259–270.

Saltelli, A., Ratto, M., Andres, T., Campolongo, F., Cariboni, J., Gatelli, D., Saisana, M. and Tarantola, S. (2008), *Global Sensitivity Analysis. The Primer*, John Wiley & Sons, Ltd.

Saltelli, A. and Sobol', I. M. (1995), 'Sensitivity analysis for nonlinear mathematical models: numerical experience (in Russian)', *Mathematical models and computer experiment* **7**(11), 16–28.

Salvatori, L. and Tosi, N. (2009), 'Stefan problem through extended finite elements: Review and further investigations', *Algorithms* **2**(3), 1177–1220.

Schilling, O. S., Park, Y. J., Therrien, R. and Nagare, R. M. (2019), 'Integrated Surface and Subsurface Hydrological Modeling with Snowmelt and Pore Water Freeze–Thaw', *Groundwater* **57**(1), 63–74.

Schneider, S., Hoelzle, M. and Hauck, C. (2012), 'Influence of surface and subsurface heterogeneity on observed borehole temperatures at a mountain permafrost site in the Upper Engadine, Swiss Alps', *Cryosphere* **6**(2), 517–531.

Schuur, E. a. G., Bockheim, J., Canadell, J. P., Euskirchen, E., Field, C. B., Goryachkin, S. V., Kuhry, P., Lafleur, P. M., Lee, H., Mazhitova, G., Nelson, F. E., Rinke, A., Romanovsky, V. E., Shiklomanov, N., Tarnokai, C., Venevsky, S., Vogel, J. G. and Zimov, S. a. (2008), 'Vulnerability of permafrost carbon to climate change: Implications for the global carbon cycle', *BioScience* **58**(8), 701–714.

Schuur, E. A. G., McGuire, A. D., Schädel, C., Grosse, G., Harden, J. W., Hayes, D. J., Hugelius, G., Koven, C. D., Kuhry, P., Lawrence, D. M., Natali, S. M., Olefeldt, D., Romanovsky, V. E., Schaefer, K., Turetsky, M. R., Treat, C. C. and Vonk, J. E. (2015), 'Climate change and the permafrost carbon feedback', *Nature* **520**(7546), 171–179.

Sethian, J. A. (1999), *Level Set Methods and Fast Marching Methods*, 2nd edn, Cambridge Monographs on Applied and Computational Mathematics (No. 3), University of California, Berkeley.

Shen, P. Y., Pollack, H. N., Huang, S. and Wang, K. (1995), 'Effects of subsurface heterogeneity on the inference of climate change from borehole temperature data: model studies and field examples from Canada', *Journal of Geophysical Research* **100**(B4), 6383–6396.

Signorelli, S., Bassetti, S., Pahud, D. and Kohl, T. (2007), 'Numerical evaluation of thermal response tests', *Geothermics* **36**(2), 141–166.

Simms, R. B. (2012), The effects of soil heterogeneity on the performance of horizontal ground loop heat exchangers, Master's thesis, University of Waterloo.

Simms, R. B., Haslam, S. R. and Craig, J. R. (2014), 'Impact of soil heterogeneity on the functioning of horizontal ground heat exchangers', *Geothermics* **50**, 35–43.

Šimunek, J., Šejna, M., Saito, H., Sakai, M. and van Genuchten, M. T. (1998), The HYDRUS-1D Software Package for Simulating the One-Dimensional Movement of Water, Heat, and Multiple Solutes in Variably-Saturated Media, Technical report, Department of Environmental Sciences, University of California Riverside, Riverside, California.

Skrzypczak, T., Wegrzyn-Skrzypczak, E. and Węgrzyn-Skrzypczak, E. (2012), 'Mathematical and numerical model of solidification process of pure metals', *International Journal of Heat and Mass Transfer* **55**(15-16), 4276–4284.

Slater, A. G. and Lawrence, D. M. (2013), 'Diagnosing present and future permafrost from climate models', *Journal of Climate* **26**(15), 5608–5623.

Smerdon, B. D. and Mendoza, C. A. (2010), 'Hysteretic freezing characteristics of riparian peatlands in the Western Boreal forest of Canada', *Hydrological Processes* **24**(8), 1027–1038.

Sobol, I. M. (1976), 'Uniformly distributed sequences with an additional uniform property', *USSR Computational Mathematics and Mathematical Physics* **16**(5), 236–242.

Solomon, A. D. (1966), 'Some Remarks on the Stefan Problem', *Mathematics of Computation* **20**, 347–360.

Spaans, E. J. A. and Baker, J. M. (1996), 'The Soil Freezing Characteristic: Its Measurement and Similarity to the Soil Moisture Characteristic', *Soil Science Society of America Journal* **60**(1), 13.

Swaminathan, C. R. and Voller, V. R. (1992), 'A general enthalpy method for modeling solidification processes', *Metallurgical Transactions B* **23**(5), 651–664.

Tang, Y. and Yan, J. (2014), 'Effect of freeze-thaw on hydraulic conductivity and microstructure of soft soil in Shanghai area', *Environmental Earth Sciences* pp. 7679–7690.

Teepe, R., Brumme, R. and Beese, F. (2001), 'Nitrous oxide emissions from soil during freezing and thawing periods', *Soil Biology and Biochemistry* **33**(9), 1269–1275.

Tester, J. W. and Modell, M. (1997), *Thermodynamics and Its Applications*, 3rd edn, Prentice Hall PTR.

Tian, H., Wei, C., Wei, H. and Zhou, J. (2014), 'Freezing and thawing characteristics of frozen soils: Bound water content and hysteresis phenomenon', *Cold Regions Science and Technology* **103**, 74–81.

Usowicz, B., Kossowski, J. and Baranowski, P. (1996), 'Spatial variability of soil thermal properties in cultivated fields', *Soil and Tillage Research* **39**(1-2), 85–100.

Vogel, T., Dohnal, M., Votrubova, J. and Dusek, J. (2019), 'Soil water freezing model with non-iterative energy balance accounting', *Journal of Hydrology* **578**(June), 124071.

Voller, V. R., Cross, M. and Markatos, N. C. (1987), 'An enthalpy method for convection/diffusion phase change', *International Journal for Numerical Methods in Engineering* **24**(1), 271–284.

Voss, C. (1984), 'A Finite-Element Simulation Model for Saturated-Unsaturated, Fluid-Density-Dependent Groundwater Flow with Energy Transport or Chemically-Reactive Single-Species Solute Transport', *U.S. Geological Survey* p. 409.

Walvoord, M. A. and Kurylyk, B. L. (2016), 'Hydrologic Impacts of Thawing Permafrost - A Review', *Vadose Zone Journal* **15**(6), 0.

Walvoord, M. a., Voss, C. I. and Wellman, T. P. (2012), 'Influence of permafrost distribution on groundwater flow in the context of climate-driven permafrost thaw: Example from Yukon Flats Basin, Alaska, United States', *Water Resources Research* **48**(7), 1–17.

Wang, G., Hu, H. and Li, T. (2009), 'The influence of freeze/thaw cycles of active soil layer on surface runoff in a permafrost watershed', *Journal of Hydrology* **375**(3-4), 438–449.

Watanabe, K. and Mizoguchi, M. (2002), 'Amount of unfrozen water in frozen porous media saturated with solution', *Cold Regions Science and Technology* **34**(2), 103–110.

Wheeler, A. A., Boettinger, W. J. and McFadden, G. B. (1992), 'Phase-field model for isothermal phase transitions in binary alloys', *Physical Review A* **45**(10), 7424–7439.

White, D., Hinzman, L., Alessa, L., Cassano, J., Chambers, M., Falkner, K., Francis, J., Gutowski, W. J., Holland, M., Max Holmes, R., Huntington, H., Kane, D., Kliskey, A., Lee, C., McClelland, J., Peterson, B., Scott Rupp, T., Straneo, F., Steele, M., Woodgate, R., Yang, D., Yoshikawa, K. and Zhang, T. (2007), 'The arctic freshwater system: Changes and impacts', *Journal of Geophysical Research: Biogeosciences* **112**(4), 1–21.

White, M. D. and Oostrom, M. (2006), 'STOMP Subsurface Transport Over Multiple Phase'.

Williams, P. J. (1964), 'Unfrozen Water Content of Frozen Soils and Soil Moisture Suction', *Géotechnique* **14**(3), 231–246.

Williams, P. J. and Smith, M. (1989), *The Frozen Earth*, 1 edn, Cambridge University Press.

Wood, E. F., Sivapalan, M., Beven, K. and Band, L. (1988), 'Effects of spatial variability and scale with implications to hydrologic modeling', *Journal of Hydrology* **102**(1-4), 29–47.

Woodbury, A. D. and Sudicky, E. A. (1991), 'The geostatistical characteristics of the borden aquifer', *Water Resources Research* **27**(4), 533–546.

Wu, Q. and Zhang, T. (2010), 'Changes in active layer thickness over the Qinghai-Tibetan Plateau from 1995 to 2007', *Journal of Geophysical Research* **115**(D9), D09107.

Zhang, T., Barry, R. G., Knowles, K., Heginbottom, J. A. and Brown, J. (1999), 'Statistics and characteristics of permafrost and ground-ice distribution in the Northern Hemisphere', *Polar Geography* **23**(2), 132–154.

Zhang, Y., Chen, W. J. and Cihlar, J. (2003), 'A process-based model for quantifying the impact of climate change on permafrost thermal regimes', *Journal of Geophysical Research-Atmospheres* **108**(D22), 4695.

Zheng, X., Babaee, H., Dong, S., Chryssostomidis, C. and Karniadakis, G. E. (2015), 'A phase-field method for 3D simulation of two-phase heat transfer', *International Journal of Heat and Mass Transfer* **82**, 282–298.

Zhou, X., Zhou, J., Kinzelbach, W. and Stauffer, F. (2014), 'Simultaneous measurement of unfrozen water content and ice content in frozen soil using gamma ray attenuation and TDR', *Water Resources Research* **50**(12), 9630–9655.

Zimov, S. a. and Schuur, E. a. G. (2006), 'Permafrost and the Global Carbon Budget', *Science* **312**(June), 1612–1613.

APPENDICES

Appendix A

Sharp interface model

This chapter thoroughly describes two methods of simulating the two-phase permafrost problem: the extended finite element method (XFEM) and enthalpy method. The formulations of both methods are derived for a fully saturated conditions. Special treatments is needed for capturing the phase-interface (in XFEM) or slushy zone (in enthalpy method) when modeling permafrost systems.

A.1 The XFEM model

Discontinuities within the problem's domain can be captured by several methods and techniques, one of which is the XFEM. This method is one of the most common numerical methods for simulating discontinuous media. The idea, which was originally presented by Belytschko and Black (1999) and Moës et al. (1999) for elastic crack propagation, primarily relies on enhancing the approximations of a continuous function for a discontinuous space by adding discontinuous enrichment functions. This method enables the discontinuity to arbitrarily find its path within the element. There are two types of discontinuities: weak and strong. In the former type, the primary variable (e.g., temperature) is continuous, but its gradients are discontinuous, e.g., in problems with phase change. Strong discontinuity refers to a discontinuity in the primary variable, e.g., problems involving crack propagation or contact between two interface. Regarding these definitions, the permafrost problem involves weak discontinuity; thus, the appropriate enrichment function is the Signed Distance Function, which creates a jump in the temperature gradient field as would exist at the ice-water interface. The XFEM approximation of the temperature field can be written

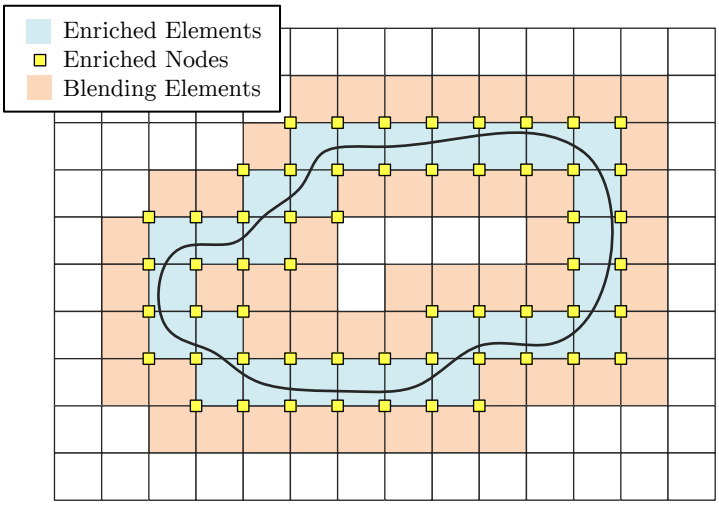

Figure A.1 Overview of XFEM

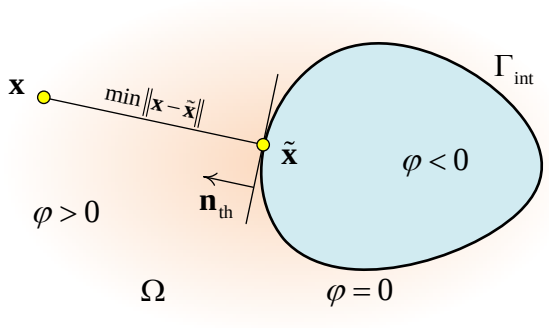

Figure A.2 Signed Distance Function

as

$$T(\mathbf{x},\, t) = \sum_{I \in \mathcal{N}} N^I_{\text{std}}(\mathbf{x})\, \overline{T}^I_{\text{std}}(t) + \sum_{J \in \mathcal{M}} \underbrace{N^I_{\text{enr}}\left(|\varphi(\mathbf{x})| - \left|\varphi\left(\mathbf{x}^J\right)\right|\right)}_{enriched\ shape\ function} \overline{T}^J_{\text{enr}}(t), \tag{A.1}$$

where $\mathcal{N}$ and $\mathcal{M}$ are the standard and enrichment sets, respectively. The std subscript denotes an association with standard degrees of freedom, and enr subscript denotes values associated with the enriched degrees of freedom. The XFEM setup of a medium with a material interface is shown in Figure A.1, in which the *enriched* and *blending* elements are defined. An element is called enriched if it contains a discontinuity, and, consequently, all of its nodes are enriched; however, blending elements refer to the ones that contains no discontinuity, but they are adjacent to an enriched element. These elements cause stability problems, since the partition of unity would not be satisfied due to that they are partially

enriched. One may implement some techniques to attenuate the blending element issues.

The Signed Distance Function is expressed as

$$\varphi(\mathbf{x}) = \min\|\mathbf{x} - \tilde{\mathbf{x}}\| \operatorname{sign}((\mathbf{x} - \tilde{\mathbf{x}})\cdot\mathbf{n}_{\mathrm{th}}), \tag{A.2}$$

in which $\tilde{\mathbf{x}}$ is a point located on the interface having the minimum distance from the point $\mathbf{x}$, $\|\ \|$ expresses the positive distance of point $\mathbf{x}$ from the interface, Figure A.2.

A.1.1 Weak form and discretization of the equations

In the present work, the finite element and finite difference methods (backward Euler) are employed for the space and time domain discretization, respectively. The weak formulation of the problem is calculated by multiplying the strong form of the problem's PDE, Equation 3.3, by an appropriate trial function δT, which could also be chosen arbitrarily, and integrating it over the problem's domain (Ω).

$$\begin{aligned} \Pi &= \frac{\partial}{\partial t}\left(\overline{\rho c}T\right) - \nabla\cdot\left(\overline{K}\nabla T\right) - \mathrm{h_b}, \\ \delta\Pi &= \int_\Omega \delta T\cdot\left[\frac{\partial}{\partial t}\left(\overline{\rho c}T\right) - \nabla\cdot\left(\overline{K}\nabla T\right) - \mathrm{h_b}\right] d\Omega = 0. \end{aligned} \tag{A.3}$$

After implementing Gauss-Green theorem, the weak form of the problem is calculated as

$$\begin{aligned} \int_\Omega \delta T\cdot\left[\frac{\partial}{\partial t}\left(\overline{\rho c}T\right)\right] d\Omega + \int_\Omega \nabla\left(\delta T\right)\cdot\overline{K}\nabla T d\Omega - \int_\Gamma \delta T\cdot\left(\overline{K}\nabla T\cdot n\right) d\Gamma_N \\ + \int_\Omega \delta T\cdot \mathrm{h_b} d\Omega = 0, \end{aligned} \tag{A.4}$$

let $\overline{K}\nabla T\cdot n = -\tilde{\mathbf{q}}$, $\delta T = \mathbf{N}\delta\overline{\mathbf{T}}$, $T = \mathbf{N}\overline{\mathbf{T}}$, $\nabla\mathbf{N} = \mathbf{B}$, and

$$\begin{aligned} \delta\overline{\mathbf{T}}^{\mathrm{T}}\left[\int_\Omega \left(\mathbf{N}^t\right)^{\mathrm{T}}\left[\frac{\left(\overline{\rho c}\mathbf{N}\overline{\mathbf{T}}\right)^t - \left(\overline{\rho c}\mathbf{N}\overline{\mathbf{T}}\right)^{t-1}}{\Delta t}\right] d\Omega + \left(\int_\Omega \left(\mathbf{B}^t\right)^{\mathrm{T}}\overline{K}^t\mathbf{B}^t d\Omega\right)\overline{\mathbf{T}} \right. \\ \left. + \int_\Gamma \left(\mathbf{N}^t\right)^{\mathrm{T}}\tilde{\mathbf{q}}^t d\Gamma - \int_\Omega \left(\mathbf{N}^t\right)^{\mathrm{T}}\mathrm{h_b}^t d\Omega\right] = 0, \end{aligned} \tag{A.5}$$

in which $\mathbf{N}$ is the shape function, which contains the enriched shape functions of fully or

partially enriched elements. Finally, the discretized equation is obtained as

$$\frac{\mathbf{C}^t\overline{\mathbf{T}}^t - \tilde{\mathbf{C}}^{t-1}\overline{\mathbf{T}}^{t-1}}{\Delta t} + \mathbf{K}^t\overline{\mathbf{T}}^t - \mathbf{f}^t = 0, \tag{A.6}$$

where

$$\begin{aligned}
\mathbf{C}^t &= \int_\Omega \left(\mathbf{N}^t\right)^{\mathrm{T}} (\overline{\rho c})^t \mathbf{N}^t d\Omega, \\
\tilde{\mathbf{C}}^t &= \int_\Omega \left(\mathbf{N}^t\right)^{\mathrm{T}} (\overline{\rho c})^{t-1} \mathbf{N}^{t-1} d\Omega, \\
\mathbf{K}^t &= \int_\Omega \left(\mathbf{B}^t\right)^{\mathrm{T}} \overline{K}^t \mathbf{B}^t d\Omega, \\
\mathbf{f}^t &= \int_\Omega \left(\mathbf{N}^t\right)^{\mathrm{T}} \mathrm{h}_{\mathrm{b}}^t d\Omega - \int_\Gamma \left(\mathbf{N}^t\right)^{\mathrm{T}} \tilde{\mathbf{q}}^t d\Gamma.
\end{aligned} \tag{A.7}$$

A.1.2 Conditions on the interface

In this method, a Dirichlet boundary condition must be satisfied at the fully frozen and fully thawed soil interface, in which the temperature should be equal to the soil freezing point temperature (T_{f}).

$$T_{\mathrm{int}} = T_{\mathrm{f}} \qquad \text{on } \Gamma_{\mathrm{int}}. \tag{A.8}$$

Equation A.8 denotes that the temperature field is continuous; however, its gradients normal to the surface are discontinuous due to different thermal conductivities, heat capacities, and densities at the two sides of the interface ($\mathbf{x} = \mathbf{x}_{\mathrm{int}}^-$ and $\mathbf{x} = \mathbf{x}_{\mathrm{int}}^+$). This condition may be applied using various methods, such as, Penalty, Lagrange multipliers, augmented Lagrange multipliers, or Nitsche methods. Here, the Lagrange multipliers method has been implemented.

Lagrange multipliers method

In this method, the interface condition is exactly applied by introducing new degrees of freedom called the *Lagrange multipliers*. In order to apply this method to the XFEM formulation, the problem is posed as a potential energy minimization problem, where the total potential energy is given by $\overline{\Pi}$. In this manner, the interface condition is defined as

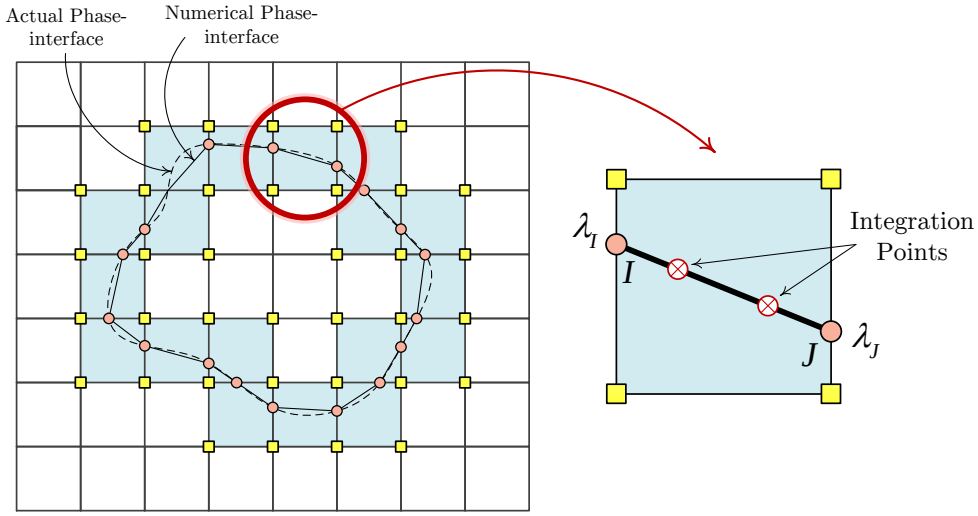

Figure A.3 Lagrange degrees of freedom

$g_{\text{int}}\left(\overline{T}^t\right) = 0$, where

$$\begin{aligned} g_{\text{int}}\left(\overline{T}^t\right) &= \overline{T}\left(\mathbf{x}_{\text{int}}^t, t\right) - T_{\text{f}}, \\ &= \overline{\text{N}}\left(\mathbf{x}_{\text{int}}^t, t\right) \overline{\mathbf{T}}^t - T_{\text{f}}. \end{aligned} \tag{A.9}$$

Since the interface is a line, a one-dimensional shape function ($\overline{\text{N}}$) is required to estimate the temperature at any point on the interface using the nodal values of the interface (λ_I and λ_J in Figure A.3).

To determine the system's potential energy due to the interface constraint, a constraint functional is defined as

$$\Pi^{\text{int}} = \int_{\Gamma_{\text{int}}} \lambda_{\text{int}} g_{\text{int}}\left(\overline{T}^t\right) d\Gamma, \tag{A.10}$$

where λint is the Lagrange multiplier at the interface calculated based on the Lagrange degrees of freedom. By adding the constraint functional to the potential energy of the system, the system's total potential energy would become

$$\overline{\Pi} = \Pi + \Pi^{\text{int}} \equiv \Pi + \int_{\Gamma_{\text{int}}} \lambda_{\text{int}} g_{\text{int}}\left(\overline{T}^t\right) d\Gamma. \tag{A.11}$$

Equations A.6 and A.7 represent the fully discrete formulation of a conductive heat

transfer problem. The phase-interface condition, Equation A.8, must be expressed in a discrete form as well. To achieve this, $\overline{\Pi}$ must be minimized, which can be done by taking the variation from Equation A.11. This leads to

$$\begin{aligned}\overline{\Pi} &= \delta\Pi + \int_{\Gamma_{\text{int}}} \delta\lambda_{\text{int}} g_{\text{int}} d\Gamma + \int_{\Gamma_{\text{int}}} \lambda_{\text{int}} \delta g_{\text{int}} d\Gamma \\ &= \delta\Pi + \delta\overline{\lambda}^{\text{T}} \int_{\Gamma_{\text{int}}} \left(\text{N}^t\right)^{\text{T}} \left(\overline{\text{N}}^t \overline{\mathbf{T}}^t - T_{\text{f}}\right) d\Gamma + \delta\overline{\mathbf{T}}^{\text{T}} \int_{\Gamma_{\text{int}}} \left(\overline{\text{N}}^t\right)^{\text{T}} \text{N}^t \overline{\lambda}^t d\Gamma = 0.\end{aligned} \tag{A.12}$$

Combining Equation A.12 with Equation A.6 gives the final linear system of equations as follows:

$$\begin{bmatrix} \overline{\mathbf{K}}^t & \left(\mathbf{K}_{\text{int}}^t\right)^{\text{T}} \\ \mathbf{K}_{\text{int}}^t & 0 \end{bmatrix} \begin{Bmatrix} \overline{\mathbf{T}}^t \\ \overline{\lambda}^t \end{Bmatrix} = \begin{Bmatrix} \overline{\mathbf{F}}^t \\ \mathbf{F}_{\text{f}}^t \end{Bmatrix}, \tag{A.13}$$

where

$$\overline{\mathbf{K}}^t = \mathbf{K}^t + \frac{1}{\Delta t}\mathbf{C}^t, \tag{A.14}$$

$$\overline{\mathbf{F}}^t = \mathbf{f}^t + \frac{1}{\Delta t}\widetilde{\mathbf{C}}^t \overline{\mathbf{T}}^{t-1}, \tag{A.15}$$

$$\mathbf{K}_{\text{int}}^t = \int_{\Gamma_{\text{int}}} \left(\text{N}^t\right)^{\text{T}} \overline{\text{N}}^t d\Gamma, \tag{A.16}$$

$$\mathbf{F}_{\text{f}}^t = \int_{\Gamma_{\text{int}}} \left(\text{N}^t\right)^{\text{T}} T_{\text{f}} d\Gamma. \tag{A.17}$$

This results in a solution which is constrained such that the condition $g_{\text{int}}\left(\overline{T}^t\right) = 0$ is always met.

A.1.3 Level set method

To capture the evolution of the interface, the level set method is used. The idea behind this method in a bi-material case is to apply the Signed Distance Function to the space where the material interface exists. At the end of each timestep, the level set will be updated to determine the new interface location (Khoei, 2015). This method is schematically shown in Figure A.4. To calculate the new location of the interface, an appropriate algorithm is needed to update the level set function. This is done by setting the material derivative of

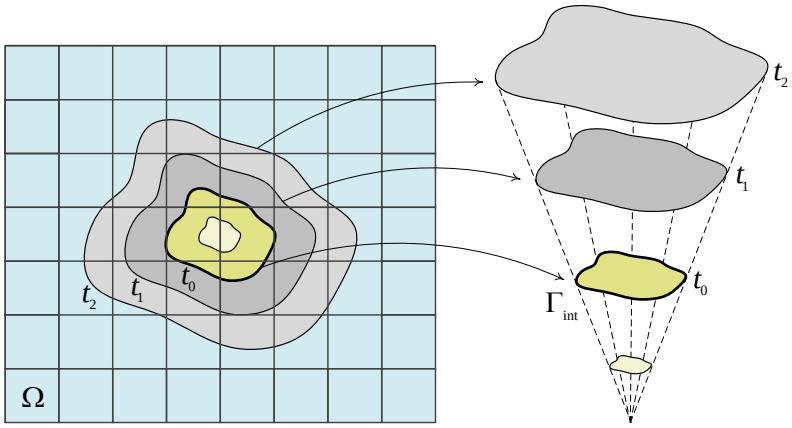

Figure A.4 Overview of the level set method

the level set function $\varphi(\mathbf{x})$ equal to zero, which is expressed as

$$\begin{aligned} \frac{D\varphi}{Dt} &= 0, \\ \frac{\partial\varphi}{\partial t} + \mathbf{v}\cdot\nabla\varphi &= 0, \end{aligned} \tag{A.18}$$

where $\mathbf{v}$ is the generalized interface velocity that advects the interface, which, in phase change problems, is the phase-interface. While the generalized interface velocity is meaningful at the interface only, it can be defined for the entirety of an artificial domain which contains the interface. Since $V_\varphi = \mathbf{n}\cdot\mathbf{v} = \frac{\nabla\varphi}{|\nabla\varphi|}\cdot\mathbf{v}$, Equation A.18 can be expressed in terms of the normal velocity:

$$\frac{\partial\varphi}{\partial t} + V_\varphi\,|\nabla\varphi| = 0. \tag{A.19}$$

Normal speed field V_φ

Calculation of the normal speed field V_φ is based on the conventional assumption that the gradients V_φ and φ are orthogonal (Sethian, 1999; Adalsteinsson and Sethian, 1999). Hence, V_φ can be defined as the following PDE:

$$\mathrm{sign}(\varphi)\,\nabla V_\varphi\cdot\nabla\varphi = 0. \tag{A.20}$$

Equation A.20 is solvable with the following boundary condition

$$V_{\varphi}(\mathbf{x}_{\text{int}}, t) = v \quad \text{on } \Gamma_{\text{int}}, \tag{A.21}$$

in which v is the interface velocity. An energy balance equation (the Stefan condition) is required to allocate the interface position and control its speed. The Stefan condition is applied on Γ_{int} and is defined such that the jump in conductive heat flow across the interface is equal to the latent heat consumed with progression of that interface, i.e.,

$$\begin{aligned} \rho L_{\text{f}} v &= -[\![q]\!] \\ &= -[\![K \nabla T]\!] \\ &= (K_{\text{th}} \nabla T_{\text{th}} - K_{\text{fr}} \nabla T_{\text{fr}}) \cdot \mathbf{n}_{\text{fr}}, \end{aligned} \tag{A.22}$$

where ρ is the water density, L_{f} is the latent heat of fusion, v is the speed of the interface progression. The subscripts th and fr denotes values at the fully thawed and fully frozen side of the interface, respectively. The unit vector outwardly perpendicular to the frozen phase is denoted by $\mathbf{n}_{\text{fr}}$.

A.2 The enthalpy model

Enthalpy is a thermodynamic quantity which represents the total heat energy of a system. In this method, the phase-interface is calculated as a part of solution; thus, explicit tracking of the interface is not needed. It is historically interesting that, this method was not originally introduced for simulating phase change; however, it was introduced by Eyres et al. (1946) as an alternative formulation for heat conduction problems with varying thermal conductivity.

The energy conservation equation expressed in enthalpy formulation may be written as

$$\frac{\partial H}{\partial t} + \nabla \cdot (\tilde{\mathbf{v}} H) = -\nabla \cdot \tilde{\mathbf{q}} + \text{h}_{\text{b}}, \tag{A.23}$$

$$\tilde{\mathbf{q}} = -\overline{K} \nabla T, \tag{A.24}$$

in which the enthalpy (H) of the system is defined as

$$H(T) = \int_{T_0}^{T} \overline{\rho c}(T)\, T dT. \tag{A.25}$$

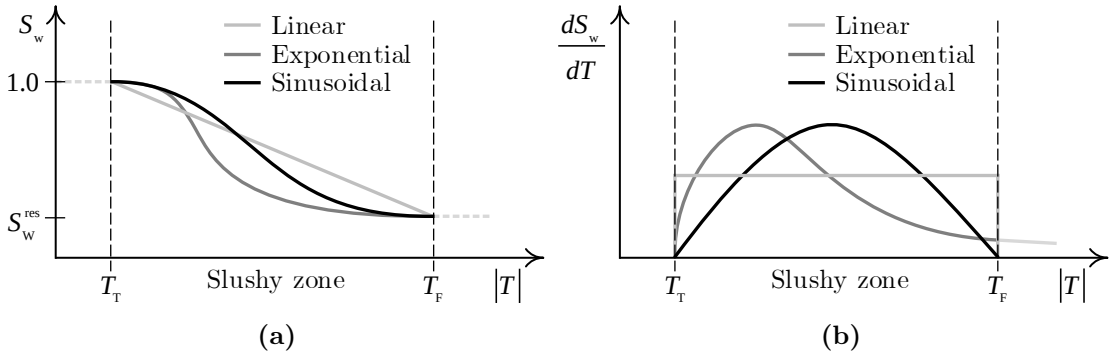

Figure A.5 Soil freezing functions: (a) Freezing functions, (b) Derivatives of the functions

In Equations A.23 and A.25, $\overline{\rho c}$ and $\overline{K}$ are functions of temperature and, in an arithmetic averaging scheme, are expressed as

$$\overline{\rho c}(T) = n(S_{\mathrm{w}}(T)\,\rho_{\mathrm{w}} c_{\mathrm{w}} + S_{\mathrm{i}}(T)\,\rho_{\mathrm{i}} c_{\mathrm{i}}) + (1-n)\rho_{\mathrm{s}} c_{\mathrm{s}} + n\rho_{\mathrm{i}} L_{\mathrm{f}} \frac{dS_{\mathrm{w}}}{dT} \tag{A.26}$$

$$,\overline{K}(T) = n(S_{\mathrm{w}}(T)\,k_{\mathrm{w}} + S_{\mathrm{i}}(T)\,k_{\mathrm{i}}) + (1-n)k_{\mathrm{s}}, \tag{A.27}$$

where, n, S, ρ, c, and k are the porosity, saturation, density, bulk heat capacity, and thermal conductivity, respectively. The w, i, and s subscripts denote the parameters of water, ice, and soil phases. Note the last term in Equation A.26, which regards the latent heat capacity in the phase change process.

The relation between water saturation and temperature is defined by the soil freezing function, $S_{\mathrm{w}}(T)$, which defines a relationship between water saturation and temperature. The two non-hysteretic commonly used freezing functions (Figure A.5) are: linear and Gaussian functions (McKenzie et al., 2007). The linear freezing function, which denotes the simplest criteria of soil freezing, can be defined as follows:

$$S_{\mathrm{w}}(T) = \begin{cases} bT + 1 & T > T_{\mathrm{res}} \\ \\ S_{\mathrm{w}}^{\mathrm{res}} & T \leqslant T_{\mathrm{res}} \end{cases}, \tag{A.28}$$

where b is the slope of the linear function, $S_{\mathrm{w}}^{\mathrm{res}}$ is the residual water saturation, and T_{res} is the temperature at which the water saturation reaches its residual value. Accordingly, the

derivative of this linear function follows

$$\frac{dS_{\mathrm{w}}}{dT}(T) = \begin{cases} b & T > T_{\mathrm{res}} \\ 0 & T \leqslant T_{\mathrm{res}} \end{cases} . \tag{A.29}$$

The Gaussian freezing function, which is a smooth differentiable function, and its derivative with respect to temperature are defined as

$$S_{\mathrm{w}}(T) = (1 - S_{\mathrm{w}}^{\mathrm{res}}) \exp\left[-\left(\frac{T - T_{\mathrm{f}}}{\beta}\right)^2\right] + S_{\mathrm{res}}, \tag{A.30}$$

$$\frac{dS_{\mathrm{w}}}{dT}(T) = -2\,(1 - S_{\mathrm{w}}^{\mathrm{res}})\,\frac{T - T_{\mathrm{f}}}{\beta^2} \exp\left[-\left(\frac{T - T_{\mathrm{f}}}{\beta}\right)^2\right], \tag{A.31}$$

where T_{f} is the porewater freezing point, and β is a fitting parameter that defines the temperature range of slushy zone.

To avoid numerical issues, it is better to use a smooth and differentiable freezing function. Since the linear freezing function contains a non-differentiable point (at $T = T_{\mathrm{res}}$), the exponential form of the freezing function is often preferable. In chapter 3, a theoretical justification for the fitting parameter of the Gaussian freezing function is provided.

Appendix B

Generating heterogeneous field realization using GSLIB

Geostatistical software library (GSLIB) is an open source computer program written in FORTRAN. One can use this program to quantify spatial variability of existing fields using Geostatistics or generate random fields with specified Geostatistical properties. The list of the subroutines used in the process of generating a spatially correlated field is listed in Table B.1

For the ease of the reader, the descriptions of the subroutines and required parameters are simply copied here from the help page of GSLIB's official website (*GSLIB Help Page: Programs - http://www.gslib.com/gslib_help/programs.html*, n.d.).

Table B.1 The name and version number of the GSLIB subroutines deployed in this research

Subroutine name	Version number
SGSIM	3.001
VMODEL	2.905
GAM	2.905
ADDCOORD	2.905
VARGPLT	2.906

GSLIB Help Page: SGSIM

Description:

- Sequential Gaussian simulation program

Parameters:

- **datafl:** the input data in a simplified Geo-EAS formatted file. If this file does not exist then an unconditional simulation will be generated.
- **icolx, icoly, icolvr, icolwt** and **icolsec:** the column numbers for the *x,y* and *z* coordinates, the variable to be simulated, the declustering weight, and the secondary variable (e.g., for external drift if used). One or two of the coordinate column numbers can be set to zero which indicates that the simulation is 2-D or 1-D. For equal weighting, set **icolwt** to zero.
- **tmin** and **tmax:** all values strictly less than **tmin** and strictly greater than **tmax** are ignored.
- **itrans:** if set to 0 then no transformation will be performed; the variable is assumed already standard normal (the simulation results will also be left unchanged). If **itrans=1**, transformations are performed.
- **transfl:** output file for the transformation table if transformation is required (**igauss**=0).
- **ismooth:** if set to 0, then the data histogram, possibly with declustering weights is used for transformation, if set to 1, then the data are transformed according to the values in another file (perhaps from histogram smoothing).
- **smthfl:** file with the values to use for transformation to normal scores (if **ismooth** is set to 0).
- **icolvr** and **icolwt:** columns in **smthfl** for the variable and the declustering weight (set to 1 and 2 if **smthfl** is the output from `histsmth`).
- **zmin** and **zmax** the minimum and maximum allowable data values. These are used in the back transformation procedure.
- **ltail** and **ltpar** specify the back transformation implementation in the lower tail of the distribution: **ltail**=1 implements linear interpolation to the lower limit **zmin**, and **ltail**=2 implements power model interpolation, with **w=ltpar**, to the lower limit **zmin**.
- The middle class interpolation is linear.
- **utail** and **utpar** specify the back transformation implementation in the upper tail of the distribution: **utail**=1 implements linear interpolation to the upper limit **zmax**, **utail**=2 implements power model interpolation, with **w=utpar**, to the upper limit **zmax**, and **utail**=4 implements hyperbolic model extrapolation with **w=utpar**. The hyperbolic tail extrapolation is limited by **zmax**.
- **idbg:** an integer debugging level between 0 and 3. The larger the debugging level the more information written out.
- **dbgfl:** the file for the debugging output.
- **outfl:** the output grid is written to this file. The output file will contain the results, cycling fastest on *x* then *y* then *z* then simulation by simulation.
- **nsim:** the number of simulations to generate.
- **nx, xmn, xsiz:** definition of the grid system (*x* axis).
- **ny, ymn, ysiz:** definition of the grid system (*y* axis).
- **nz, zmn, zsiz:** definition of the grid system (*z* axis).
- **seed:** random number seed (a large odd integer).
- **ndmin** and **ndmax:** the minimum and maximum number of original data that should be used to simulate a grid node. If there are fewer than **ndmin** data points the node is not simulated.
- **ncnode:** the maximum number of previously simulated nodes to use for the simulation of another node.

- **sstrat:** if set to 0, the data and previously simulated grid nodes are searched separately: the data are searched with a super block search and the previously simulated nodes are searched with a spiral search (see section II.4). If set to 1, the data are relocated to grid nodes and a spiral search is used and the parameters **ndmin** and **ndmax** are not considered.
- **multgrid:** a multiple grid simulation will be performed if this is set to 1 (otherwise a standard spiral search for previously simulated nodes is considered).
- **nmult:** the number of multiple grid refinements to consider (used only if **multgrid** is set to 1).
- **noct:** the number of original data to use per octant. If this parameter is set less than or equal to 0, then it is not used; otherwise, it overrides the **ndmax** parameter and the data is partitioned into octants and the closest **noct** data in each octant is retained for the simulation of a grid node.
- **radius_hmax**, **radius_hmin** and **radius_vert**: the search radii in the maximum horizontal direction, minimum horizontal direction, and vertical direction (see angles below).
- **sang1, sang2** and **sang3:** the angle parameters that describe the orientation of the search ellipsoid. See the discussion on anisotropy specification associated with Figure II.4.
- **ktype:** the kriging type (0 = simple kriging, 1 = ordinary kriging, 2 = simple kriging with a locally varying mean, 3 = kriging with an external drift, or 4 = collocated cokriging with one secondary variable) used throughout the loop over all nodes. SK is required by theory; only in cases where the number of original data found in the neighborhood is large enough can OK be used without the risk of spreading data values beyond their range of influence
- **rho:** correlation coefficient to use for collocated cokriging (used only if **ktype** = 4).
- **secfl:** the file for the locally varying mean, the external drift variable, or the secondary variable for collocated cokriging (the secondary variable must be gridded at the same resolution as the model being constructed by `sgsim`).
- **nst** and **c0:** the number of semivariogram structures and the isotropic nugget constant.
- For each of the **nst** nested structures one must define **it**, the type of structure; **cc**, the *c* parameter; **ang1,ang2,ang3**, the angles defining the geometric anisotropy; **aa_hmax**, the maximum horizontal range; **aa_hmin**, the minimum horizontal range; and **aa_vert**, the vertical range.

Application notes:

- This program requires standard normal data and writes standard normal simulated values. Normal score transform and back transform are to be performed outside of this program
- Recall that the power model is not a legitimate model for a multiGaussian phenomenon and it is not allowed in `sgsim`
- The semivariogram model is that of the normal scores. The kriging variance is directly interpreted as the variance of the conditional distribution; consequently, the nugget constant **c0** and **c** (sill) parameters should add to 1.0.

B.1 SGSIM parameter file

```
START OF PARAMETERS
nodata
1 2 0 3 5 0                          -columns for X,Y,Z,vr,wt,sec.var.
-1E+21 1E+21
0                                    -transform the data (0=no, 1=yes)
sgsim.trn
0                                    -consider ref. dist (0=no, 1=yes)
vmodel.var
1 2                                  -columns for vr and wt
0 15                                 -zmin,zmax (tail extrapolation)
1 0                                  -lower tail option
1 15                                 -upper tail option
0                                    -debug level (0-3)
GSLIB/outputs/R1_BCSGSIM_nodata.dbg
GSLIB/outputs/R1_BCSGSIM_output.out
1                                    -number of realizations to generate
2001 0 2.500000e-02                  -nx, xmin, xsize
1 0 0.000000e+00                     -ny, ymin, ysize
1 0 1                                -nz, zmin, zsize
443562                               -random number seed
0 8                                  -Min and max original data for sim
12                                   -number of simulated nodes to use
1                                    -assign data to nodes (0=no, 1=yes)
1 3                                  -multiple grid search (0=no, 1=yes), num
0                                    -maximum data per octant (0=not used)
10 10 10                             -maximum search radii (hmax, hmin, vert)
0 0 0                                -angles for search ellipsoid
51 51 11                             -size of covariance lookup table
0 0 1                                -kType: 0=SK,1=OK,2=LVM,3=EXDR,4=COLC
nodata
4                                    -column
1 0                                  -nst, nugget NOFILE
2 1 0 0 0                            -it, cc, ang1, ang2, ang3
3.000000e+00 3.000000e+00 0          -a_hmax, a_hmin, a_vert
```

GSLIB Help Page: VMODEL

Description:

- This program will take the semivariogram model and write out a file with the same format as the `gam` program so that it can be plotted with `vargplt` The primary uses of `vmodel` are to overlay a model on experimental points and also to provide a utility to check the definition of the semivariogram model.

Parameters:

- **outfl:** the output file that will contain the semivariogram values.
- **ndir** and **nlag:** the number of directions and the number of lags to be considered.
- **azm, dip** and **lag:** for each of the **ndir** directions a direction must be specified by **azm** and **dip** and a unit lag offset must be specified (**lag**).
- **nst** and **c0:** the number of structures and the nugget effect.
- For each of the **nst** nested structures one must define **it**, the type of structure; **cc**, the *c* parameter; **ang1,ang2,ang3**, the angles defining the geometric anisotropy; **aa_hmax**, the maximum horizontal range; **aa_hmin**, the minimum horizontal range; and **aa_vert**, the vertical range.

B.2 VMODEL parameter file

```
START OF PARAMETERS:
GSLIB/save/vmodel.var
2 100                                   -Nb structure, Number of lags
90 0 0.25
0 0 0.25
1 0                                     -nst, nugget NOFILE
2 1 0 0 0                               -it, cc, ang1, ang2, ang3
2 12 1                                  -a_hmax, a_hmin, a_vert
```

GSLIB Help Page: GAM

Description:

- Variogram calculation of gridded data

Parameters:

- **datafl:** the input data in a simplified Geo-EAS formatted file. The data are ordered rowwise (x cycles fastest, then y, then z).
- **nvar** and **ivar(1) ... ivar(nvar):** the number of variables and their columns in the data file.
- **tmin** and **tmax:** all values, regardless of which variable, strictly less than **tmin** and greater than or equal to **tmax** are ignored.
- **outfl:** the output variograms are written to a single output file named **outfl** The output file contains the variograms ordered by direction and then variogram type specified in the parameter file (the directions cycle fastest then the variogram number). For each variogram there is a one-line description and then **nlag** lines each with the following:
  - lag number (increasing from 1 to **nlag**
  - average separation distance for the lag.
  - the {\em semivariogram value (whatever type was specified).
  - number of pairs for the lag.
  - mean of the data contributing to the tail.
  - mean of the data contributing to the head.
  - the tail and head variances (for the correlogram).

  The {\tt vargplt program documented in section VI.1.8 may be used to create PostScript displays of multiple variograms.
- **igrid:** the grid or realization number. Recall that realizations or grids are written one after another; therefore, if **igrid=2** the input file must contain at least 2 x **nx** x **ny** x **nz** values and the second set of **nx** x **ny** x **nz** values will be taken as the second grid.
- **nx, xmn, xsiz:** definition of the grid system (*x* axis).
- **ny, ymn, ysiz:** definition of the grid system (*y* axis).
- **nz, zmn, zsiz:** definition of the grid system (*z* axis). One or two dimensional data may be considered by setting the number of nodes in some directions to 1. Often, `gam` is used to check the variogram reproduction of realizations from a simulation program.
- **ndir** and **nlag:** the number of directions and lags to consider. The same number of lags are considered for all directions and all directions are considered for all of the **nvarg** variograms specified below.

- **ixd, iyd** and **izd:** these three arrays specify the unit offsets that define each of the **ndir** directions

Gridded Data

When data are on a regular grid, the directions are specified by giving the number of grid nodes that must be shifted to move from a node on the grid to the next nearest node on the grid that lies along the directional vector. Some examples for a cubic grid:

x shift	y shift	z shift	
1	0	0	aligned along the x axis
0	1	0	aligned along the y axis
0	0	1	aligned along the z axis
1	1	0	horizontal at 45^{o} from y
1	-1	0	horizontal at 135^{o} from y.
1	1	1	dipping at -45^{o}, 225^{o} clockwise from y.

Within the **gam** subroutine the directions are specified by offsets of the form shown above. No direction or lag tolerances are allowed. In some cases this direction definition is too restrictive and may result in not enough pairs being combined. The solution is either to average multiple directions from **gam** with weighting by the number of pairs, or to store the grid as irregularly spaced data and use **gamv** to compute the variograms (at substantially more computational cost).

- **standardize:** if set to 1, the semivariogram values will be divided by the variance
- **nvarg:** the number of variograms to compute.
- The "variogram type" is specified by an integer code
- **ivtail, ivhead** and **ivtype:** for each of the **nvarg** variograms one must specify which variables should be used for the tail and head and which type of variogram is to be computed. For direct variograms the **ivtail** array is identical to the **ivhead** array. Cross variograms are computed by having the tail variable different from the head variable, e.g., if **ivtail(i)** is set to 1, **ivhead(i)** is set to 2, and **ivtype(i)** is set to 2, then distance measure **i** will be a cross semivariogram between variable 1 and variable 2. Note that **ivtype(i)** should be set to something that makes sense (e.g., types 1,2, or 3); a cross relative variogram would be difficult to interpret. Further, note that for the cross semivariogram (**ivtype**=2) the two variables **ivtail** and **ivhead** are used at both the tail and head locations. The **ivtype** variable corresponds to the integer code in the list given in section III.1.
- **cut:** whenever the **ivtype** is set to 9 or 10, i.e., asking for an indicator variogram, then a cutoff must be specified immediately after the **ivtype** parameter on the same line in the input file. Note that if an indicator variogram is being computed then the cutoff/category applies to variable **ivtail(i)** in the input file (although the **ivhead(i)** variable is not used it must be present in the file to maintain consistency with the other variogram types).

Application notes:

- Regularly spaced data in 1-D can be handled by setting *ny, nz* to one and *iyd, izd* to zero.

B.3 GAM parameter file

```
START OF PARAMETERS:
GSLIB/save/R1_SGSIM_output.out
1 1
-1E+21 1E+21                          -trimming limits
GSLIB/save/GR_R1_SGSIM_output.out
1                                     -grid or realization number
201 0 0.25                            -nx, xmin, xsize
201 0 0.25                            -ny, ymin, ysize
1 0 1                                 -nz, zmin, zsize
2 100                                 -number of directions, number of lags
1 0 0                                 -ixd(i),iyd(i),izd(i)
0 1 0                                 -ixd(i),iyd(i),izd(i)
1                                     -standardize Sill? (0=no, 1=yes)
1                                     -number of variograms
1 1 1                                 -Tail var, head var, vario type
```

GSLIB Help Page: ADDCOORD

Description:

- This program adds 3-D coordinates to gridded points in an ordered GSLIB output file (as from kriging or simulation).

Parameters:

- **datafl:** the input gridded data file.
- **outfl:** file for output with *X, Y* and *Z* coordinates.
- **ireal:** the grid or realization number to consider.
- **nx, xmn,** and **xsiz:** the number of nodes in the *x* direction, the origin, and the grid node separation.
- **ny, ymn,** and **ysiz:** the number of nodes in the *y* direction, the origin, and the grid node separation.
- **nz, zmn,** and **zsiz:** the number of nodes in the *z* direction, the origin, and the grid node separation.

B.4 ADDCOORD parameter file

```
Parameters for SGSIM

START OF PARAMETERS
GSLIB/outputs/R1_SGSIM_output.out
GSLIB/outputs/R1_ADDCOOR_output.out
1                                   -realization number to add coordinate
201 0 2.500000e-01                  -nx, xmin, xsize
21 0 2.500000e-01                   -ny, ymin, ysize
1 0 1                               -nz, zmin, zsize
```

GSLIB Help Page: VARGPLT

Description:

- The program `vargplt` takes the special output format used by the variogram programs and creates graphical displays for PostScript display devices. This program is a straightforward display program and does not provide any facility for variogram calculation or model fitting. Good interactive variogram fitting programs are available in the public domain

B.5 VARGPLT parameter file

```
START OF PARAMETERS:
GSLIB/save/VP.ps
4                                   -number of variograms
1 0                                 -distance limits (from Data if max<min)
1 0                                 -varioance limits (from Data if max<min)
1 1                                 -Plot sill (0=no,1=yes), sill value)
Variogram plot
GSLIB/save/GR_R1_SGSIM_output.out
1 0 1 0 1                           -  Variogram #, dash #, pts?, line?, color
GSLIB/save/GR_R1_SGSIM_output.out
2 0 1 0 7                           -  Variogram #, dash #, pts?, line?, color
GSLIB/save/vmodel.var
1 0 0 1 1                           -  Variogram #, dash #, pts?, line?, color
GSLIB/save/vmodel.var
2 0 0 1 7                           -  Variogram #, dash #, pts?, line?, color
```

Glossary

active layer the soil that is regularly exposed to freezing and thawing conditions on an annual basis 2, 9

pedotransfer functions empirical functions linking soil properties to some basic shared characteristics 84

permafrost ground remaining frozen for at least two consecutive years iv, v, xiii, 2, 3, 5, 8–10, 15, 18–20, 22, 24, 74, 88

talik perennially thawed soil between the active layer and permafrost v, xiii, 2, 3, 9, 10, 75, 89, 108

thermokarst lake lake formed due to permafrost thaw and the depression of surface ground 2, 74

zero-curtain effect due to this effect, soil's temperature stays close to the freezing point of water due to the effect of latent heat of fusion 79